SCUOLA DI SCIENZE
Dipartimento di Chimica Industriale "Toso Montanari"

Corso di Laurea Magistrale in
Chimica Industriale
Curriculum: Advanced Spectroscopy in Chemistry
Classe LM-71 - Scienze e Tecnologie per la Chimica Industriale

Characterisation and speciation of particulate matter deposited on PTFE and quartz filters

CANDIDATE

Zhanar Zhakiyeva

SUPERVISOR

Prof. Marco Giorgetti

CO-SUPERVISORS

Prof. Sylvain Cristol, Prof. Reinhard Denecke

Characterisation and speciation of particulate matter deposited on PTFE and quartz filters

CANDIDATE

Zhanar Zhakiyeva

SUPERVISOR

Prof. Marco Giorgetti

CO-SUPERVISORS

Prof. Sylvain Cristol, Prof. Reinhard Denecke

Session I

Academic Year 2016/2017

TABLE OF CONTENTS

CHAPTER III RESULTS

III-2 XPS results

CHAPTER IV DISCUSSION

IV-1 Speciation of the elements

LIST OF FIGURES

LIST OF TABLES

ABSTRACT

Respirable fractions of airborne ambient particulate matter (PM), specifically PM_{10} and $PM_{2.5}$, have been identified over the years as potential health hazards. Moreover, there is a big concern about potentially toxic species that can dissolve in lung fluids and bloodstream. This toxic species can be either organic or inorganic in origin. Due to chemical complexity, extremely small particle sizes, small sample size collected on filters, analysis of such samples is quite problematic. The technique that has a great potential for elemental speciation of fine PM inside the bulk of the filter is a synchrotron-based X-ray Absorption Fine Structure Spectroscopy. This technique allows to identify the form of an occurrence of an element in the complex mixture, complementing compositional elemental data obtained by X-ray fluorescence and Proton-Induced X-ray Emission (PIXE). Additionally, XAFS is non-destructive and sensitive to parts-per-million (ppm) concentration levels of many elements when the signals are detected in fluorescence configuration. However, it is well known that chemical composition of airborne PM on the surface differs from that of the core. Moreover, many studies have shown that there is a good correlation between the surface composition of aerosol particles and their role in environmental processes, such as atmospheric scavenging and cloud condensation nuclei. Therefore, an X-ray Photoelectron Spectroscopy was employed to investigate the surface composition of PM. XPS is a non-destructive technique that requires minimum sample preparation. Furthermore, XANES K-edge spectra simulations using FDMNES code were performed in order to simulate lacking reference data for elements in scarce amounts. We went even further and performed FDMNES calculations for intermediate energy of sulphur K-edge. Previously such XAS simulations were done in solitary cases, therefore our interest was justified. Following the pre-edge and XANES analyses outcomes of the three investigated filters, and by considering the relative abundance of the metals in them, an EXAFS analysis at the Fe K-edge only was performed. It provided quantitative data of the selected metal core bonding, was performed. In particular the local atomic environment of the Fe site has been revealed, providing bond length referring mostly to the first coordination shell.

CHAPTER I INTRODUCTION
I-1 PM

I-1-1 Air Pollution: historical aspects

In the 17th century, the coal burning near the palace at Westminster was forbidden by Queen Elizabeth I because of the offensive nature of smoke, and therefore the factories were moved away from London. Already in the 19th century, clinicians in England linked various lung diseases to air pollution. Nonetheless, a proper legislation to control air pollution was lacking in many industrial countries, until the major industrial air pollution episodes occurred in the Meuse Valley (Belgium, 1930), and in Donora Valley (Pennsylvania, United States, 1948) and in urban London (December 1952). In Belgium and US, air pollution was caused by excessive smoke from coal-burning domestic appliances and industrial furnaces, whereas in London, a dense fog occurred during inversion weather and lasted for four days. The detected concentrations of smoke particles and sulphur dioxide were 10 times of normal levels. Almost 4,000 deaths occurred during or after the episode, mostly of elderly people with chronic heart and lung diseases. Later, in the 1970s and 1980s many big cities had serious air pollution episodes such as Chicago, Mexico City, Lagos, Cairo, Tokyo etc. As a consequence, many developed countries introduced environmental legislation and created environmental protection agencies[8].

The introduction of new clean air regulations led to the reduction of pollution episodes in urban areas, elimination of winter smog (London-type pollution), and significantly improved levels of photochemical pollutants (California-type pollution) because of aggressive controls on vehicle exhausts and industrial fumes. But the problem of adverse health effects and excess deaths by airborne particulate matter (PM) in urban areas were not eliminated, as it was believed by an extensive review of Holland et al [9].

The reason that PM became very important air pollutants in recent decades and their adverse health effects became more hazardous is that air pollution in urban areas has changed. Air pollution from combustion of traditional fossil fuels (biomass, coal, wood, crude oil, diesel with high content in sulfur) is now in much lower concentrations than 30 to 40 years ago because of better and cleaner technologies, but other pollutants have gained prominence, such as fine and ultrafine PM, because of a dramatic increase in motor vehicle use worldwide with the consequent rise in exhaust emissions in urban areas. Nowadays, airborne PM is found not only in big cities but also in small and large towns, and their size distribution and composition is now more varied, e.g. they may contain heavy metals, PAHs, etc.[8].

I-1-2 Particulate matter composition and origins

Particulate matter (PM) is a complex, heterogeneous mixture that changes in time and space. It encompasses emissions from both natural and man-made sources. Natural sources include wind-blown dust, sea salt, volcanic ash, pollens, fungal spores, soil particles, the products of forest fires and the oxidation of biogenic reactive gases. Manmade sources include fossil fuel combustion (especially in vehicles and power plants), industrial processes (manufacturing metals, cement, lime and chemicals), construction work, quarrying and mining activities, cigarette smoking and wood stove burning. The main source of PM in urban areas is road transport in addition to the burning of fossil fuels in power stations and factories. Components of traffic-derived PM include engine emissions and wear, brake and tyre wear and dust from road surfaces. The largest single source of airborne PM from motor vehicles is derived from diesel exhaust (diesel fuel combustion results in many more particles than gasoline engines). Owing to the increase in the number of new cars with diesel engines in industrialised countries, diesel exhaust particles (DEPs) account for most airborne particulate matter (up to 90%) in the world's largest cities. These particles are composed of a carbon core upon which high-molecular weight organic chemical components and heavy metals deposit. One of the most important distinctions of particulate pollution is based on how the particles are introduced into the atmosphere. [10].

The behaviour of particles in the atmosphere and within the human respiratory system is determined largely, but not wholly, by their physical properties which have a strong dependence on size, varying from a few nanometres to tens of micrometres. The class of coarse particles consists of particles having diameters greater than 2.5µm, the most widespread being $PM_{2.5}$ and PM_{10}. This class includes the most visible or obvious forms of PM such as black smoke, soil, dust from roads and building sites, large salt particles from sea spray, mechanically generated particles, as well as some secondary particles. Coarse particles also include pollen, mould, spores and other plant parts. PM_{10} denotes all ambient PM (i.e. ultra-fine, fine and coarse particles) having a diameter of 10µm or less and are sometimes termed "thoracic" particles in that they can escape the initial defences of the nose and throat and penetrate beyond the larynx to deposit along the airways in the thorax[10].

I-1-3 Health hazards

Over the years exposures to ambient PM have been related to enhanced mortality and morbidity. PM exposures were reported to induce oxidative stress, pulmonary inflammation and modulate the immune responses of the lungs. Moreover, the PM were linked to various respiratory infections such as pneumonia, especially among the elderly. Previously, the toxicity of PM has been related to the particle size and not to its composition, however in last years it is being discovered that the

composition of PM strongly determines its toxicity[11, 12]. Associations between chemical composition and particle toxicity tend to be stronger for the fine and ultrafine PM size fractions[8]. Janssen et al. have demonstrated, that exposure to air pollution is associated with reductions in lung function and growth, asthma, allergic rhinitis and respiratory infections in children. The reason that children are more vulnerable than adults is in the higher permeability of their airways to air pollutants compared to adults and the immaturity of their respiratory defence mechanisms[10, 13].

I-2 X-ray Absorption Fine Structure Spectroscopy

X-ray Absorption Fine Structure spectroscopy is a unique tool for studying at the atomic structure at a molecular level, being highly sensitive to the local structure around selected elements that are contained within a material. The main advantage of this technique is that it can be applied not only to crystals, but also to materials without a long-range order: amorphous systems, glasses, disordered films, solutions, liquids, metallo-proteins, and in this work, particulate matter. Moreover, XAFS is also an electronic spectroscopy, that measures transitions between bound initial states and continuum final states[14].

I-2-1 Physics of XAFS

XAFS is intrinsically a quantum mechanical phenomenon that is based on the X-ray photoelectric effect, in which an incoming X-ray photon is absorbed by an atom, followed by freeing an electron from an inner atomic orbital (Figure 1). The "photoelectron" wave scatters from the atoms surrounding the absorbing atom, creating interferences between the outgoing and scattered parts of the photoelectron wavefunction, which provides information about the structure, structural disorder and thermal motions of neighbouring atoms. Other phenomena occurring are heat, X-ray fluorescence and production of electrons (the detection of which is at the basis of an X-ray photoelectron spectroscopy experiment), and of course the scattering of X-rays which is another fundamental X-ray-material interaction. This scattering could be either coherent, also called elastic (i.e., X-ray diffraction, where the scattered photons interfere with each other) or incoherent, leading to the family of inelastic scattering-based techniques[3].
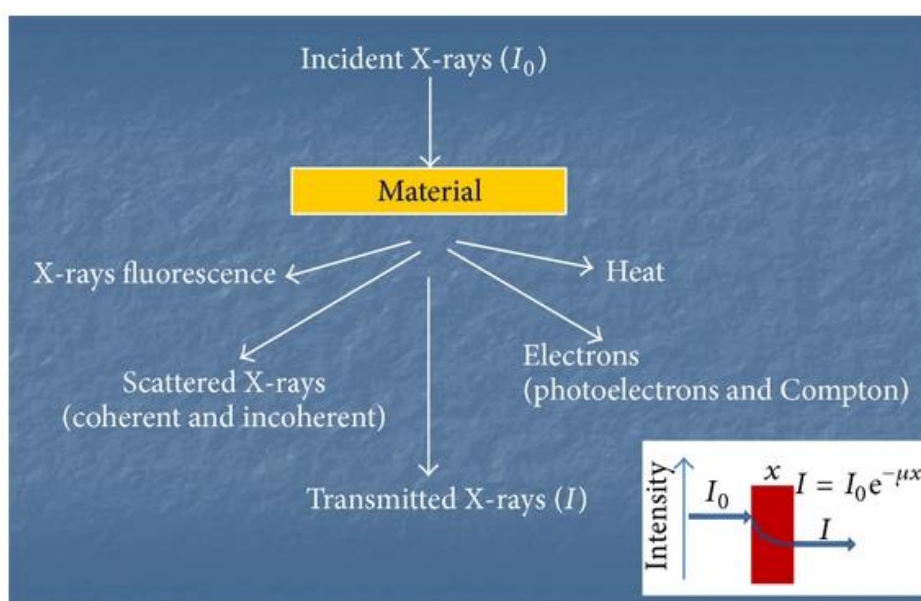
Figure 2 Interaction of X-rays photons with matter (taken from Giorgetti M.)[3]

As displayed at the bottom of Figure 1, the absorption of X-rays can be measured quantitatively, and it follows a similar exponential decay given by the Beer-Lambert law which describes optical transitions. The quantity of interest here is called linear absorption coefficient and it can be considered analogous to the absorbance in UV-vis spectroscopy. It is measured in $[cm^{-1}]$. Actually, because of its applicability to all states of matter, it is more convenient to use the mass absorption coefficient μ_m obtained by normalization to the density of the material ρ, that is, (μ/ρ); therefore, the dimension becomes $[cm^2/g]$. The absorption coefficient describes how strongly X-rays are absorbed as a function of energy E. In general, matter becomes more transparent to X-rays at higher energies; that is, X-rays are more penetrating following a decreasing function proportional to $(1/E^3)$ of the absorption cross-section $\mu(E)$. However, at specific energies that are element-specific, there is a sudden increase in the cross section, also called X-ray absorption edge. This dramatic increase of the absorption is due to the photoelectric effect[3, 14]. In order to observe such an edge, the X-ray photon has to have a sufficient energy to liberate electrons from the low-energy bound states in the atoms. Absorption edges were first measured by Maurice de Broglie in 1913, and in 1920 Hugo Fricke first observed the "fine structure" – energy-dependent variations in $\mu(E)$. Afterwards, despite the enthusiasm about this new technique, the theoretical explanation of XAFS remained vague. Only in the 1970s Stern, Sayers and Lytle had clarified the essential points of a theory of XAFS and showed that XAFS could be a practical tool for structure determination.

The X-ray photoelectric process which gives rise to such an absorption is summarized in Figure 2. An X-ray photon is absorbed by an atom, and the excess energy is transferred to an electron which is expelled from the atom, leaving it ionized. This electron is called photoelectron, and we will see how it is responsible for the EXAFS mechanism. The electron vacancy created in the photo absorption process leaves the atom in a very unstable condition and therefore two competing processes may occur. The first is X-ray fluorescence, in which a higher energy core-level electron fills the deeper core hole, emitting an X-ray of well-defined energy. This provides a unique signature of the atoms constituting the material once those photons are collected by a detector, as in X-ray fluorescence spectroscopy (XFS). The second process (for de-excitation of the core hole) is the Auger effect, in which an electron drops from a higher electron level and consequently, a second electron is emitted into the continuum. The measurement of these electrons is made possible by Auger spectrometers. In the hard X-ray region (>2 keV), X-ray fluorescence is more likely to occur than Auger emission, but for lower energy the Auger process dominates.
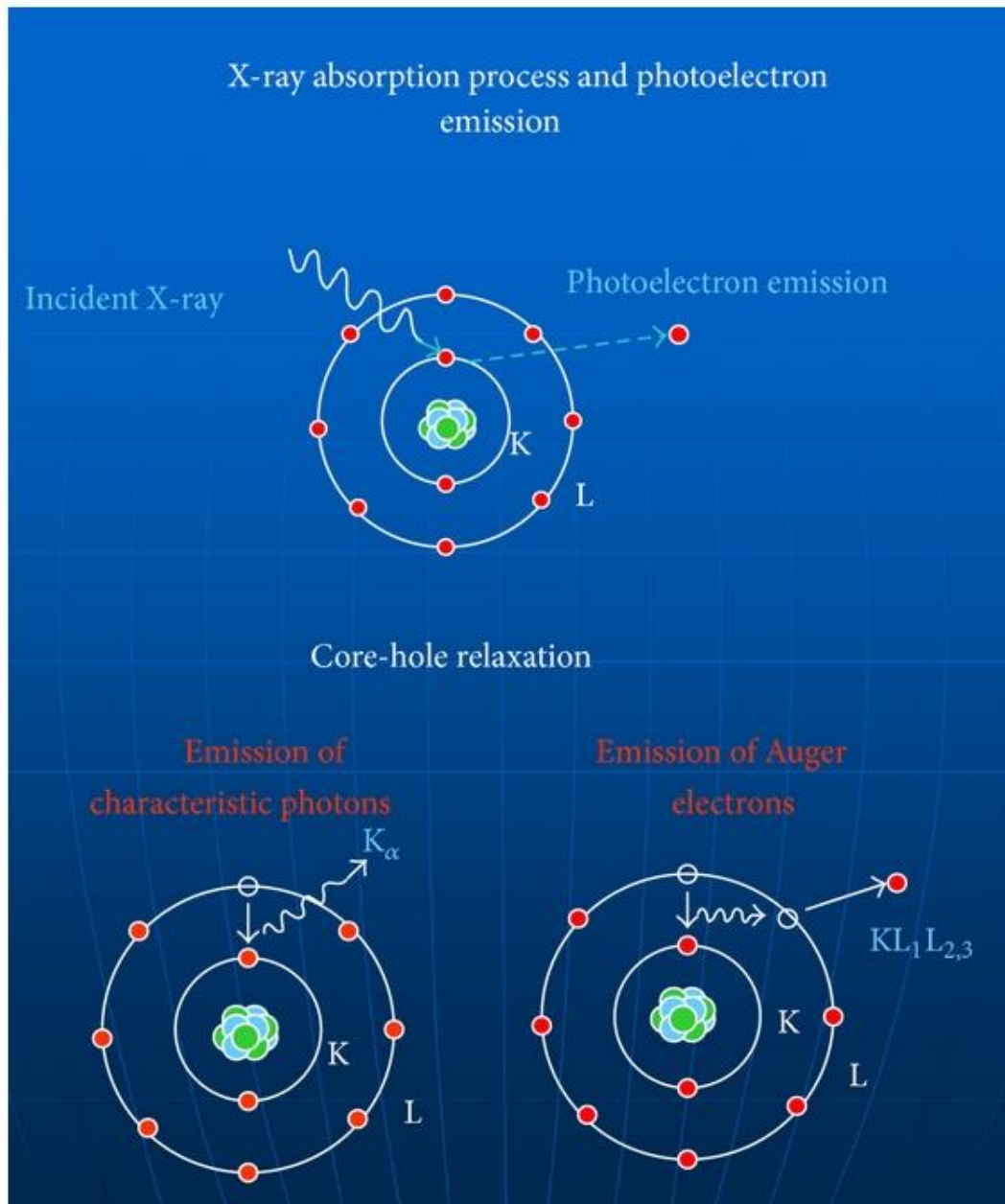
Figure 1 The photoelectric absorption process which creates a core hole, and its relaxation by fluorescent X-ray emission or Auger electron emission (taken from Giorgetti M.)[3]

I-2-2 XANES and EXAFS regions

X-ray Absorption Near Edge Structure (XANES) starts at absorption edge (E_o) and spans for approximately 30 eV. In this region a core electron is excited into a bound empty valence state. The shape and intensity is characteristic of the oxidation state, number and type of atoms bonded to the excited atom. Intense peaks at the top of the edge are historically called "white lines", because of their appearance on photographic plates[14]. The most common and the simplest interpretation of the XANES region is an identification of the oxidation state of an element. When the electron density around the absorbing atom decreases, its affinity towards electrons increases,

6

resulting in the shift of the absorption edge to slightly higher energies. These shifts of the order of few eV act as fingerprints of specific oxidation states. Generally, the edge energy is assigned as the position of first inflection point at the absorption edge, or the maximum at the derivative spectrum.

Additionally, by employing linear combination fitting techniques (LCF), the amounts of different components giving unique spectral features to XANES spectra, can be determined. This is made possible by the peculiar property of mass-absorption coefficients, which can be added together when multiple components are present. Also, XANES spectra can also be calculated. Among several programs performing such calculations, in this work the FDMNES code was employed. The FDMNES (Finite Difference Method Near Edge Structure) package is an *ab initio* code, which is based on building clusters around the absorbing atoms and performing several independent calculations when there are several non-equivalent absorbing atoms[15]**.**

Another part of the XAS spectrum that comes after the XANES region and ranges to approximately 1000 eV above the edge is called Extended X-ray Absorption Fine Structure spectrum (EXAFS). The EXAFS phenomenon arises from the quantum-mechanical interference resulting from the scattering of a photoelectron by the potential of the surrounding atoms.

This is seen from Figures 3 and 4 where the photoelectron emitted by the photoabsorbing atom (blue) propagates as a spherical wave and spreads out over the solid. At this point the mechanism can be different in case of an isolated atom (Figure 3) or a coordinated atom on (Figure 4). In the latter case, the emitted photoelectron is reflected off by the neighbouring atoms (yellow) to the absorbing atom and so does every atom in the material. The amplitude of all the reflected electron waves adds either constructively or destructively to the spectrum of the absorbing atom and hence the X-ray absorption coefficient exhibits the typical oscillations depicted at Figure 4 (bottom).

$$\vec{k} = \sqrt{2m(E - E_0)/\hbar^2}$$

$$\lambda = \frac{2\pi}{k}$$

$$\mu \approx \frac{\rho Z^4}{AE^3}$$

Absorption (a.u.)

E (eV)
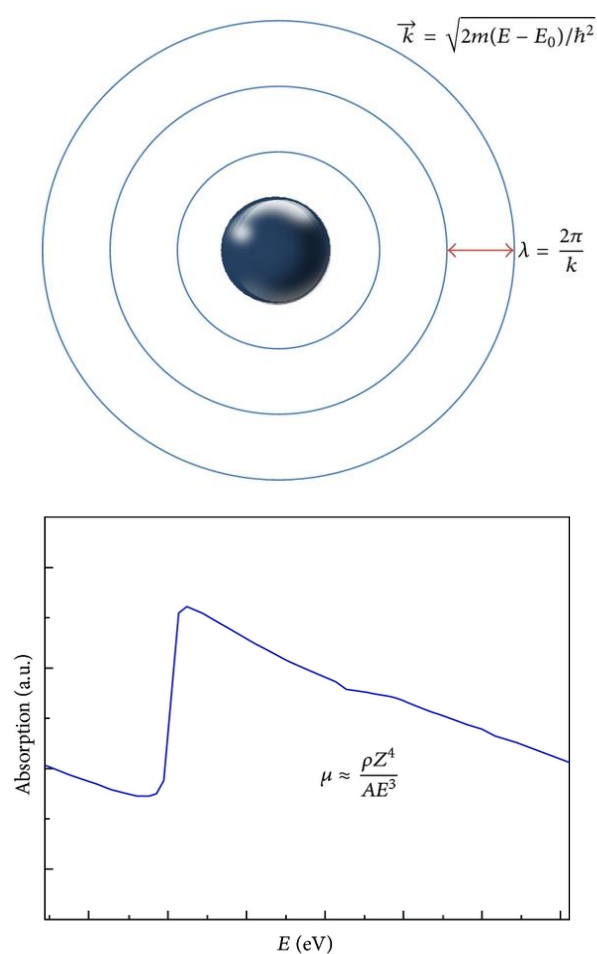
Figure 2 Emission of a photoelectron for an isolated atom (adapted from Giorgetti M.)[3]
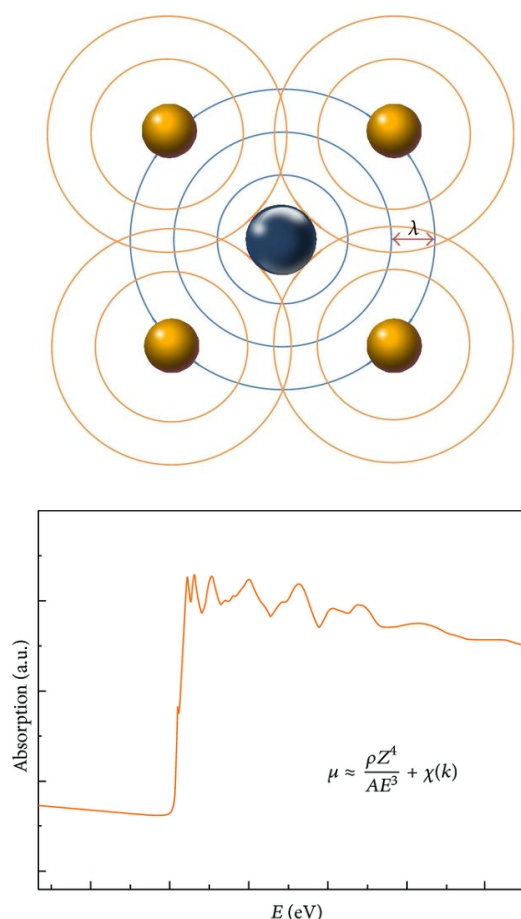
Figure 3 Emission of a photoelectron for a coordinated atom. The absorption coefficient measured at a central atom threshold shows a fine structure due to the presence of neighboring atoms (adapted from Giorgetti M.)[3]

A crucial issue is the recognition that the photoelectron is not infinitely long lived but decays as a function of time and distance, therefore, the EXAFS cannot probe long-range distances. EXAFS can give only local structural information, of about several angstroms around the selected atomic species. Of course, this mechanism does not happen in the case of isolated atoms like Ar gas, which leads to the corresponding X-ray absorption edge to appear featureless as observed in Figure 3 (bottom). From the time frame of the EXAFS phenomenon it is helpful to underline that this takes place at a time scale much shorter than that of atomic motion (also vibrations), so the measurement is a sum of instantaneous spectra of molecules at different stages of their vibrational cycle. This results in a damping of the EXAFS oscillations and is normally considered in the data analysis by means of an EXAFS Debye-Waller like factor. EXAFS should be considered as a bulk technique, because all the materials under investigation contribute to the overall shape of the XAS spectrum. As the oscillations in absorption are related to neighbouring atoms, the EXAFS region gives information about the number and type of neighbouring atoms and their distance to the absorbing atom [3, 16]. As a customary, in order to obtain the relevant structural parameters from an EXAFS features the experimental spectrum is fitted with a suitable structure. In this work, the fit obtained for an Fe K-edge case will be presented.

I-2-3 Synchrotron radiation

At the same time as XAFS spectroscopy was developing, research on synchrotron radiation was equally progressing. In the 1970s, when Stern, Sayers and Lytle were completing XAFS theory, the first synchrotron radiation facilities were developed. Nowadays, almost all XAFS experiments are performed at Synchrotron Radiation Sources (SRS) due to a high energy tuneable X-ray beams that are produced there. SRSs were the "bonuses" coming from high-energy physics experiments, which were later adapted to produce high-energy electromagnetic radiation with desirable spectral characteristics. Electrons moving close to the speed of light within an evacuated pipe are guided

around a closed path of 100-1000 meters circumference by vertical magnetic fields. When the trajectory bends, the electrons accelerate (change velocity vector). Accelerating charged particles then emit electromagnetic radiation[14].

I-3 X-ray Photoelectron Spectroscopy

X-ray photoelectron spectroscopy was developed in the mid-1960s by Kai Siegbahn and his research group at the university of Uppsala, Sweden. The technique was first called ESCA (Electron Spectroscopy for Chemical Analysis). Later, in 1981, Siegbahn was awarded the Nobel Prize for Physics for his work with XPS.

The XPS experiment is based on irradiating a solid *in vacuo* with monoenergetic X-rays and by analysing the energy of the electrons emitted. The spectrum is a plot of the number of detected electrons per energy interval versus their kinetic energy. Each element has a unique spectrum with the mixture of elements giving the sum of the peaks of individual constituents. As the mean free path of electrons in solids is very small, the detected electrons originate from the top few atomic layers only, which makes XPS unique surface-sensitive technique. Quantitative data can be obtained from peak heights or peak areas, and identification of chemical states can be concluded from the exact measurement of peak positions and separations [17].

I-3-1 Principles of the technique

XPS proceeds by irradiating a sample with monoenergetic soft X-rays, generally Mg Kα (1235.6 eV) or Al Kα (1486.6 eV), and by analysing the energy of the detected electrons (Figure 6). These photons (penetrating power 1-10 μm) interact with atoms in the surface region, causing the electrons to be emitted by the photoelectric effect. The emitted electrons have measured kinetic energy given by:

$$KE = h\nu - BE - \varphi_s$$

where hν is the energy of the photon, BE is the binding energy of the atomic orbital from which the electron originates, and φ_s is the spectrometer work function.
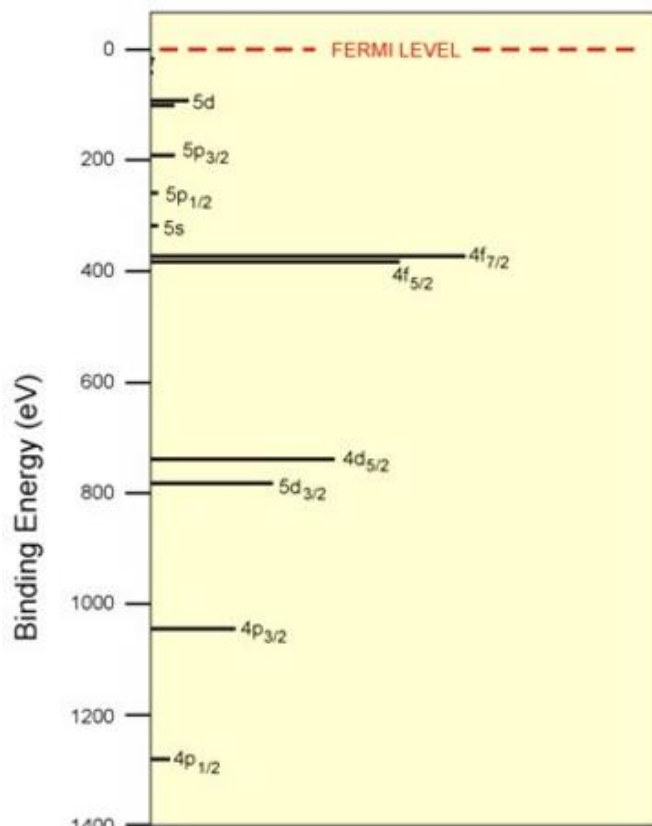
Figure 5 Relative binding energies and absorption cross-sections of uranium. The binding energy is proportional to the distance below the line indicating the Fermi level, and the ionization cross-section is proportional to the length of the line.[1]

BE is the energy difference between the initial and final states after the photoelectron has left the atom. As there is variety of possible final states of the ions from each type of atom, there is a corresponding variety of KE (Kinetic energies) of the emitted electrons. Furthermore, there is a different probability or cross-section for each final state. The Fermi level corresponds to zero BE (by definition), and the depth beneath the Fermi level in the Figure 5 indicates the relative energy of the ion remaining after electron emission, or the binding energy of the electron. The line lengths indicate the relative probabilities of the various ionization processes. The p, d and f levels become split upon ionization, leading to vacancies in the $p_{1/2}$, $p_{3/2}$, $d_{3/2}$, $d_{5/2}$, $f_{5/2}$ and $f_{7/2}$ levels. The spin-orbit splitting ratio is 1:2 for p levels, 2:3 for d levels and 3:4 for f levels.

As each element has a unique set of binding energies, XPS can be used to identify and determine the concentration of the elements of the surface. Variations in the elemental binding energies (the chemical shifts) come from the differences in the chemical potential and polarizability of compounds. These chemical shifts are used to identify the chemical state of the materials being analysed.
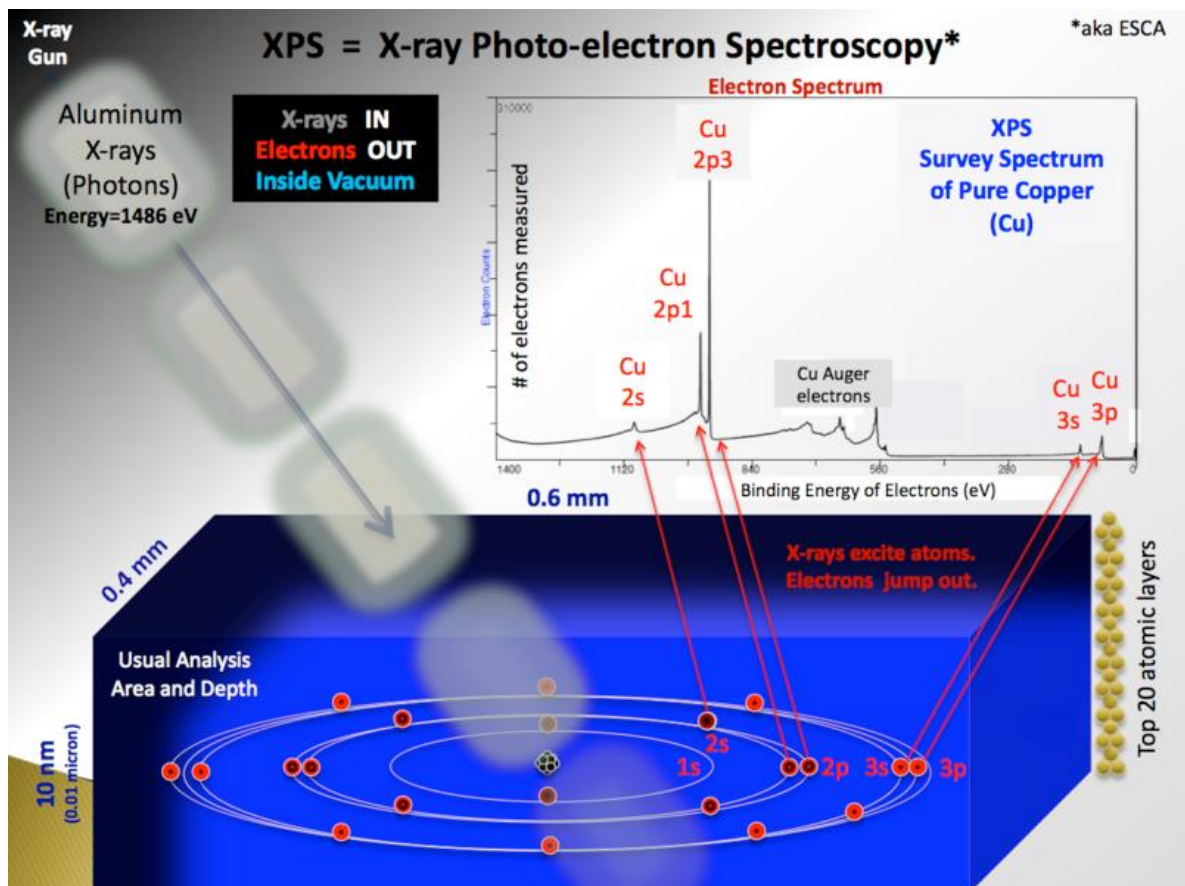
Figure 6 Schematic of XPS experiment (taken from Crist V.)[18]

In addition to the photoelectrons emitted in the photoelectric process, Auger electrons may be emitted because of relaxation of the excited ions remaining after photoemission. This Auger

electron emission occurs roughly 10^{-14} seconds after the photoelectric event. The competing emission of a fluorescent X-ray photon is a minor process in this energy range. In the Auger process (described previously on Figure 2 in XAFS introduction part), an outer electron falls into the inner orbital vacancy, and a second electron is simultaneously emitted with an excess energy. The Auger electron possesses kinetic energy equal to the difference between the energy of the initial ion and the doubly charged final ion, and is independent of the mode of the initial ionization. Therefore, photoionization leads to two emitted electrons - a photoelectron and an Auger electron.

The probability of electron interaction with matter is way higher, so while the path length of the photons is of the order of micrometres, that of the electrons is of the order of tens of angstroms. Thus, while ionization occurs to a depth of a few micrometres, only those electrons that originate within tens of Angstroms below the solid surface can leave the surface without energy loss. These electrons which leave the surface without energy loss produce the peaks in the spectra and are the most useful. The electrons that undergo inelastic loss processes before emerging form the background[17].

MOTIVATION OF WORK

As described in the introduction, PM is a complex, heterogeneous mixture that changes in time and space. It encompasses many different chemical components and physical characteristics, many of which have been cited as potential contributors to its toxicity. Each component has multiple sources, and each source generates multiple components. Identifying and quantifying specific components and assigning chemical speciation represents one of the most challenging problems of analytical and environmental science. Generally, PM analysis is done using conventional techniques such as: gravimetry, inductively coupled plasma- mass spectrometry, atomic absorption spectroscopy etc. However, these techniques give information only about the elemental composition. In this work, we have successfully gone beyond the elemental characterization. By using core-level spectroscopy techniques we were able to obtain oxidation states, local structure arrangement and symmetry around selected sites and element quantification of different layers. Since the term *speciation* refers to the chemical form or compound in which an element occurs, this work can be considered an excellent example of chemical speciation.

CHAPTER II EXPERIMENTAL AND METHODS

II-1 PM sampling

Particulate matter deposited on filters were collected by the group of Prof. Laura Tositti (University of Bologna, Chemistry Department) from January till July 2012. For each collection, daily samplings of 24h duration were made. The two samples were named VADO and QUI, referring to their respective sampling zones. Therefore, several filters were available for analysis, which were identified by their sampling number. The VADO filter deposited PM_{10} on two different types of filter (quartz and Teflon), while the QUI filter collected PM_{10} and $PM_{2.5}$ on Teflon filters. In this work only two VADO filters (VADO 118 and VADO 28) and one QUI 156 filter will be analysed.

The particulates were collected on two different types of filters: Teflon and quartz chosen according to the type of analysis planned, in order to obtain the most complete characterization of the particulates. Since, the PM is an extremely complex mixture where a number of organic and inorganic species are present, the choice of the filtering support was a critical aspect. The material constituting the membranes should be compatible with the type of analyte to be determined, and must not alter its composition through the chemical impurities. The degree of purity of the filters was verified every time a new set was acquired. Generally, the filters in quartz are used to determine and characterize the carbon fractions and the ions, while those in polymeric material are used to determine and characterize the inorganic fraction. The Teflon filters were used for PIXE analysis.
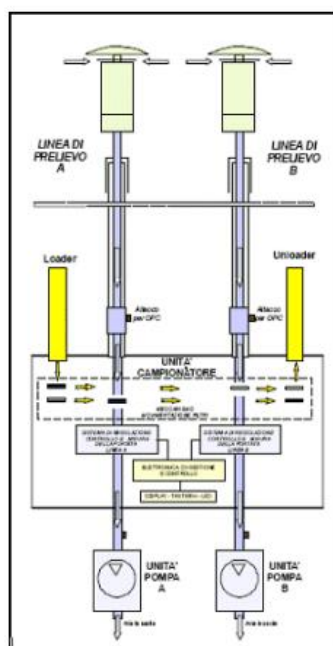
Figure 7 The scheme and the photo of a sampler FAI SWAM Dual Channel

The sampling instruments have three units as shown on Figure 7:

1. Two sampling lines allowing the sampling of a particulate matter suspended in the atmosphere. Each line includes a sampling head with the function of collecting the exact size of PM, and with anti-wind and anti-rain properties.

2. A filtering station with one or two filtering membranes on which PM is accumulated.

3. Two suction pumps, which intake air from the environment through the sampling heads, the sampling tubes and the filtering membranes located in the filtering station.

At the end of every sampling cycle, the filters were transferred in a waste container. The operator could proceed to replace the filters (loading clean filters, unloading sampled filters) at any moment without interfering with the ongoing sampling. The two sampling pumps worked simultaneously and synchronously, to allow the collection of samples that are independent but perfectly equivalent in terms of the sampling's time length. Furthermore, the sampler was equipped with a temperature controlling system, in order to limit the loss of semi-volatile species such as NH_4NO_3 and various other organic species (adapted from Tositti et al.)

II-2 XAFS data collection

X-ray absorption near edge structure (XANES) and Extended X-Ray Absorption Fine Structure (EXAFS) spectra have been recorded at the XAFS of Elettra-Sincrotrone Trieste, Basovizza, Italy through the project №20150161 "Airborne particulate matter: metal speciation by X-Ray Absorption Spectroscopy" (project leader M. Giorgetti)[19] and further in-house experiments. The storage ring was operated at 2.0 GeV in top up mode with a typical current of 300 mA. Data have been recorded at the S, Ca, Ti, V, Cr, Mn, Fe, Ni, Cu, and Zn K-edges. The white beam was monochromatized using a fixed exit monochromator equipped with a pair of Si (111) crystals. Harmonics were rejected by using the cut-off of the reflectivity of the Platinum mirror placed at 3 mrad with respect to the beam upstream the monochromator and by detuning the second crystal of the monochromator.

Internal reference of Ca, Ti, V, Cr, Mn, Fe, Ni, Cu, and Zn foils were used for energy calibration in each scan. The first inflection point for Ca, Ti, V, Cr, Mn, Fe, Ni, Cu, Zn was set at 4038.5, 4966, 5465, 5989.9, 6539.0, 7112, 8333, 8979 and 9659 eV, respectively. This allowed a continuous monitoring of the energy during consecutive scans. No energy drifts of the monochromator were observed during the experiments. Spectra were collected with a constant k-step of 0.03 Å^{-1} with 3s/point acquisition time from 2200 to 3500 (S K-edge); from 3800 to 4800 eV (Ca K-edge); from 4700 to 5500 (Ti K-edge); 5200-6000 eV (V K-edge); 5700 to 6500 eV (Cr K-edge); from 6300 to 7100 (Mn K-edge); from 6900 to 7700eV (Fe K-edge); from 8100 to 8900 eV (Ni K-edge); 8700 to 9400 eV (Cu K-edge) and from 9400 to 10500 (Zn K-edge).

Spectra have been collected in fluorescence mode with the sample positioned at 45° with respect to the beam. The total fluorescence yield is measured as a function of the X-ray energy using a silicon drift KETEK detector. More than one spectrum was collected per each sample. The spectra were then averaged and normalized according to the standard procedure using the ATHENA program[20].

Surface chemical characterization was performed using XPS in a Thermo Scientific Escalab 220i-XL spectrometer. Samples of ~0.25 cm^2 of VADO 118 and ~0.09 cm^2 of VADO 28 were supported on the sample holder with a carbon tape. For all XPS measurements the base pressure in the analyzer chamber was $1.0*10^{-8}$ mbar or less. The samples were excited by Al Kα (1486.68 eV) radiation from an Aluminium-Magnesium-twin-X-ray tube. Two lens modes were used: large area (LAE) and large area-XL (LAXL) depending on the size of the probe. When the latter mode was utilized the samples were irradiated with electron gun (flood gun) to prevent a positive charge accumulation. The layer composition and depth profiles of the VADO 118 and VADO 28 filters were investigated by sputtering with 1 keV Ar$^+$ ions. The etching time was varied as 2, 10 and 30 min for VADO 118 filter and 10 min for VADO 28 filter.

The measurement parameters for the survey (white background) and detailed spectra (blue background) of the filters are summarized in Table 1 below. The measurement conditions were kept constant for all VADO 118 samples, and varied slightly for VADO 28 and QUI 156 as indicated in below.

Filter code	Sputtering time (min)	Energy range (eV)	Pass energy (eV)	Step size (eV)	Dwell time (ms)	Number of scans	Lens mode
QUI 156	0	-5 --1205	50	1	100	1	LAE
VADO 118	0, 2, 10, 30	-5 -- 1205	50	0.5	100	1	LAE
VADO 28	10	-5 -- 1205	50	0.5	100	1	LAXL
QUI 156	0, 2, 10, 30	Depending on the element	10	0.1	300	5	LAE
VADO 118	0, 2, 10, 30		20	0.1	300	4	LAE
VADO 28 "*old*"	10		20	0.1	300	4	LAXL
VADO 28 "*new*"	10		50	0.1	300	4	LAXL

Table 1 XPS measurement parameters

The data acquisition was performed using Thermo Scientific™ Avantage Software and data analysis with UNIFIT 2016 software[21, 22]. First the background was fitted using Shirley function followed by curve fitting using a convolution of Gaussian and Lorentzian functions.

II-4 FDMNES package details

The FDMNES (Finite Difference Method Near Edge Structure) package is an *ab initio* code, which is used to calculate the XANES (X-ray absorption near edge structures) spectra, which extend up to around 50 eV after the absorption edge. It builds clusters around the absorbing atoms performing several independent calculations when there are several non-equivalent absorbing atoms[15]. The challenging problem is to compute the final states, which depend on the local atomic structure, while the initial state is a core state easy to calculate. There are different ways to calculate these final states. One of them uses the local density approximation by considering clusters using the multiple scattering (MS) theory. Generally, MS theories use a muffin-tin approximation: averaging of the potential needed for the expansion of the wave functions. This approximation assumes the spherical shape of the potential in the atomic and outer sphere regions and volume averaged in the interatomic regions, which makes the results depend on the size of the interstitial region.

Another way to solve the Schrodinger equation using the local density approximation which avoids the muffin-tin approximation is the finite-difference method (FDM). The first formulation of FDM to solve the Schrodinger equation was given in the 1930s.

II-4-1 Finite difference method

In the FDM method a general way to solve differential equations by discretizing them over a grid of points in the whole volume where the calculation is made (Figure 8). In XANES, the equation is solved over a spherical volume, centred on the absorbing atom and the radii extending over a sufficiently large cluster. Inside this sphere the classical FDM equation is used. However, close to the ion core, the kinetic energy of the electron is very high, whereas in the region between two ion cores, it is much lower. A way to solve this discrepancy is in performing an expansion in
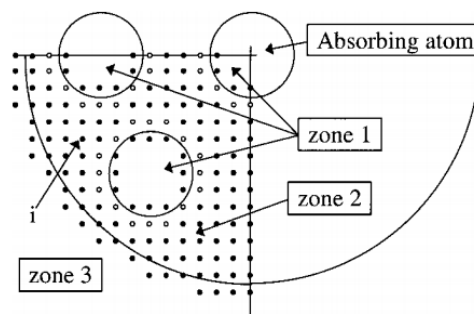
Figure 8. General view of the region of calculation around the absorbing atom. Symmetry planes are used to reduce the area of calculation. This one is divided in three zones: (1) around the atomic cores, (2) between the atoms where the standard FDM calculation is used, (3) the outer sphere region. White points are at the boundary of the ion core. Gray points are at the boundary of the outer sphere (adapted from Joly et al.)[5]

spherical waves in very little sphere around the atomic cores (0.5-0.7Å), assuming that potential is quite spherically symmetric in these areas. After writing the Schrodinger equation on all points of the grid, the potential must be introduced in the general matrix. As usual in standard XANES calculations, the local density approximation is used to calculate the potential. The FDM

formulation allows no approximation of the shape of the potential, thus avoiding the problem related to the classical muffin-tin approximation.

II-4-2 Muffin-tin calculations

The muffin-tin approximation corresponds to a monopolar representation of the potential and the potential in the interstitial region is constant. Overlapping muffin-tin spheres are used to take into account a part of the scattering power of the interstitial area. The use of overlapping spheres approximation is mathematically wrong, however when it is up to 10-15%, the advantages overcome the error. Sometimes, relatively good artificial agreement can even be reached when changing the interstitial potential and the muffin-tin radius. In order to have the best possible MS muffin-tin calculation, a muffin-tin radius and the interstitial potential value should be chosen carefully. The best radius is the one which minimizes the potential jump between the sphere and the interstitial area. For a muffin-tin approximation, generally a 10% to 15% overlap is used, because it has empirically been observed by the authors that with such overlap that the agreement with experiment is often the best [5].

II-4-3 The general procedure

All the sequences of the spectra calculations can be summarized in the following way: 1) From the molecule or the unit cell atom positions the code evaluates the non-equivalent and equivalent atoms with the symmetry operation relating them to each other. 2) For each non-equivalent and absorbing atom, a cluster is formed around it with a radius chosen by the user. The point group is evaluated, giving the shape of the scattering tensors and the useful representation to calculate. 3) For each cluster the final states are calculated. One of the two methods are chosen by the user: the finite differences method (FDM) or the multiple scattering theory (MST), the latter within the limits of the muffin-tin approximation (MT)[15]. The FDM is time consuming, so generally we start with MT approximation.

II-4-4 Details of the calculations

To interpret X-ray near-edge absorption spectra, we performed theoretical calculations in the framework of the MST within the MT potential approximation and the finite difference method with a full potential. Both methods were implemented in the FDMNES (2016) code (Joly, 2001). As mentioned earlier, the calculations started using MT approximation, but this method failed to reproduce spectral features, therefore only spectra calculated using FDM are presented here. Another thing to note is that the calculations were executed with a number of different sulphates, however only sodium sulphate was measured experimentally by us, therefore it is the only sulphate presented here.

For sodium sulphate spectra calculations clusters with radii of 6 Å and for sodium sulphate decahydrate clusters of 4.1 Å and 6 Å are presented here. The unit-cell parameter for $Na_2SO_4*10H_2O$ was taken from Ruben et al. with a space group $P2_1/c$ [23]; for anhydrous Na_2SO_4 from Neues et al., Mincryst card №4721 [24]; for Na_2SO_3 crystal structure information was taken from Zachariesen et al., with the space group C_{3i} [25] and for sphalerite ZnS from Wyckoff et al., Mincryst card №4449[24]. The experimental sphalerite spectrum was taken from ESRF sulphur XANES database[26].

CHAPTER III RESULTS

In order to perform a full characterization of the particulate matter deposited on filters, both bulk and surface analyses were carried out. This section is therefore organized as follows. The starting point were PIXE (Figure 9) and X-ray fluorescence response experiments, which allowed to list the elements present in the filters. The X-ray fluorescence response for QUI 156, VADO 118 and

The filter code	Elements of interest	PM10 (µg Nm³)	Element concentrations (µg cm²)	Na	Mg	Al	Si	P	S	Cl	K	Ca
QUI156	Fe, Zn, Cr	82,3		3,154	6,851	19,610	36,836	0,056	7,863	0,320	7,857	12,260
VADO118	V, Ni	23,9		3,513	2,234	3,198	6,392	0,096	7,917	0,294	1,734	3,148
VADO028	S, As	49,0		2,187	0,863	3,166	4,851		11,185	0,493	2,146	2,475

PTFE filters	Filter code			Ti	V	Cr	Mn	Fe	Ni	Cu	Zn	As
PIXE analysis	QUI156			1,124	0,061	0,041	0,256	13,889	0,022	0,099	0,258	
	VADO118			0,179	0,153	0,021	0,051	3,104	0,057	0,077	0,348	
	VADO028			0,191	0,031	0,015	0,081	2,818	0,014	0,034	0,353	0,007

Filter code				Se	Br	Rb	Sr	Zr	Mo	Ba	Pb
QUI156				0,009	0,039	0,130		0,028			0,110
VADO118				0,006	0,032	0,016	0,012				0,039
VADO028				0,007	0,049	0,010	0,018				0,132

Figure 9 Element concentrations in QUI 156, VADO 118 and VADO 28 filters by PIXE analysis (data was kindly provided by the group of Prof. Tositti)

VADO 28 is reported in the Appendix Figures A1, A2 and A3, respectively. As it is shown below on Figure 9, sulphur is a dominant inorganic non-metal element in the PM. Also, large quantities of Na, Mg, Al, Ca and Fe metals are present. These experiments set the feasibilities for each metal core K-edge experiments. Then, considering the concentrations of elements and peculiarities of synchrotron radiation experiment, a number of elements were analysed by XAS experiment (bulk) depending on their relative concentration. Later, K-edge reference spectra of reference compounds were recorded for these elements. In case of the absence of experimental reference data, XANES calculations using FDMNES code were performed. Finally, in order to analyse the surface of the filters, XPS experiments were carried out.

III-1-1 Results obtained with experimental reference XANES spectra

III-1-1-1 Sulphur

Sulphur was present in all filters according to PIXE elemental analysis and fluorescence response data, and in VADO 28 filter there was more sulphur, 11.2 $\mu g/cm^2$, than in VADO 118 and QUI 156 filter (roughly equal amounts of 7.9 $\mu g/cm^2$). The comparative XANES S K-edge spectra of all filters are shown below on Figure 10. As we can see the VADO 28 has a weak peak at lower energies which is absent in other filters. QUI 156 filter shows more evident spectral features than the VADO filters.
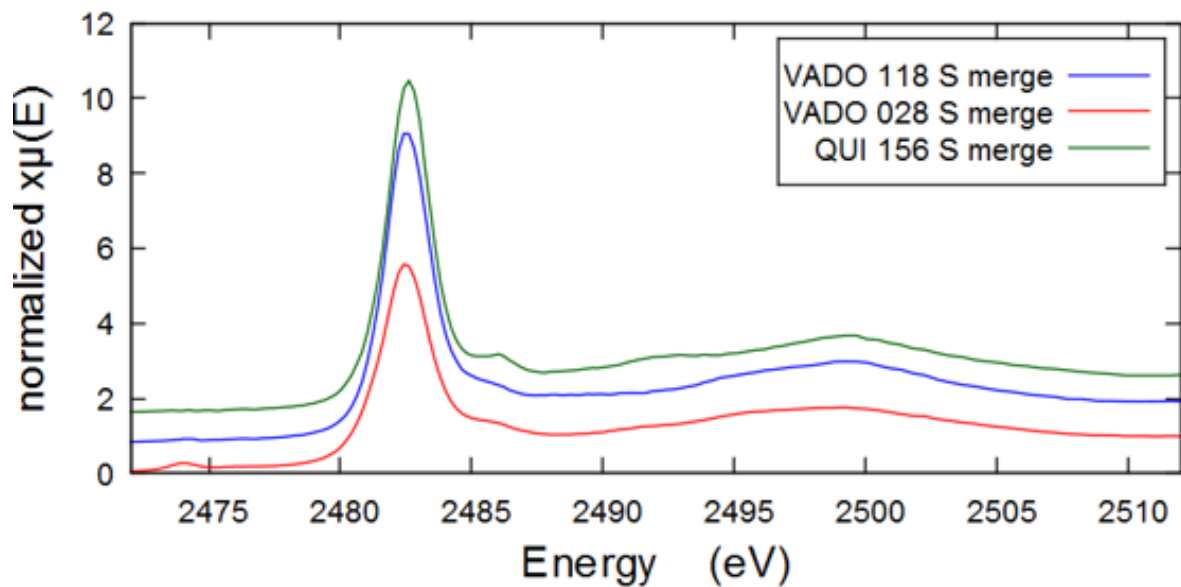
Figure 10 Comparative sulfur K-absorption edge spectra of VADO 118, VADO 28 and QUI 156 filters

The results of linear combination fitting for VADO 28 performed in ATHENA are demonstrated below on Figure 11 and fits for QUI 156 and VADO 118 filter can be found in the Appendix Figures A4 and A5.
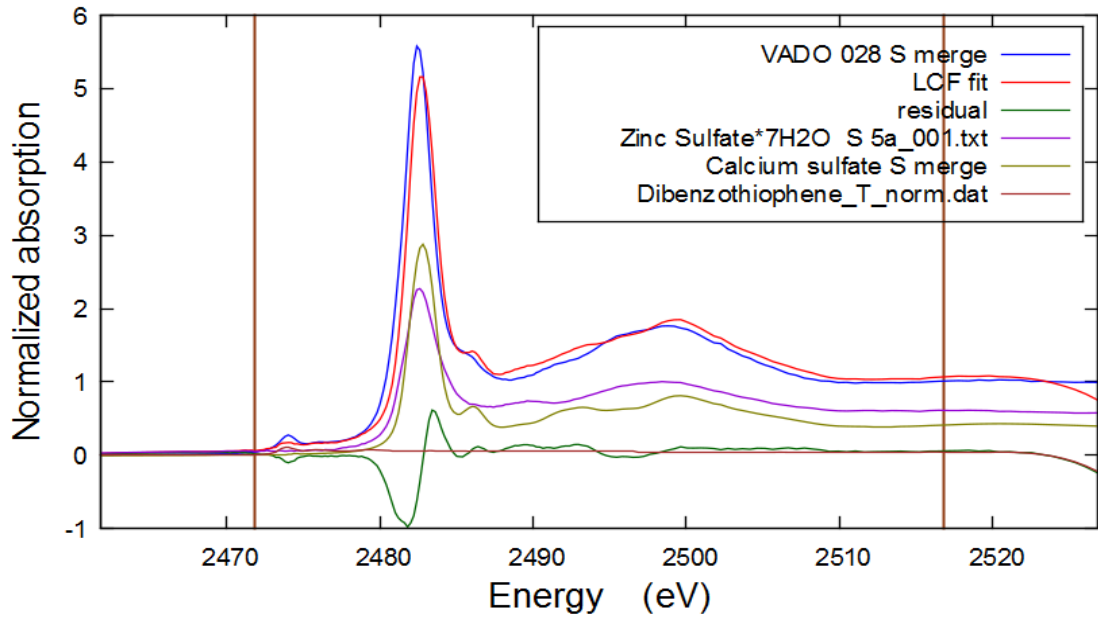
Figure 11 Results of linear combination fitting in ATHENA of S K-edge spectrum of VADO 28 filter

III-1-1-2 Zinc

Zinc was present in all filters according to PIXE elemental analysis and fluorescence response data, but Zn K-edge spectra were collected only for QUI 156 and VADO 118. The comparative XANES Zn K-edge spectra of all filters are shown below on Figure 12.
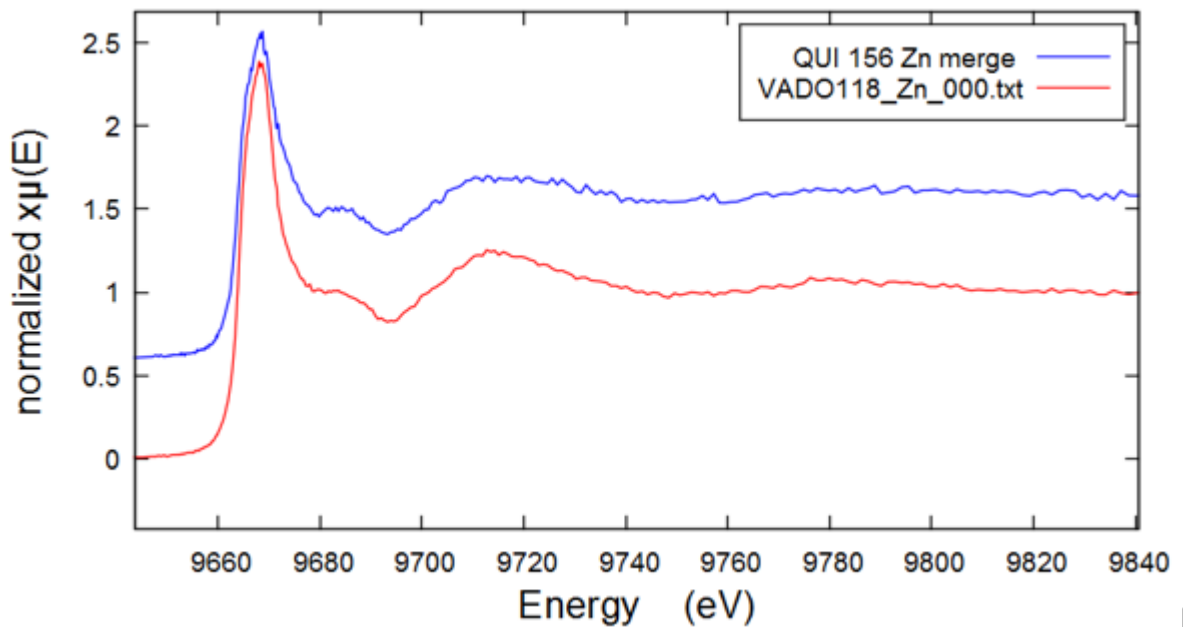
Figure 12 Comparative zinc K-edge XAFS spectra of the QUI 156 and, VADO 118 filters
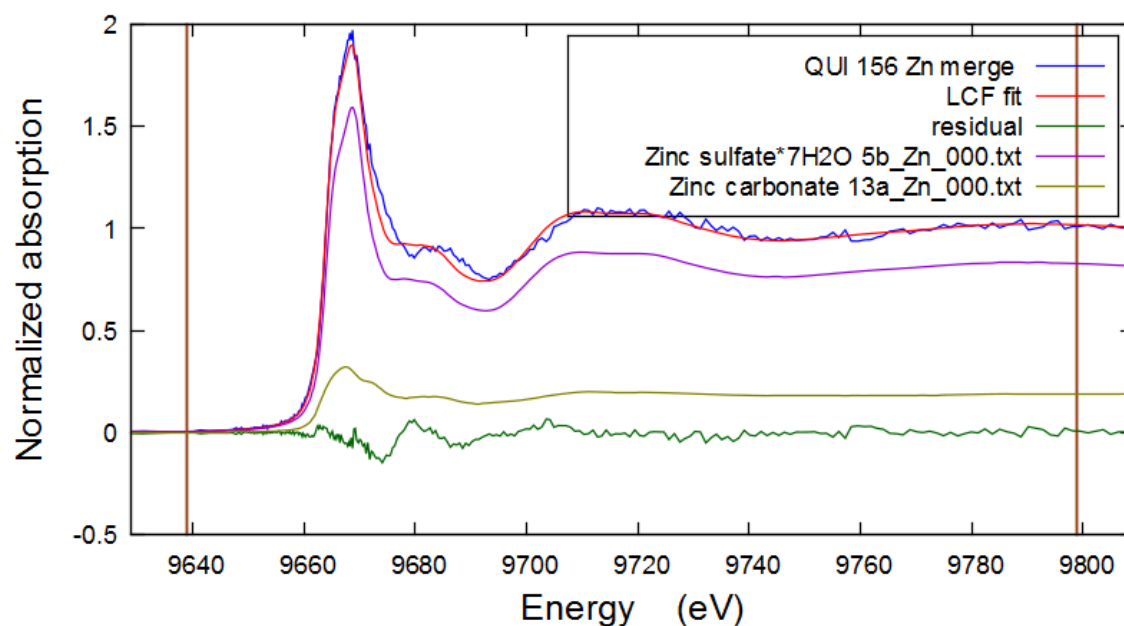
Figure 13 Results of linear combination fitting in ATHENA of QUI 156 Zn K-edge XANES spectrum

The results of linear combination fitting for QUI 156 performed in Athena are demonstrated above on Figure 13 and fits for VADO 118 filter can be found in the Appendix Figure A6.

III-1-1-3 Calcium

Calcium is present in abundance in all samples according to PIXE elemental analysis and fluorescence response data, therefore Ca K-edge spectra were collected for all filters. The comparative XANES Ca K-edge spectra of all filters are shown below on Figure 14.
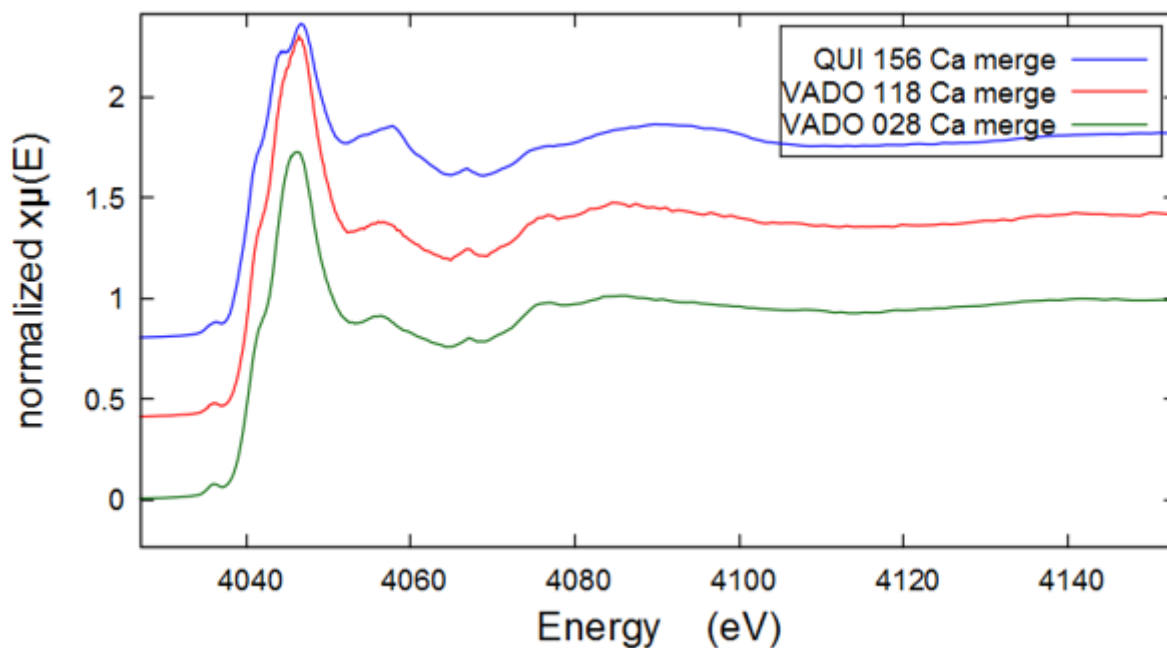
Figure 14 Comparative calcium K-edge XAFS spectrum of the QUI 156, VADO28 and VADO 118 filters
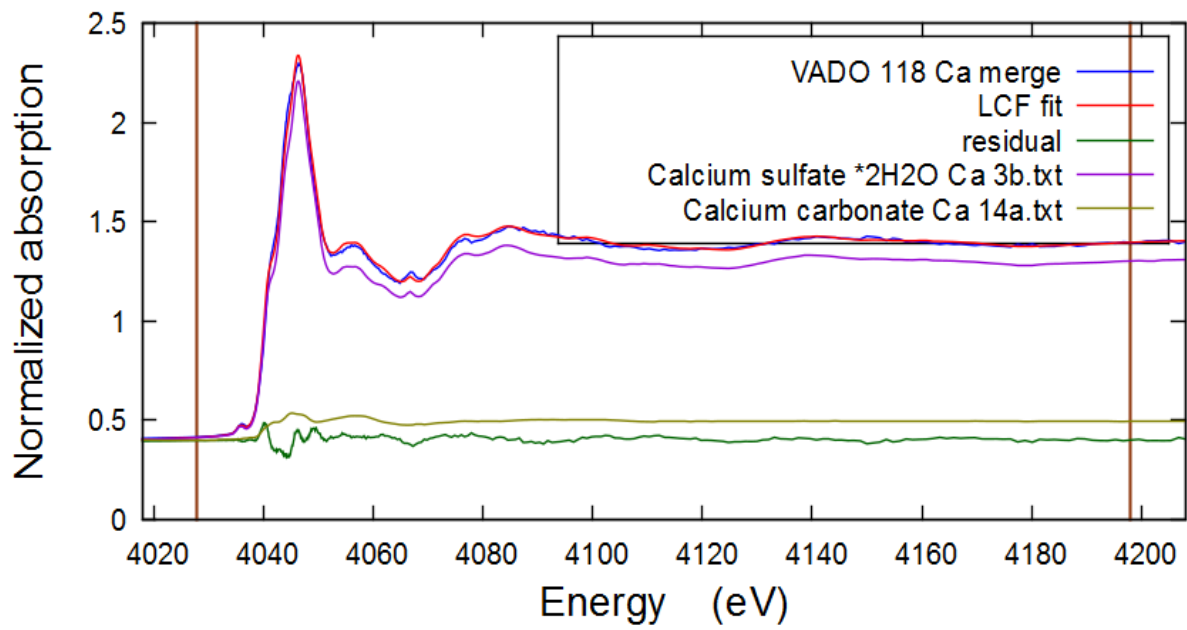
Figure 15 Results of linear combination fitting in ATHENA of VADO118 Ca K-edge XANES spectrum

Results of linear combination fitting for VADO 118 performed in Athena are demonstrated above on Figure 15 and fits for QUI 156 and VADO 28 filters are shown in the Appendix Figures A7-8.

Iron was found in all filters according to fluorescence response data and PIXE elemental analysis, especially in abundance in QUI 156 filter, 13.89 μg/cm^2. The comparative XANES Fe K-edge spectra of all filters are shown below on Figure 16. The results of linear combination fitting for QUI 156 performed in Athena is demonstrated below on Figure 17 and fits for VADO 118 and VADO 28 filters are shown in Appendix Figures A9 and A10.
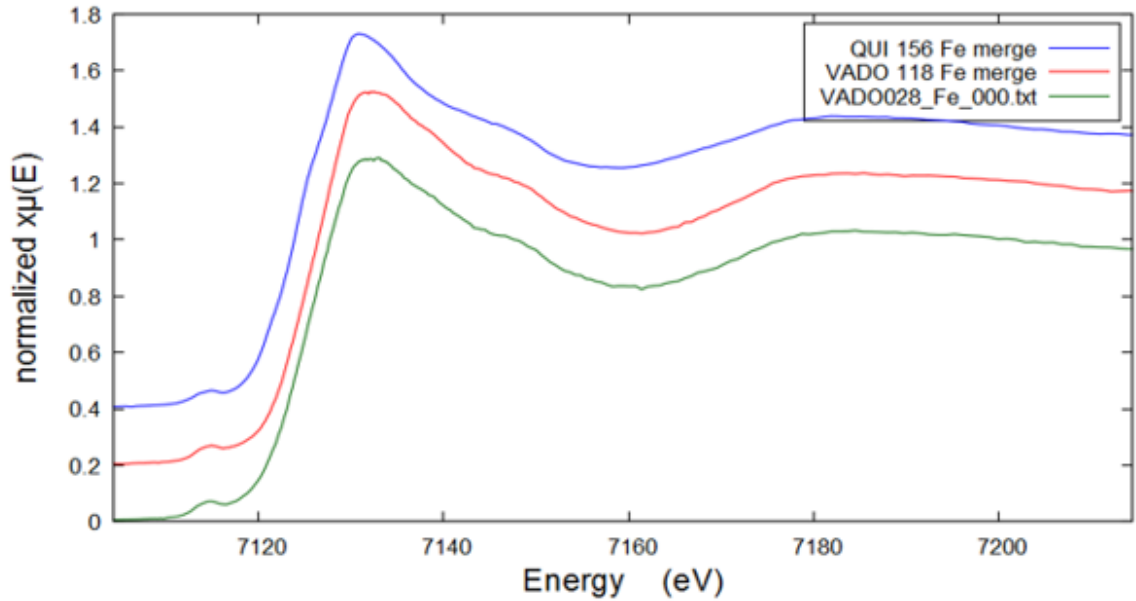
Figure 16 Comparative iron K-edge XANES spectrum of the QUI 156, VADO 28 and VADO 118 filters
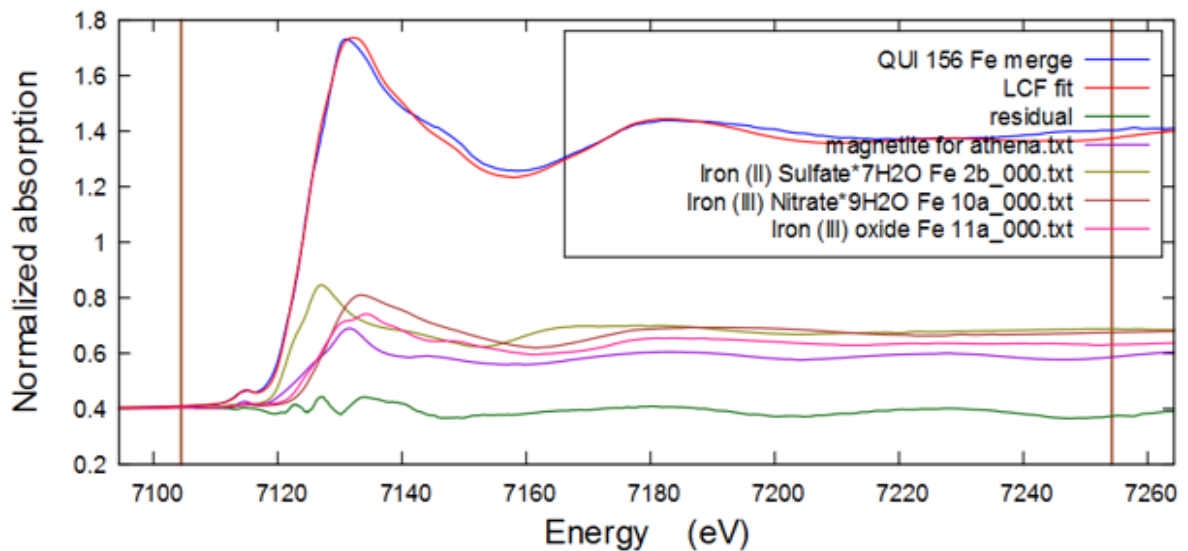
Figure 17 Results of linear combination fitting in ATHENA of QUI 156 Fe K-edge XANES spectrum

III-1-2 Results obtained with calculated reference XANES spectra

III-1-2-1 Manganese

Manganese was present in all filters according to PIXE elemental analysis and fluorescence response data, but the amounts were rather low for VADO filters. QUI 156 filter had higher amount of Mn, 0.256 µg/cm². The comparative XANES Mn K-edge spectra of all filters are shown below on Figure 18.
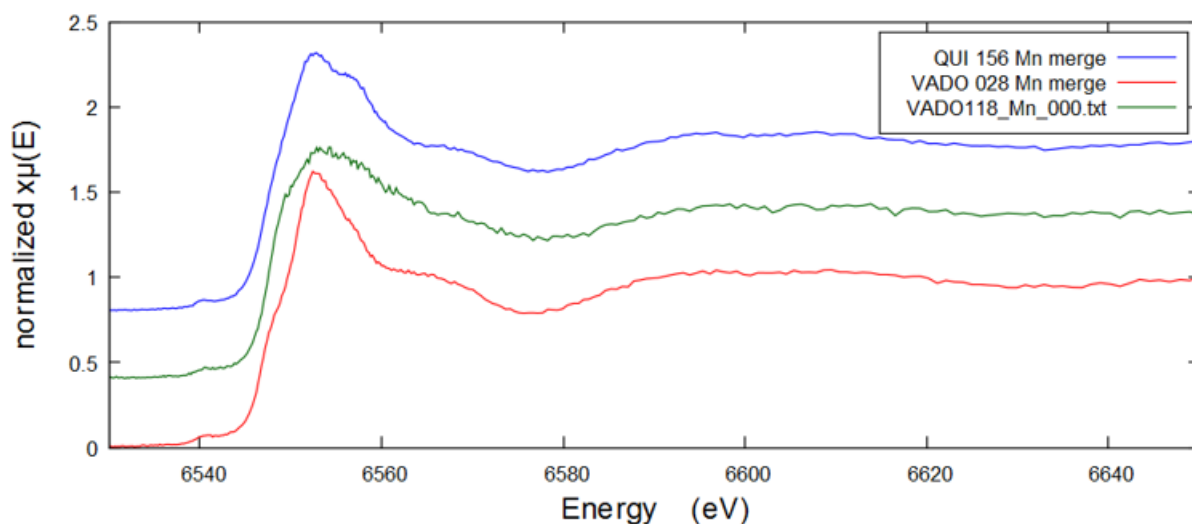
Figure 18 Comparative manganese K-edge XAFS spectra of the QUI 156, VADO28 and VADO 118 filters

Results of linear combination fitting for VADO 28 performed in Athena are demonstrated below on Figure 19. The fits for QUI 156 and VADO 118 filters are demonstrated Appendix Figures A11 and A12.
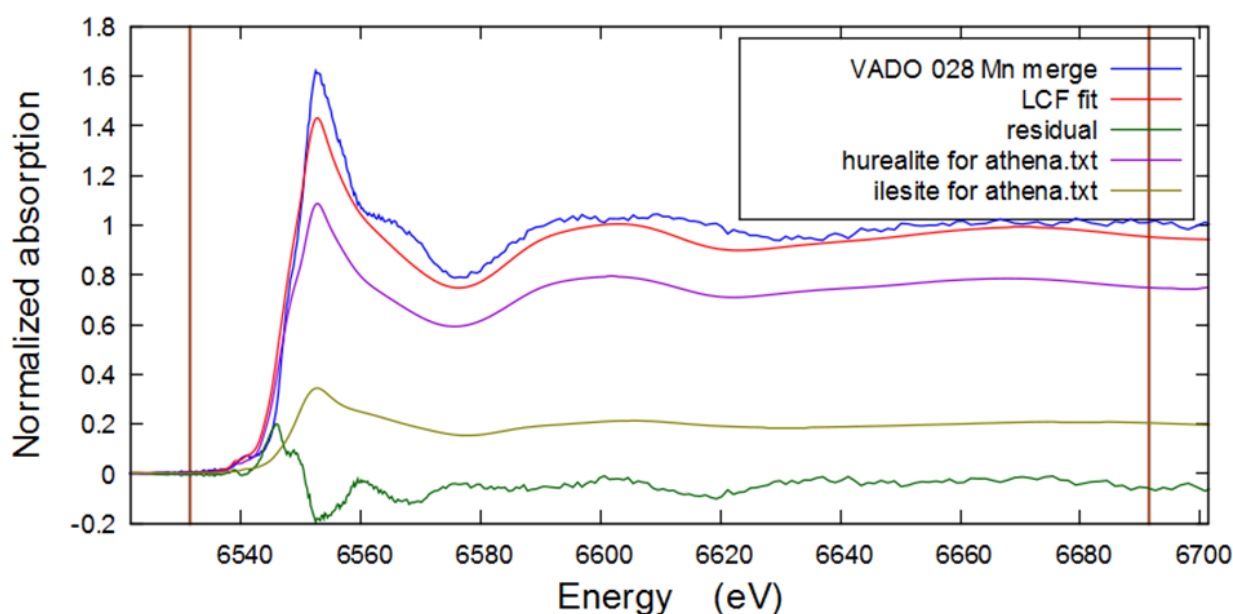
Figure 19 Results of linear combination fitting in ATHENA of VADO 28 Mn K-edge XANES spectrum

24

Chromium was present in all filters, but in very small amounts. From fluorescence response data and PIXE elemental analysis, QUI 156 filter has the highest amount of 0.041 μg/cm^2, therefore the Cr K-edge spectrum of QUI filter only was recorded. No reference data were collected for Cr samples, so the speciation was performed based on theoretical calculations only. The results of linear combination fitting for QUI 156 performed in Athena are demonstrated below on Figure 20.
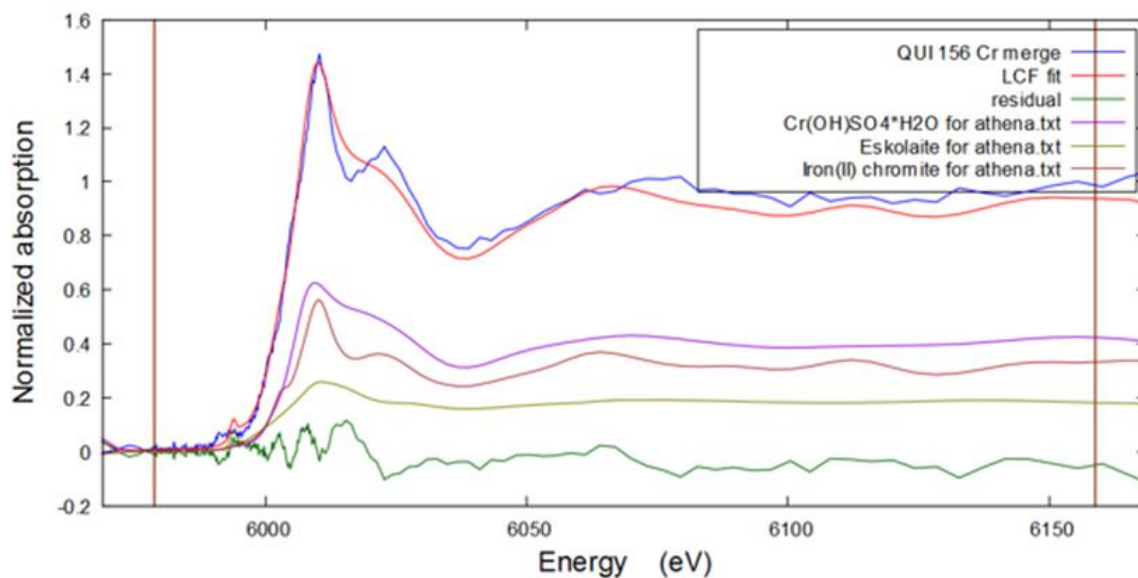
Figure 20 Results of linear combination fitting in ATHENA of QUI 156 Cr K-edge XANES spectrum

III-1-2-3 Copper

Copper content was very low, therefore XANES Cu K-edge spectrum of a rather low S/N ratio was obtained only for QUI 156 filter, which had the highest amount of Cu among other filters 0.099 µg/cm^2 (based on PIXE analysis and fluorescence response data). No reference spectra were recorded for Cu samples, so the assignment was performed based on FDMNES calculations only. The results of linear combination fitting for QUI 156 performed in Athena are demonstrated below on Figure 21.
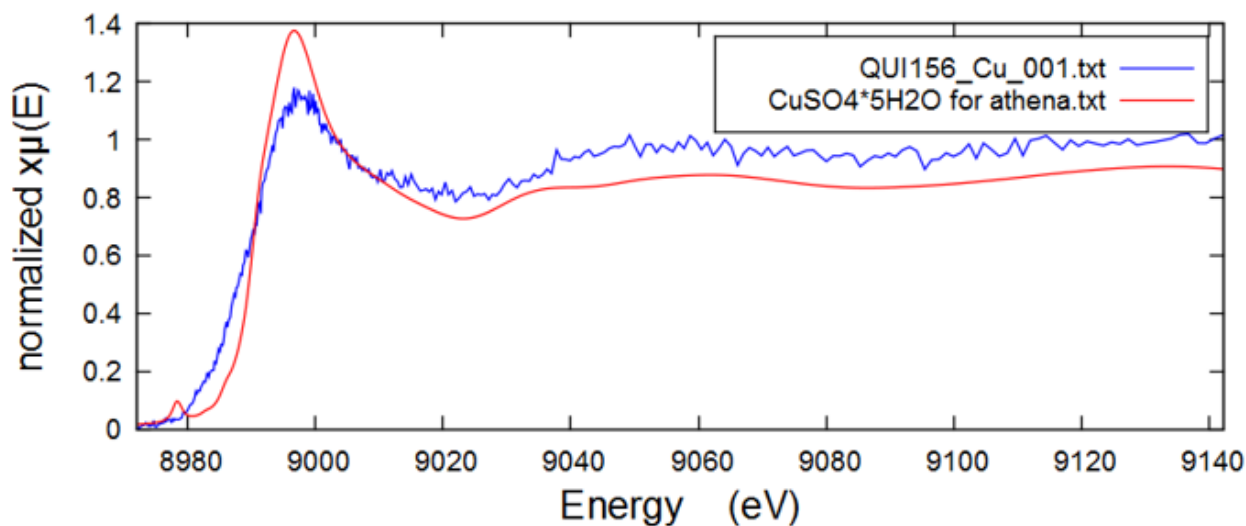
Figure 21 Results of a linear combination fitting in ATHENA of QUI 156 Cu K-edge XANES spectrum

The vanadium XAFS spectrum was collected for all filters, however, the vanadium content was rather low to give a good S/N spectrum (from PIXE analysis and fluorescence response data). The XAFS spectrum of the QUI 156, shown in Figure 22 below demonstrates a limitation of XAFS spectroscopy. The PM is a complex mixture of different elements, therefore the EXAFS region of one element might interfere with another element. In our case a strong L_{II}-edge of barium limits the EXAFS region for vanadium to about 120 eV, thus impeding the EXAFS analysis.. Nonetheless, the presence of barium does not affect the observation of the vanadium K-edge XANES region, and that information was still available for interpretation of the speciation of vanadium.
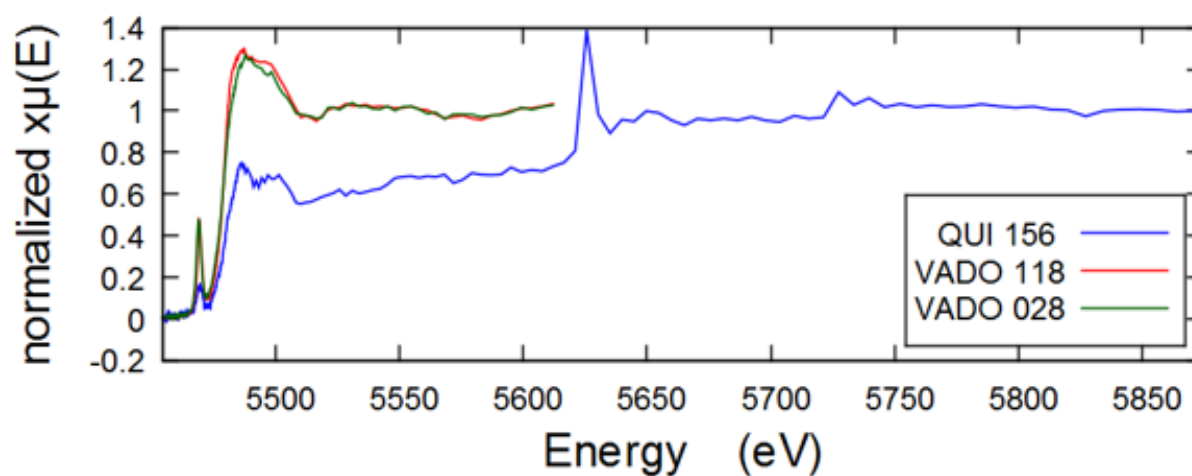
Figure 22 Comparative vanadium K-edge XAFS spectra of the QUI 156, VADO 118 and VADO 28 filters. Note a prominent Ba LII-edge peak at ~5620 eV.

27

III-1-2-5 Titanium

The titanium XAFS spectrum was collected for QUI 156 and VADO 28 filters, however, the titanium content was rather low in both filters to give a good S/N spectrum (from PIXE analysis and fluorescence response data). The comparative XAFS spectra of the QUI 156 and VADO 28 are shown on Figure 23 below. The spectrum of QUI 156 demonstrates a limitation of XAFS spectroscopy as in the case of vanadium. Here we see again barium limiting the EXAFS region of QUI 156. Strong L_{III}-edge of barium can be clearly seen on the spectra below. The results of FDMNES calculations are plotted on Figure 24 below.
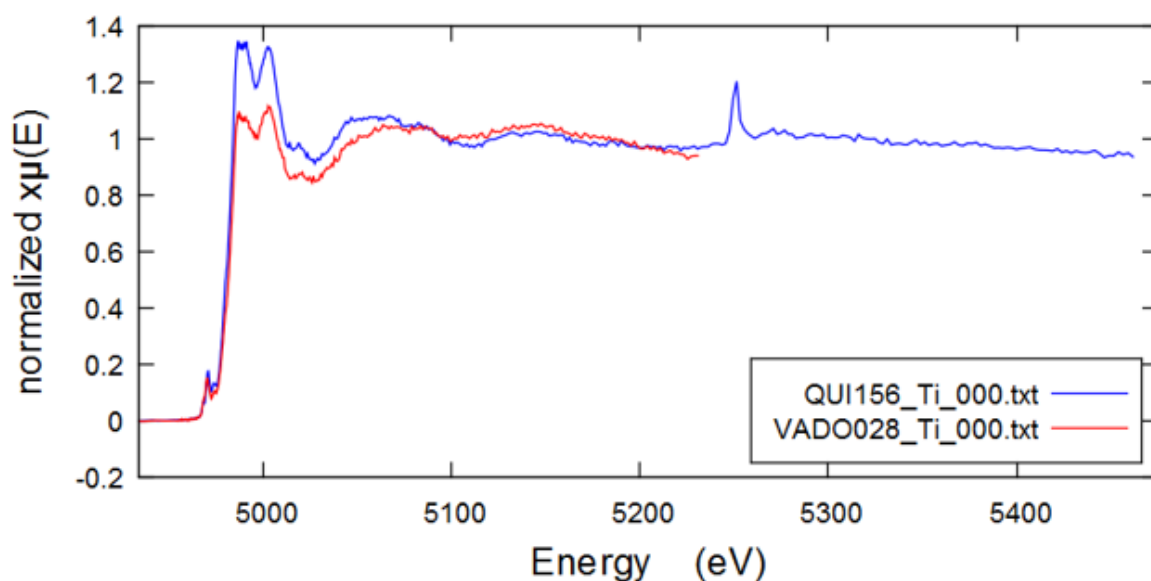
Figure 23 Comparative titanium K-edge XAFS spectra of the QUI 156 and VADO 28. Note a prominent Ba L_{III}-edge peak at ~5240 eV.
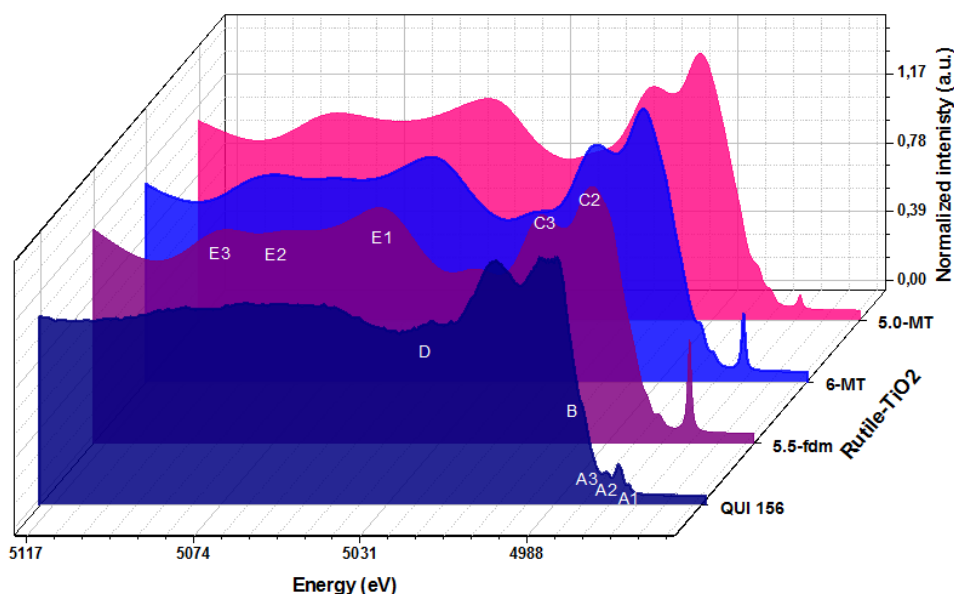
Figure 24 Comparative spectra of experimental titanium K-edge XANES spectra of QUI 156 (first), and calculated spectra of TiO2-rutile of different cluster radii: 5.5Å with FDM (second), 6Å with MT (third) and 5Å with MT methods (the last).

28

According to PIXE elemental analysis nickel was present in all filters in very low quantities. XANES Ni K-edge spectrum was collected only for VADO 118 filter, which had the highest amount of Ni among other filters 0.057 μg/cm^2 (from PIXE analysis and fluorescence response data). No reference spectra were recorded for Ni samples, so an assignment was performed based on calculations only. However, it is important to note that a fair LCF fit might be due to imprecise spectra calculations and to a non-suitable broadening function. Nevertheless, the results of linear combination fitting for VADO 118 performed in ATHENA are demonstrated below on Figure 25.
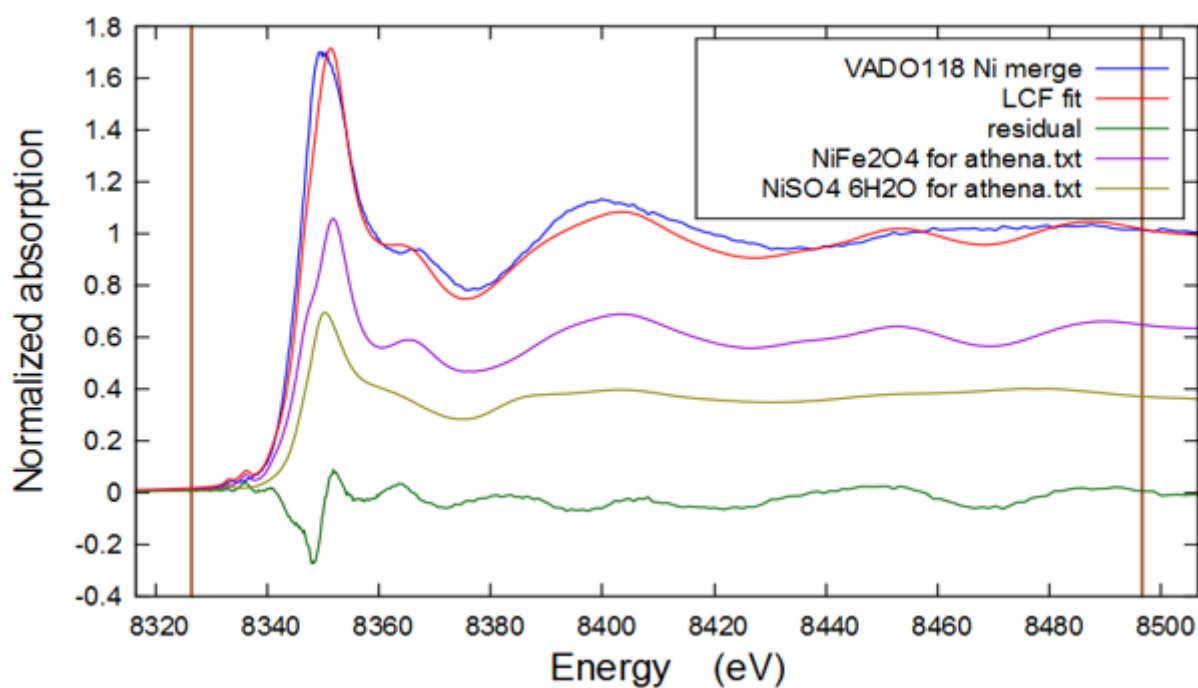
Figure 25 Results of linear combination fitting in ATHENA of VADO 118 Ni K-edge XANES spectrum

III-2-1 Comparative survey scans

The multiple possible elements present in particulate matter can be identified in XPS survey scan because it spans a broad range of ejected core-shell electron energies. Figure 26 shows typical survey scans of PM collected on quartz (VADO118, VADO28) and PTFE (QUI 156) filters.
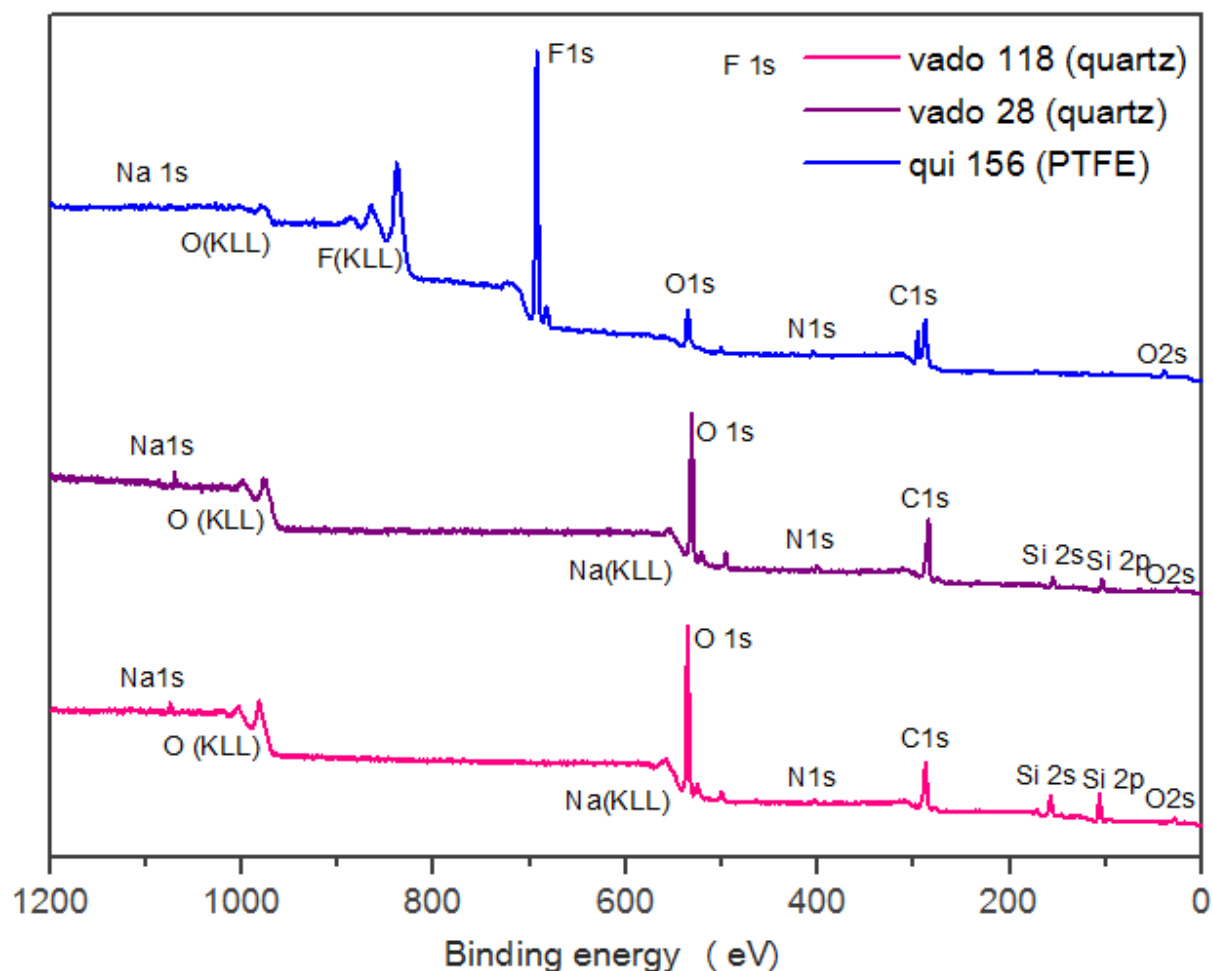
Figure 26 A comparative "survey scan" over electron-binding energies characteristic of core shell electronic energy levels of VADO 118, VADO 28 and QUI 156 filters before sputtering. The individual peaks are labeled by the element and core shell energy. Other peaks arising from secondary Auger electrons are labeled in standard KL format.

It can be noticed immediately that the comparative survey spectra (Figure 26) of two VADO filters are similar, revealing the presence of C 1s, O 1s, N 1s, Si 2p and Na 1s. Quartz – filter material, gives rise to Si 2p and O 1s signals. For QUI 156 filter the spectrum shows C 1s, O 1s, N 1s and F 1s peaks. The fluorine signal and double peak for carbon come from polytetrafluoroethylene (PTFE) - filter material. VADO 28 was collected using LAXL lens mode and a flood gun, however the survey spectrum does not reveal any significant differences.

III-2-2 Carbon

In order to identify the chemical state of the atomic species detected, the detailed spectra were collected. The acquisition energy range for C 1s spectra spanned from 270 eV to 305 eV. The detailed C1s spectra of QUI 156, VADO 118 and VADO 28 "new" with fitted backgrounds, are shown on Figures 27 a, b and c respectively. The VADO 118 C 1s spectra after 2, 10 and 30 min of sputtering can be found in Appendix Figures A13a-c.
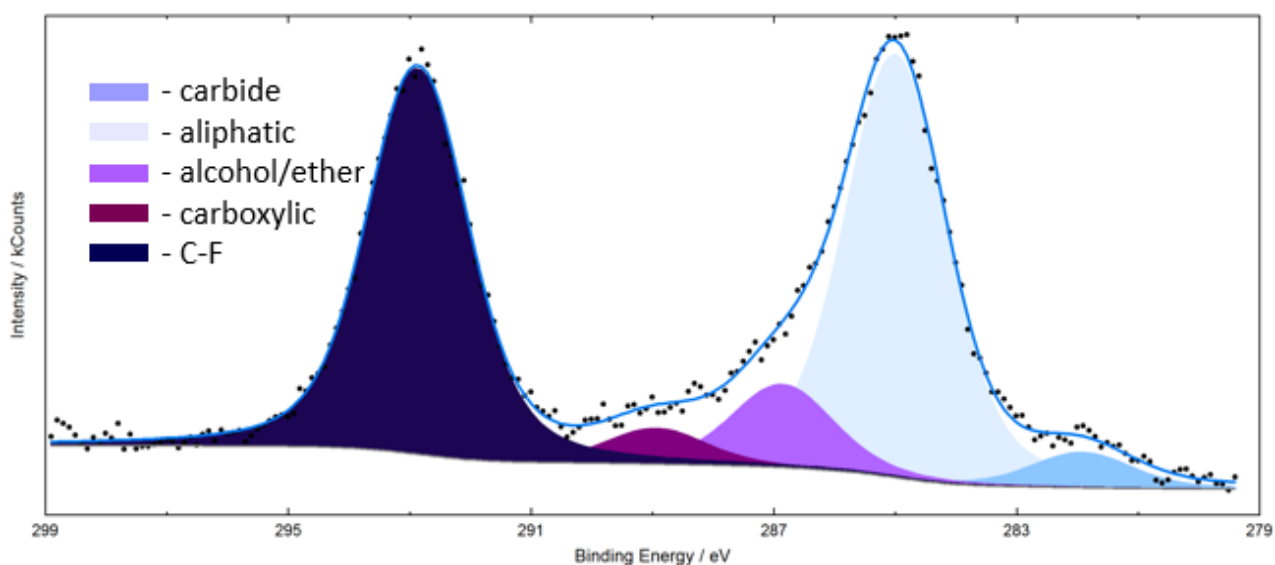
Figure 27a A detailed C1s XPS spectrum of QUI 156 resolved into signals assigned as reported in the discussion part
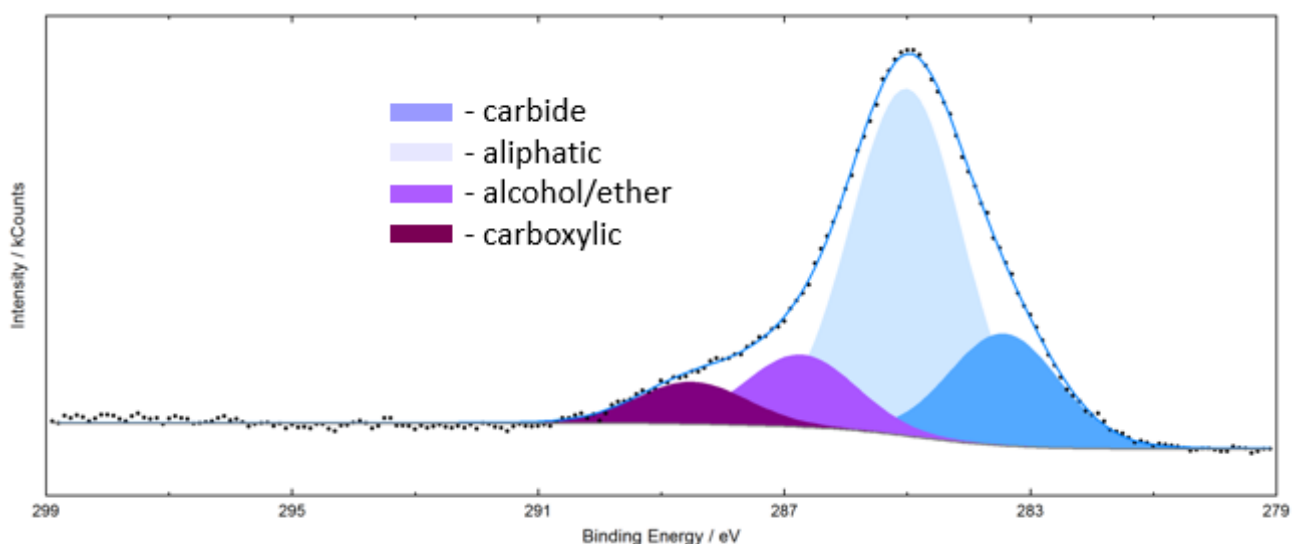
Figure 27b A detailed C1s XPS spectrum of VADO118 resolved into signals assigned as reported in the discussion

Figure 27c A detailed C1s XPS spectrum of VADO 28 "new" resolved into signals assigned as reported in the discussion part

III-2-3 Oxygen

O 1s detailed spectra were acquired with energy range of 515-555 eV. Background-subtracted O 1s spectra of the VADO 28 "new" shown on Figure 28 below. The O1s spectra for VADO 118 at 0, 2, 10 and 30 min of sputtering and QUI 156 can be found in the Appendix Figures A14 a-e.
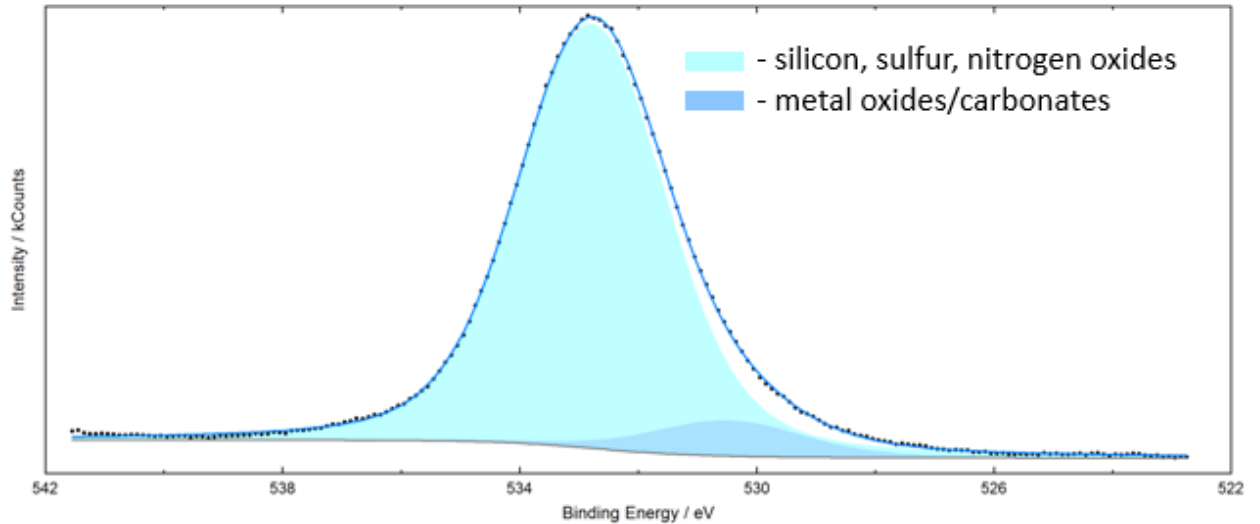
Figure 28 A detailed O1s XPS spectrum of VADO 28 "new" resolved into signals assigned as reported in the discussion part

III-2-4 Silicon

Si2p detailed spectra were acquired in the 90-120 eV energy range. Si2p spectra of the VADO 28 "new" with fitted background are shown on Figure 29 below.
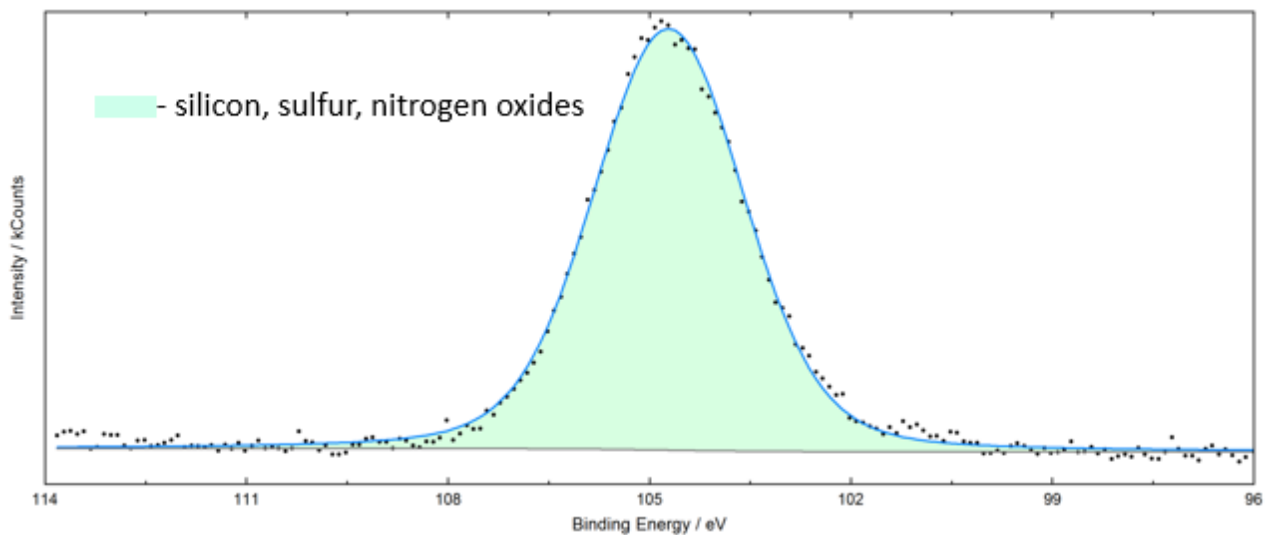
Figure 29 A detailed Si2p XPS spectrum of VADO 28 "new" resolved into signals assigned as reported in the discussion part

III-2-5 Nitrogen

N1s detailed spectra were acquired in the energy range of 385-415 eV. Background-fitted N1s spectra of VADO 28 "new", VADO 118 after 10 min of sputtering and QUI 156 are demonstrated on Figures 30 a, b and c, respectively. The N 1s spectra for VADO 118 at 0, 10 and 30 min of sputtering are shown in the Appendix A15a-c.
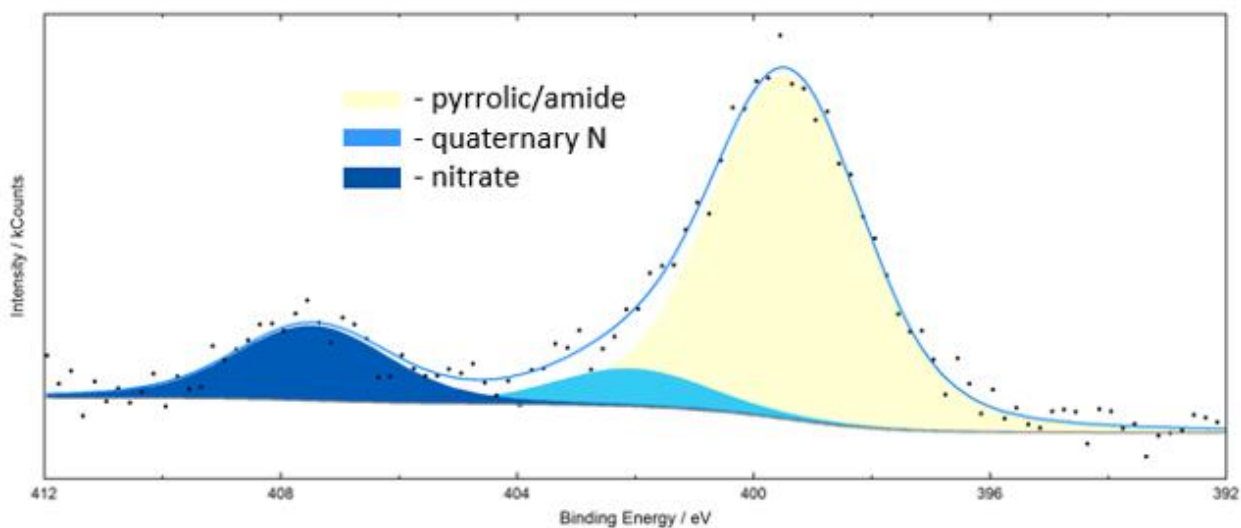
Figure 30a A detailed N1s XPS spectrum of VADO 28 "new" resolved into signals assigned as reported in the discussion part
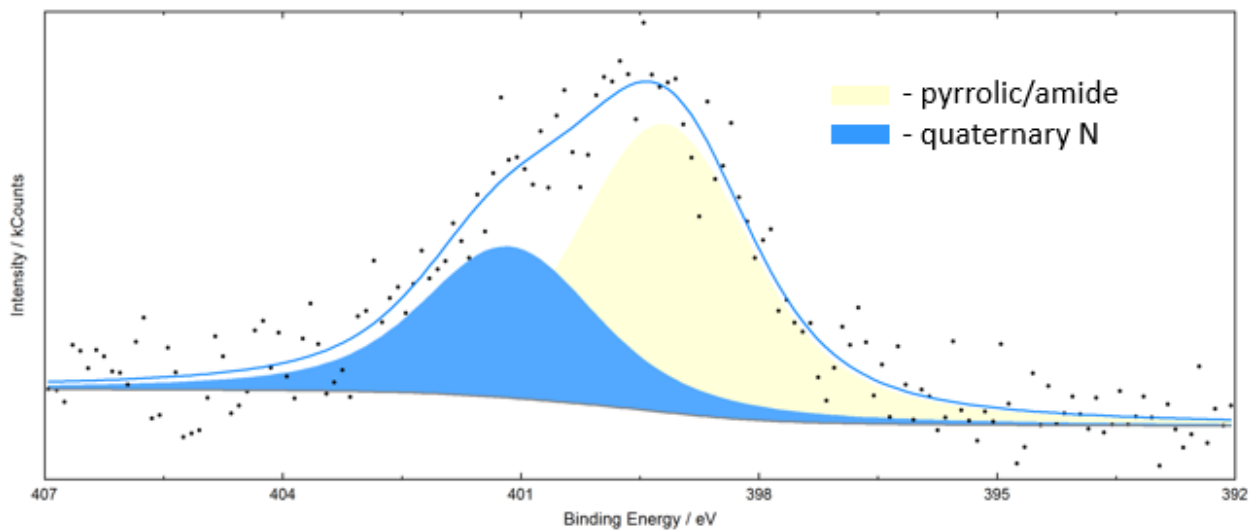
Figure 30b A detailed N1s XPS spectrum of VADO 118 after 10 min of sputtering resolved into signals assigned as reported in the discussion part
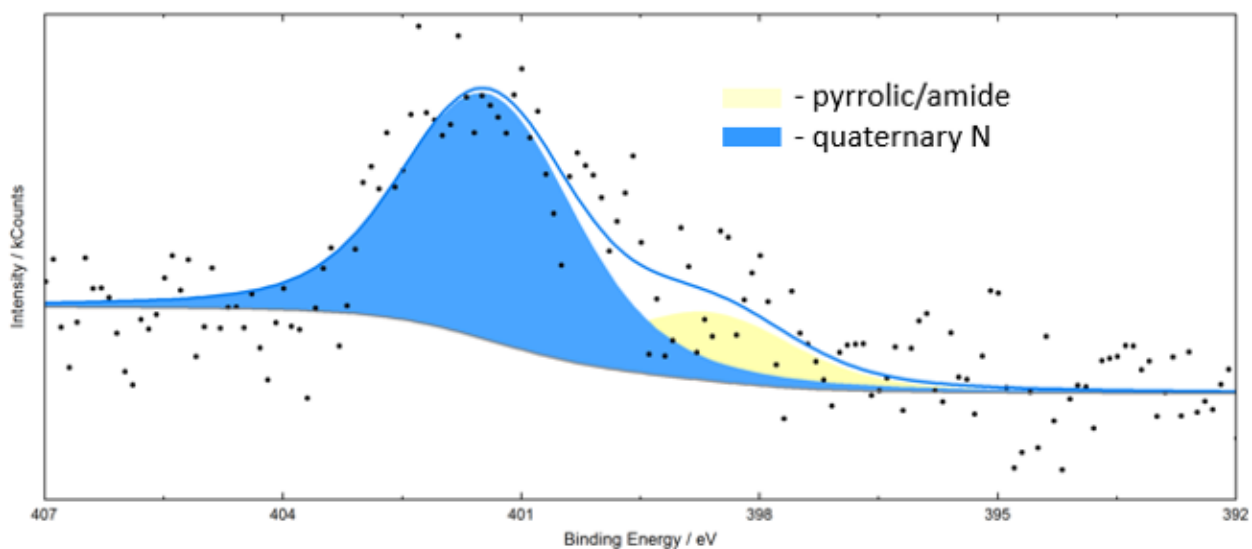
Figure 30c A detailed N1s XPS spectrum of QUI 156 resolved into signals assigned as reported in the discussion part

III-2-6 Sodium

Na 1s was evident only in VADO 118 and VADO 28 survey spectra, and the detailed spectra were acquired in the energy range of 1055-1085 eV. Background-subtracted Na1s spectra of VADO 118 after 10 min of sputtering can be seen on Figure 31.
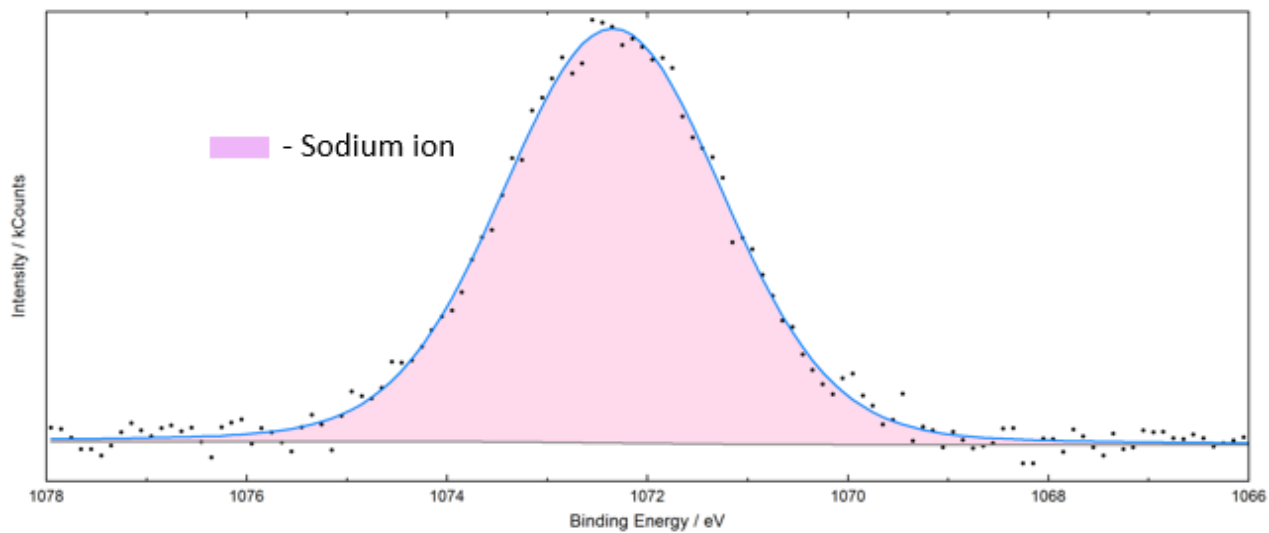
Figure 31 Na1s XPS spectrum of VADO 118 after 10 min of sputtering resolved into signals assigned as reported in the discussion part

Fe 2p became noticeable in VADO 118 survey spectrum only after 10 min of sputtering and the detailed spectrum was collected at the energy range of 690-745 eV. However, the spectrum after 10 min of sputtering is too noisy to obtain a good fit. Fe 2p spectra of VADO 28 "new" and VADO 118 after 30 min of sputtering also have low S/N ratio, nonetheless the fitting was attempted as shown on Figures 32 a and 32b.
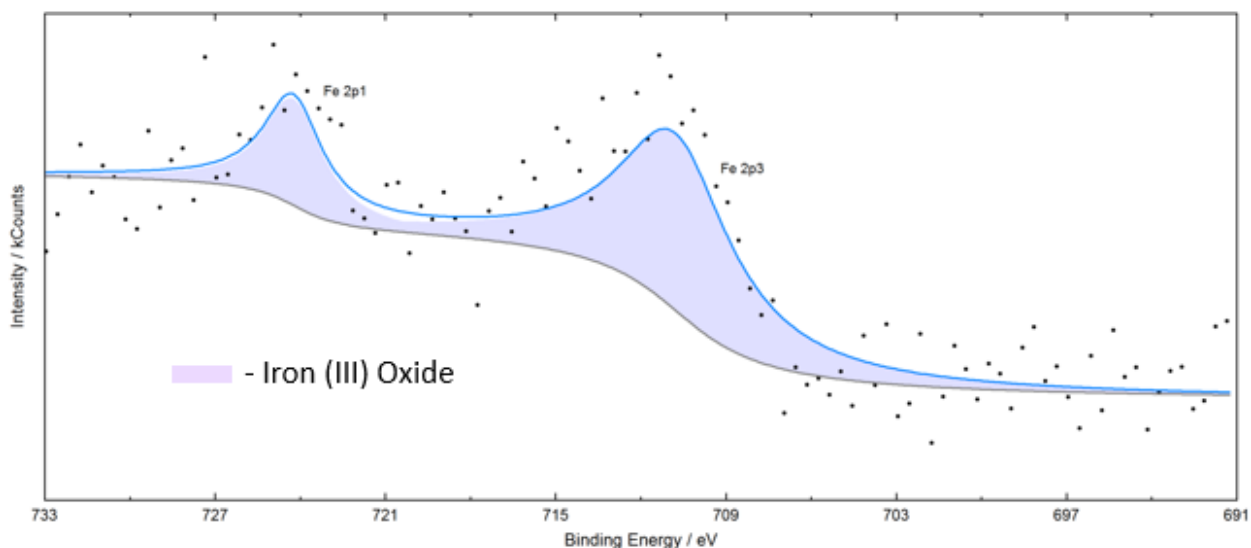
Figure 32a A detailed Fe2p XPS spectrum of VADO 28 "new" resolved into signals assigned as reported in the discussion part
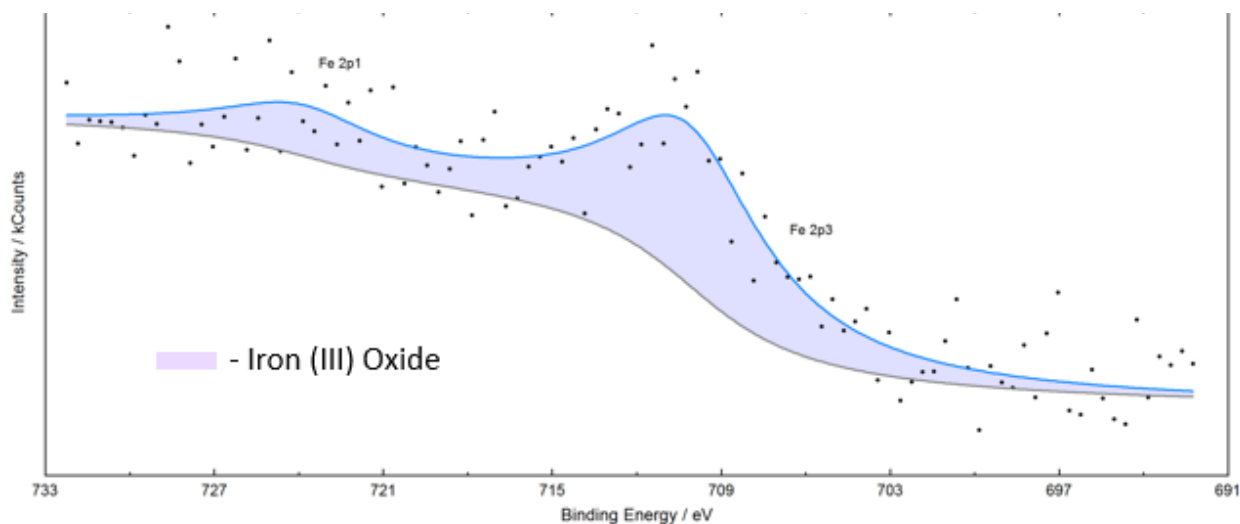
Figure 32b A detailed Fe2p XPS spectrum of VADO 118 after 30 min of sputtering resolved into signals assigned as reported in the discussion part

III-2-8 Calcium

Ca 2p became evident in VADO 118 survey spectrum only after 30 min of sputtering and the detailed spectrum was collected at the energy range of 335-370 eV. Ca 2p spectra of VADO 118 after 30 min of sputtering and VADO 28 "new" after 10 min of sputtering with fitted background are shown on Figure 33a and 33b.
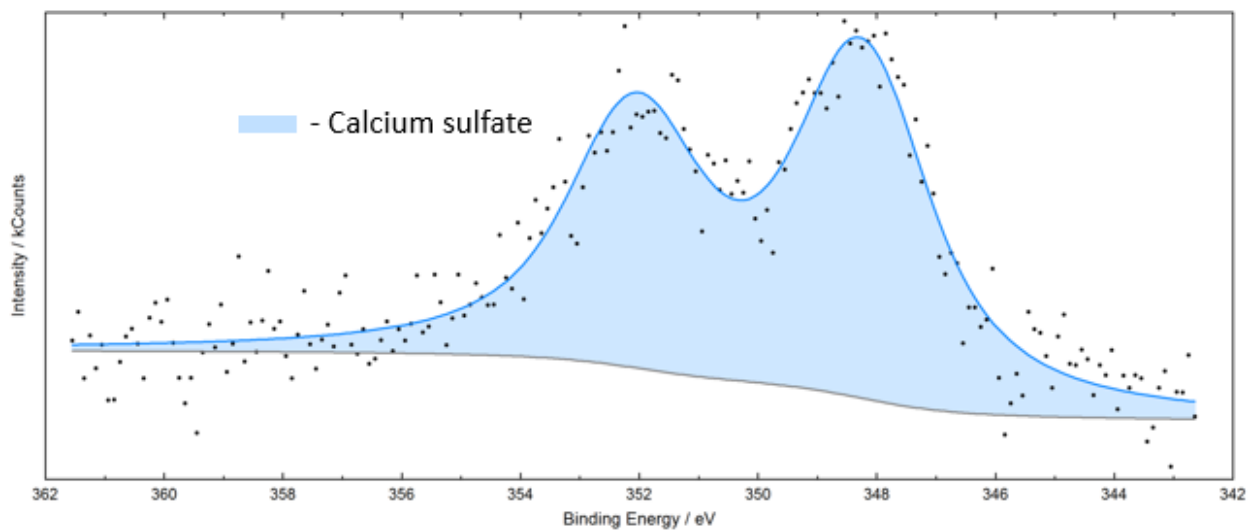
Figure 33a A detailed Ca2p XPS spectrum of VADO 118 after 30 min of sputtering resolved into signals assigned as reported in the discussion part
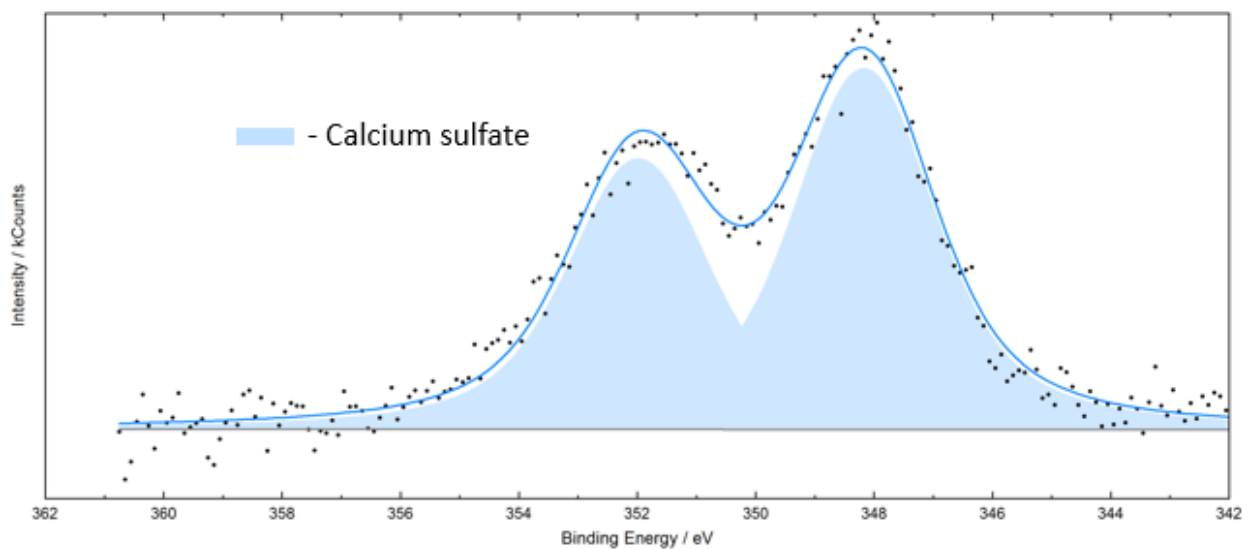
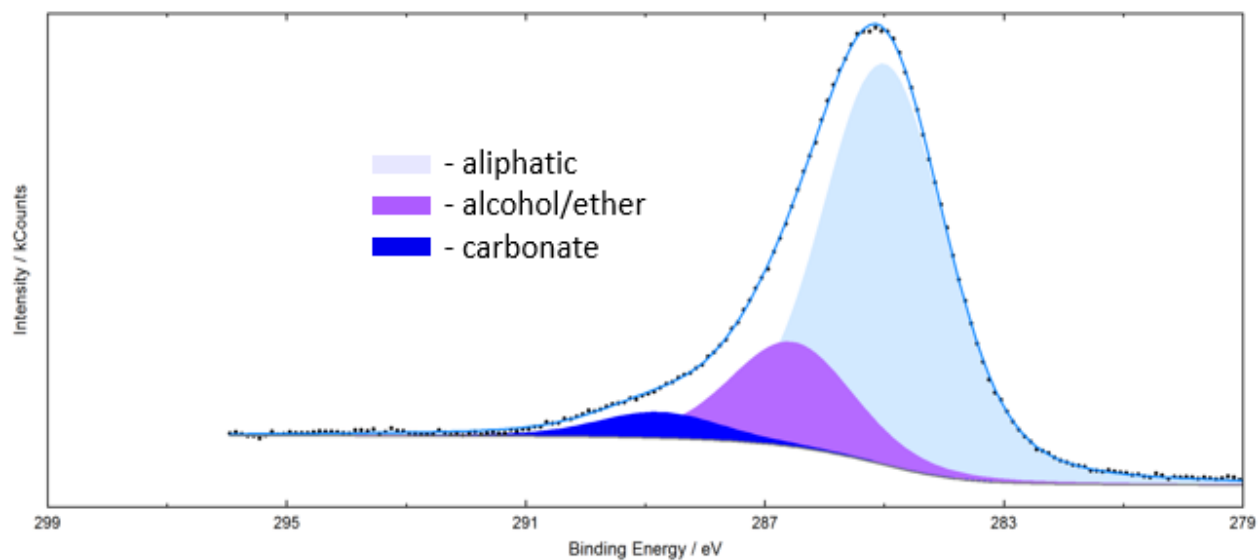Figure 33b A detailed Ca2p spectrum of VADO 28 "new" (bottom) resolved into signals assigned as reported in the discussion part

CHAPTER IV DISCUSSION

Metallic components of ambient air particulate matter are often cited as those most likely to exert health effects. They are generated by metallurgical processes, from impurities in fuel additives and in non-exhaust emissions (from mechanical abrasion such as brake- and tyre wear on vehicles). Interest is mainly targeted on transition metals such as Fe, V, Ni, Cr and Cu based on their potential to produce reactive oxygen species in biological tissues. A large fraction of ambient PM in many areas is derived from combustion processes and therefore, contains significant amounts of black carbon and organic carbon. Carbonaceous aerosol also originates from biological sources (e.g. viruses, pollen grains, plant debris) and contains secondary organic aerosol formed from the oxidation of biogenic and anthropogenic hydrocarbon emissions. More than 200 organic species have been identified, including alkanes, alkenes, aromatics, oxygenated compounds (including aldehydes, ketones and carboxylic acids), amino compounds, nitrates, polyaromatic hydrocarbons (PAH) and PAH derivatives[10]. Another widespread component is a wind-blown mineral dust tends to be made of mineral oxides. Sea salt is considered the second-largest contributor in the global aerosol budget, and consists mainly of NaCl originated from sea spray; other constituents of atmospheric sea salt reflect the composition of sea water, and thus include Mg, sulphate, Ca, K etc. In addition, sea spray aerosols may contain organic compounds, which influence their chemistry. Secondary particles originate from the oxidation of primary gases such as S and N oxides into sulphuric acid (liquid) and nitric acid (gaseous). The precursors for these aerosols— i.e. the gases from which they originate—may have an anthropogenic origin (from fossil fuel or coal combustion) and a natural biogenic origin. In the presence of ammonia, secondary aerosols often take the form of ammonium salts; i.e. $(NH_4)_2SO_4$ and NH_4NO_3 (both can be dry or in aqueous solution); in the absence of ammonia, secondary compounds take an acidic form as sulphuric acid (liquid aerosol droplets) and nitric acid (atmospheric gas), all of which may contribute to the health effects of particulates[15], [27]. In this section we show how many of the compounds listed above were identified by us as components of VADO and QUI filters.

The discussion part is presented according to an element under investigation. These elements are presented in the following order: S, Fe, Ca, Ti, V, Cr, Mn, Cu, Zn, Ni, C, O, N, Na and Si, because of the different joint experimental and theoretical approaches used for their analysis. In the discussion part we show how we have successfully gone beyond just elemental characterization. By using core-level spectroscopic techniques we were able to obtain oxidation states, local structure arrangement and symmetry around selected sites and element quantification of different layers.

Sulphur is generally found in atmospheric aerosols, plus it was the only non-metal XAS spectra of which we have collected. Therefore, we start the discussion with sulphur. The position of a white line of recorded S K-edge spectra at 2482 eV revealed that our sulphur has oxidation state 6+. Then, a linear combination fitting in ATHENA was performed as shown on for VADO 28 on Figure 11 and in the Appendix Figures A4 and A5 for QUI 156 and VADO 118 filters. The LCF fit for VADO 118 showed that the main component is $CaSO_4*2H_2O$. The spectral shape of QUI 156 filter resembles almost completely the one of $CaSO_4*2H_2O$. As it was mentioned before, for VADO 28 we can see a weak peak at lower energies which was not present in XANES spectra of other filters. Also, the amount of sulphur in this filter is larger than in other two. This small peak at lower energies was attributed to organosulfur, i.e. dibenzothiophene which was retrieved from ESRF database[26]. The final fit of VADO 28 in ATHENA shows that besides dibenzothiophene, also $CaSO_4*2H_2O$ and $ZnSO_4*7H_2O$ are present (Figure 11). The presence of the latter will be shown again from the fit of Zn K-edge XANES spectra.

Sulphur compounds study with FDMNES

Sulphur is a heterovalent compound which forms chemical bonds with more electropositive and electronegative elements and has a range of oxidation states from 2- to 6+. The position of a white line of XANES spectrum is a fingerprint of a chemical state. The sulphur K-edge spectra are characterized by a prominent absorption edge feature, which stands for the transition of the S 1s core electron to the lowest unoccupied antibonding states on the S atom, and various post-edge features. The energy position of the edge feature of S K-edge XANES increases from 2469.5-2470 eV for transition-metal monosulphides (2-) to 2471 eV for disulphides of the pyrite group (1-), 2472 eV for native S (0), 2478 eV for sulphites and 2482 eV for sulphates [2].

Sulphates

The first coordination shell of sulphur in sulphates is composed of four oxygen atoms. The S-O distances span from 1.47 to 1.49 Å, and the O-S-O angle from 106.3° to 112.2° in different sulphate compounds. The sulphate ion $(SO_4)^{2-}$ has tetrahedral symmetry and all sulphate spectra are quite similar to each other with a distinct white line at ~2482 eV. The
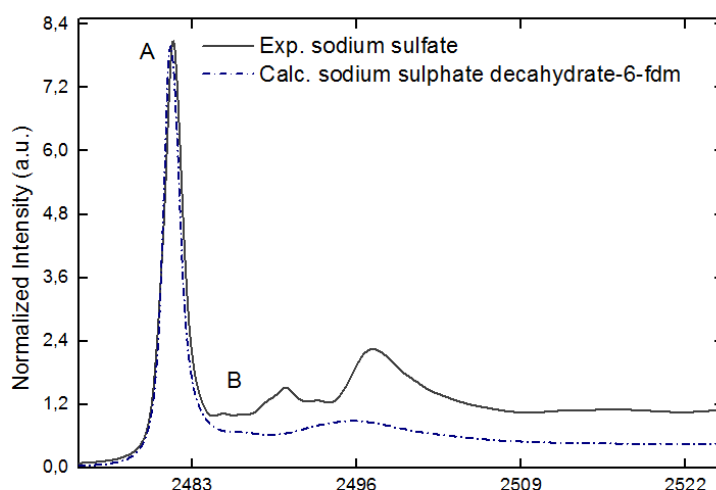
Figure 34 An experimental sodium sulphate spectrum along with calculated in FDMNES sodium sulphate decahydrate spectrum using FDM and cluster radius of 6Å

origin of the white line comes from the transition from S 1s core electron to the 3p like (σ* type) lowest unoccupied level [2, 28]. Various calculations done with sulphate compounds showed that the shape of the white line does not vary depending on the cation. In our case the reference experimental spectrum was that of sodium sulphate, therefore first the calculations for anhydrous sodium sulphate from different databases were performed. However, the best fit was obtained only when the XANES spectra of sodium sulphate decahydrate were calculated with larger cluster radii. Another important thing in calculations are the energy range and step which should resemble the ones of the experimental spectra. Unfortunately, all the calculations could reproduce only the white line correctly. The small shoulder just after the white line could be reproduced by calculations only when larger cluster radius of 6Å was included as shown on Figures 34 and 35. The DFT calculations done by Mori et al. reproduced all features in sodium sulphate spectrum when a large cluster radius of 7Å was chosen. They have also shown that main features could be reproduced even with the 1st coordination cell distances, i.e. in the absence of cations. However, the small shoulder could be calculated only when cation was included.
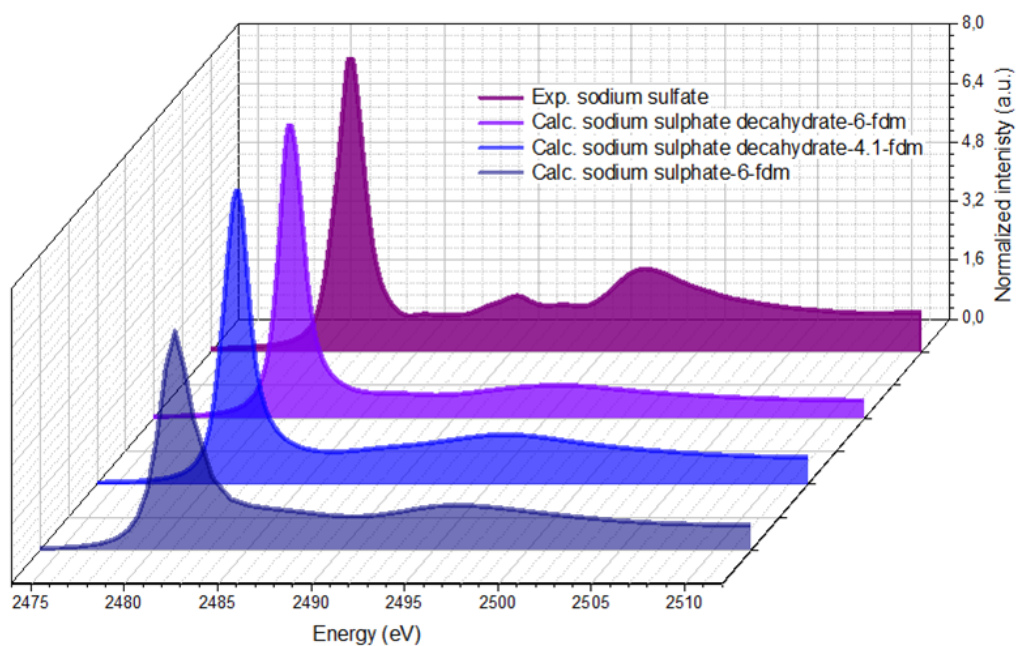
Figure 35 An experimental sodium sulphate spectrum (the last) along with calculated spectrum using FDM and cluster radius of 6Å (the first), spectra od sodium sulphate decahydrate using cluster radii of 4.1Å (the second) and 6Å (the third).

41

Sulphites

Sulphites have three pyramidal oxygen atoms in the sulphite ion $(SO_3)^{2-}$ forming a trigonal C_{3v} symmetry with a S-O interatomic distance of 1.505 Å and all O-S-O angles at 105.68°. The white line "I" in sulphites comes from S 1s—3p σ* transition and is found at ~2478 eV [2, 29]. The second small peak "II" in sulphite spectra was assigned as coming from transitions to empty molecular orbitals consisting of S 3s
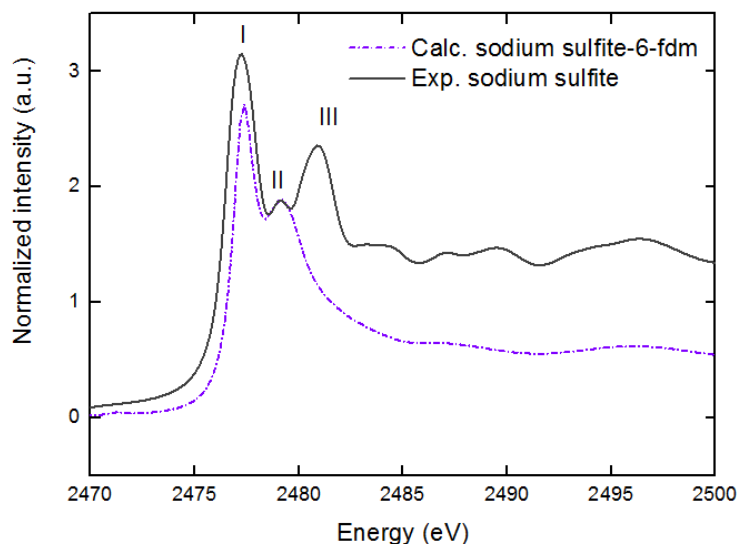
Figure 36 Experimental sodium sulphite spectrum along with calculated spectrum using FDM and cluster radius of 6Å

and 3p and some O 2p, which indicates the hybridization between the 3s and 3p atomic orbitals of the central sulphur ion (Figure 36). The hybridization is possible in C_{3v} symmetry, but forbidden in T_d symmetry. Therefore, this peak is an indication of local symmetry difference between sodium sulphite and sulphate. Mori et al. have proven this by the cluster calculation with 7 Å in which including the cations did not significantly change the overall spectral shape. FDMNES calculations

Figure 37 Sulfur K-edge XANES spectra of sulfate and sulfite forms of sulfur. The progressive shift of the absorption-edge is shown (adapted from Fleet et al.)[2]

with a cluster radius of 6 Å also succeeds in reproducing this peak. However, with a smaller cluster radius of 5 Å, the peak "II" is less evident (Figures 38). Peak "III" at ~2482 eV was not reproducible by calculations using FDMNES code, and we hypothesized that it might be due to an oxidation of S^{4+} to S^{6+}. In fact, this peak is missing in some experimental sodium sulphite spectra, as shown on the Figure 37 on the left from Fleet et al[2]. Mori et al. had faced the same problem and they initially suspected the contamination from the sulphate. However, additional XES measurements revealed the pure sulphite. Therefore, they concluded that this peak was due to band structure (i.e., long-range order) effects that were not accounted for in the computational model[28]. Sekiyama et al. explain this peak by the transition from S 1s to d-like a_1* orbital [29].

Figure 38 An experimental sodium sulphite spectrum (the last) along with calculated spectra using FDM and cluster radius of 5 Å (the first) and 6 Å (the second).

Sulphides

In contrast to sulphites and sulphates, where the first coordination shell is composed only of oxygen atoms, sulphides include the metal cation in the first coordination sphere of sulphur. The white line generally is found at ~2472 eV and many authors have suggested that it is due to orbital hybridization between the S 3p and the metal 3d orbitals can explain (Figure 39). In sulphides, the 3p shell is fully occupied, therefore an orbital hybridization with metal 3d orbitals in a partially filled d-shell will transfer some S

Figure 39 Database zinc sulphide spectrum along with calculated spectrum using FDM and cluster radius of 8.5 Å

3p electron density to the cation. This creates unoccupied states of S 3p character[2, 28].

The edge position does not only follow the screening effects but also depends on the energy of the cation 3d shell as well as the local symmetry, and thus the type of orbital hybridization. Mori et al. showed that spectral features in ZnS were not reproduced by using only first shell distances.

43

When larger cluster of 5.5 Å was included, it presented a better modelling of the overall experiment. As it is shown on Figure 40 below at 6.5 Å some spectral features are missing, and at 9.5 Å there are too many of them. For this particular case the cluster radius of 8.5 Å was the most suitable.
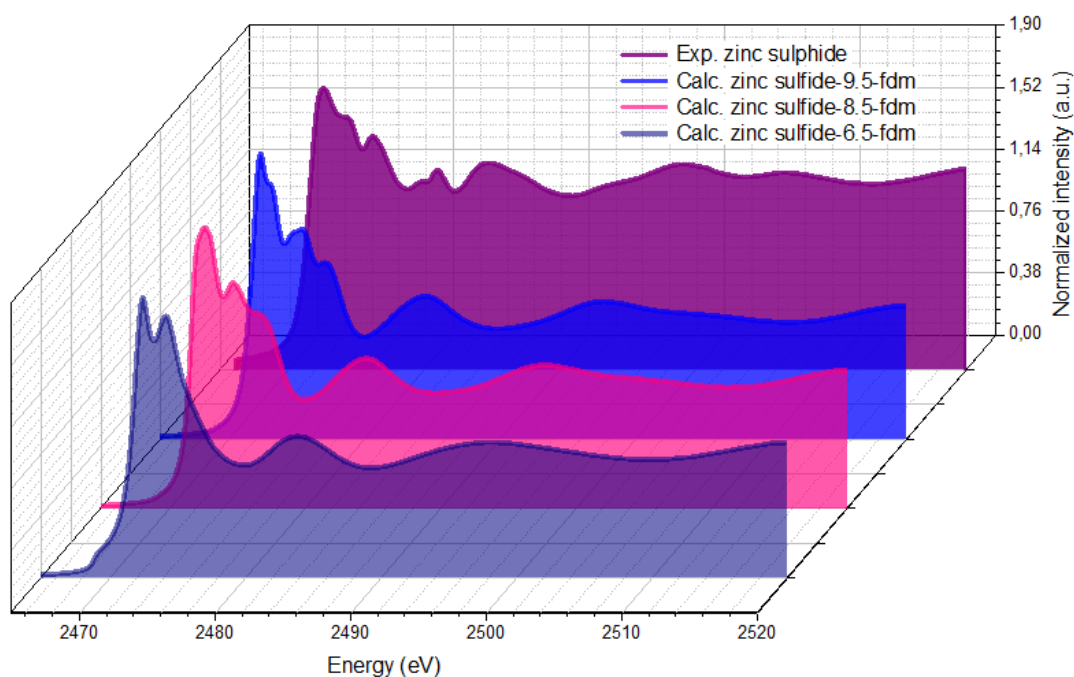
Figure 40 Database zinc sulphide spectrum (the last) along with calculated spectra using FDM and cluster radius of 6.5 Å (the first), 8.5 Å (the second) and 9.5 Å (the third).

Conclusion for FDMNES part

As it was proven by Joly et al, Xu et al. and confirmed in this work, the muffin-tin approximation is not adequate for computing XANES spectra in the low-intermediate edge energy ranges, since the resulting spectra fail to reproduce crucial spectral features. As non-muffin-tin FDM calculations take substantially longer times than muffin-tin MS ones, the multiple scattering method was used as a starting point. The FDM could reproduce well the white line in sulphates when large enough cluster radius was used. Other spectral features were not fully reproduced. In sulphites first two peaks and extended features were possible to calculate with a large cluster radius as well. The peak at 2482 eV was assigned as coming from sulphate contamination. In zinc sulphide the main and extended features were reproducible using only a very large cluster radius of 8.5 Å. Overall, FDMNES can be used for S K-edge spectra calculations, however using only non-MT finite difference method, large cluster radii and carefully chosen energy range and step. The FDMNES code is simple to use, but the FDM calculations are time consuming.

IV-1-2 Iron XANES

As it is shown of Figure 16, all Fe K-edge XANES spectra have similar shapes, with minor differences. In order to perform a linear combination fitting in Athena, several reference samples were collected at Elettra synchrotron facility: $FeSO_4*7H_2O$, $Fe(NO_3)_3*9H_2O$, Fe_2O_3, $[Fe(H_2O)_6](NH_4)(SO_4)_2*6H_2O$ and $Fe_2(SO_4)_3*5H_2O$. Additional XANES spectra of three different forms of an iron oxide were needed, therefore FDMNES calculations of hematite (α-Fe_2O_3), maghemite (γ-Fe_2O_3) and magnetite (Fe_3O_4) were performed. For hematite crystallographic data by Blacke et al., for maghemite by Shmakova et al. and for magnetite by Hamilton et al. were used, Mincryst cards № 1919, 5909 and 2702, respectively[24]. The results of the fits performed in ATHENA for QUI 156, VADO 118 and VADO 28 are presented in a Table 2 below.

Component	QUI 156	VADO 118	VADO 28
$FeSO_4*7H_2O$	28%	11%	16%
$Fe(NO_3)_3*9H_2O$	27%	34%	-
Fe_2O_3	23%	33%	13%
simulated magnetite	22%	22%	28%
$[Fe(H_2O)_6](NH_4)(SO_4)_2*6H_2O$	-	-	43%

Table 2 Linear combination fitting in ATHENA of QUI 156, VADO 118 and VADO 28 Fe K-edge XANES spectra

The results of these fits might seem odd at the first look, however all samples appear to contain iron salts in the hydrates' form and iron oxides. In order to establish if our recorded reference compounds were consistent with their crystallographic data (i.e. oxidation state and local geometry) and could be used to identify the oxidation state and local geometry of Fe in our samples, the pre-edge analysis of all of them was performed and the results shown in Figure 41 for Fe_2O_3 and Figures A16 and A17 in the Appendix.
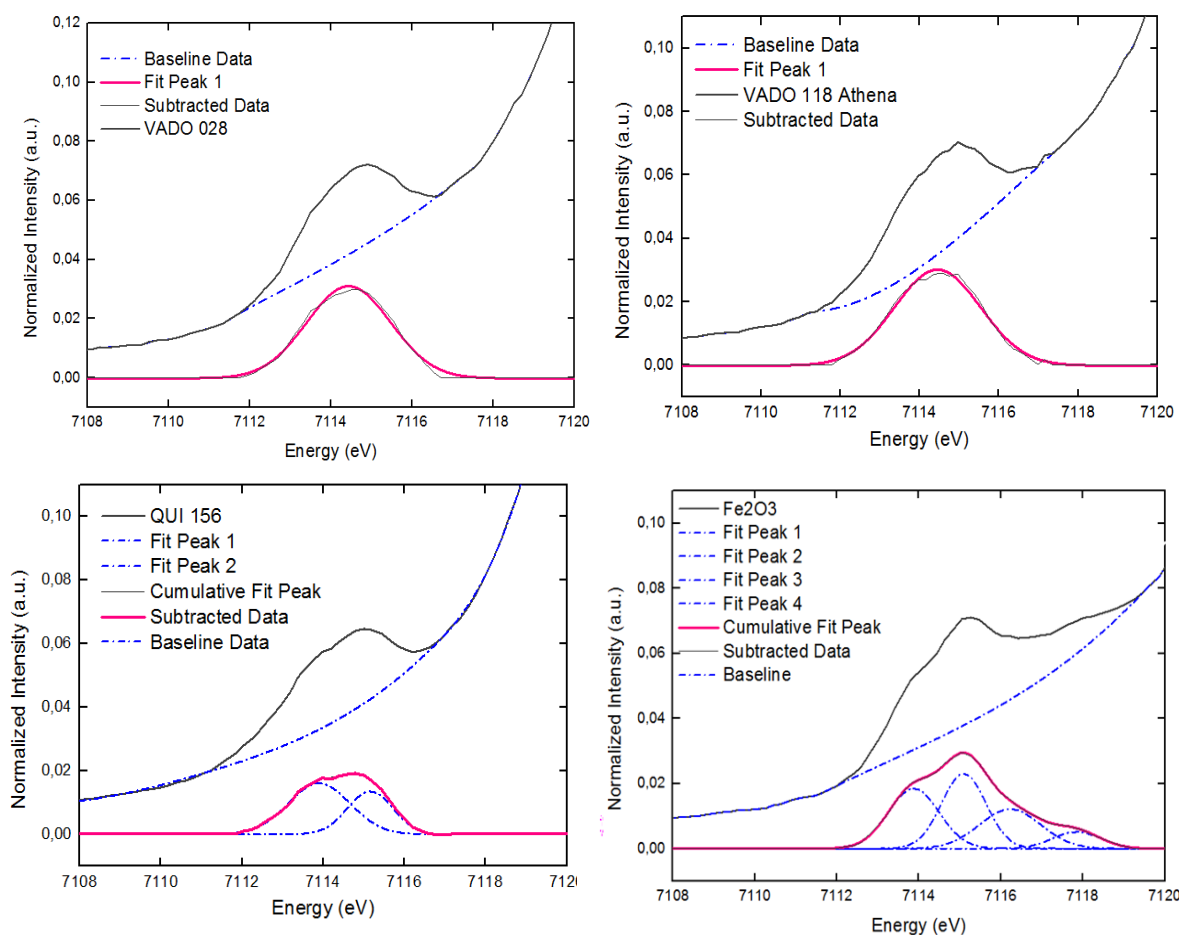
Figure 41 Selected normalized pre-edge region (Fe K-edge) and the best fit obtained (Origin) of VADO 28, VADO 118 (top), QUI 156 and Fe_2O_3 (bottom).

Identification of Fe oxidation state and local structure using pre-edge analysis have a lot of examples in the literature. Westre et al. describe thoroughly the pre-edge features of a number of ferrous and ferric compounds and give methodology for the interpretation of energy splitting and intensity distributions. They modelled pre-edge features by pseudo-Voigt line shapes (simple sums of Lorentzian and Gaussian functions), and functions modelling the background underneath the pre-edge features were chosen empirically [7]. Wilke et al. correlated the change of pre-edge features with oxidation state and local coordination environment of Fe atoms using various natural minerals. For all their fits they used pseudo-Voigt function with 50% of Gaussian and 50% of Lorentzian component [4]. In our case the fits were done using "Peak Analyzer" wizard of Origin Pro with Gaussian function as pseudo-Voigt function did not show good R^2.

High-spin ferrous octahedral FeSO$_4$*7H$_2$O

Among the collected reference spectra, we had one high-spin ferrous octahedral compound, FeSO$_4$*7H$_2$O. Westre et al. performed fittings of a number of ferrous compounds with an E$_0$=7111.2 eV, and in our case E$_0$ of 7112 eV was used. The comparison between pre-edge fittings performed by Westre et al. for octahedral high-spin Fe^{II} compound [Fe(H$_2$O)$_6$][SiF$_6$] and for our reference sample of FeSO$_4$*7H$_2$O is shown on Figure 42 on the right.

As they report, all high-spin ferrous compounds have two very weak pre-edge features split by ~2 eV, which is the case in our spectra as well (Figure 42). The 1s--3d transition is formally electric dipole forbidden, but gains intensity through the allowed electric quadrupole transition. Since both ferrous compounds have a nearly centrosymmetric octahedral iron site, electric dipole intensity cannot be gained by mixing of the 3d orbitals with the 4p orbitals.

In this work the fit was performed with three components, due to the shoulder in the first peak on the second derivative spectrum (Figure 42 C). In our case, the shoulder could not be distinguished from noise at the second derivative spectrum, most probably due to a different experimental resolution, therefore the fit with only two Gaussian components was done.
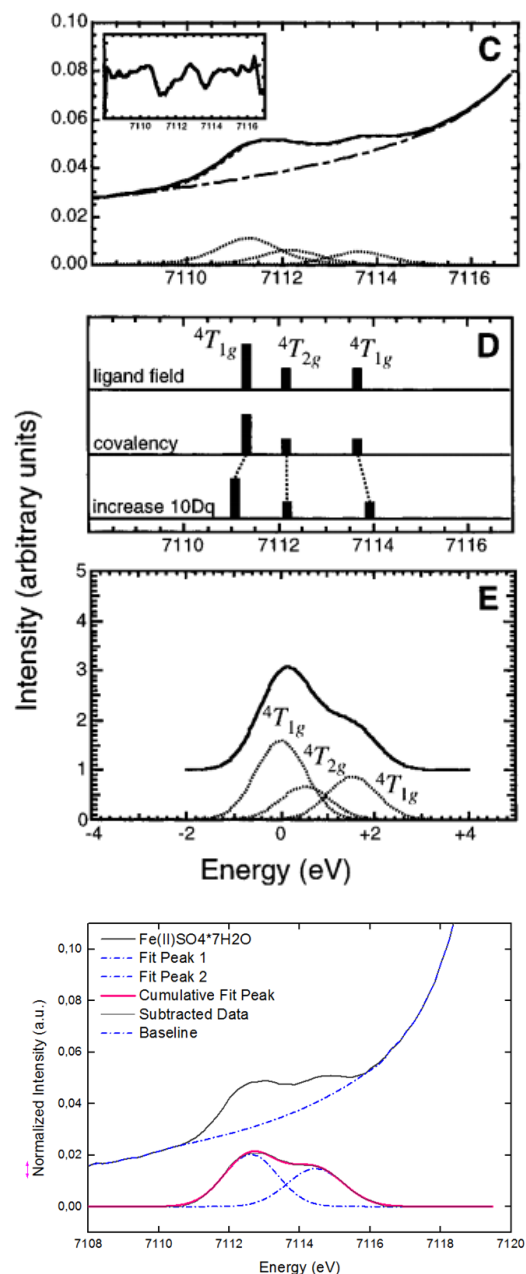
Figure 42 (top) (C) The Fe K-edge pre-edge region of [Fe(H$_2$O)$_6$][SiF$_6$] including the experimental data, a fit to the data (- - -), the background function (--), and the individual pre-edge peaks from the fit (°°°). The inset displays the second derivative of the data and the second derivative of the fit (- - -). (D) Ligand field analysis of [Fe(H2O)6][SiF6] (E) Theoretical simulation of the pre-edge region for [FeCl$_6$](adapted from Westre et al.)[7] (bottom) The pre-edge fit for FeSO$_4$*7H$_2$O

High-spin ferric octahedral compound

Westre et al. also discussed Fe K-edge XAS data measured for a series of high-spin ferric octahedral model complexes with varying ligation. Since these compounds have centrosymmetric octahedral site, the only intensity mechanism available for the 1s--3d feature is the allowed electric quadrupole transition. In the high-spin ferric d^5 case, the $^5A_{1g}$ ground state has a $(t_{2g})^3$-$(e_g)^2$ configuration. Promotion of a 1s electron into the 3d orbital produces two excited hole configurations, $(t_{2g})^2(e_g)^2$ and $(t_{2g})^3(e_g)^1$.

Fits performed showed that there are two pre-edge features with splittings ranging from 1.1 to 1.5 eV. The splitting of the two pre-edge features is related to ligand field strength, with the splittings following the trend Fe-O/Fe-N>FeF_3>$FeCl_3$>$FeBr_3$ [7]. In our case (Fe-O) the fit showed two peaks with a splitting of 1.4 eV, which is in a good agreement with the paper. The pre-edge fits of high spin ferric compounds $Fe(NO_3)_3*9H_2O$ and $Fe_2(SO_4)_3*5H_2O$ can be found in Appendix Figures A16 and A17.

The fit of another octahedral ferric compound, an iron oxide as shown on Figure 43 (bottom right) includes four peaks. Wilke et al. (E_0=7111.08 eV) report that in iron oxides and hydroxides from one to three other components are observed above 7115 eV. In the literature the appearance of these peaks is explained by the long-range order around iron atom, involving 3d orbitals of distant neighbours [30]. Therefore, these contributions were excluded in the centroid calculations by Wilke et al[4]. In our case the also first two components were included in centroid calculations as shown on Table 3 below.
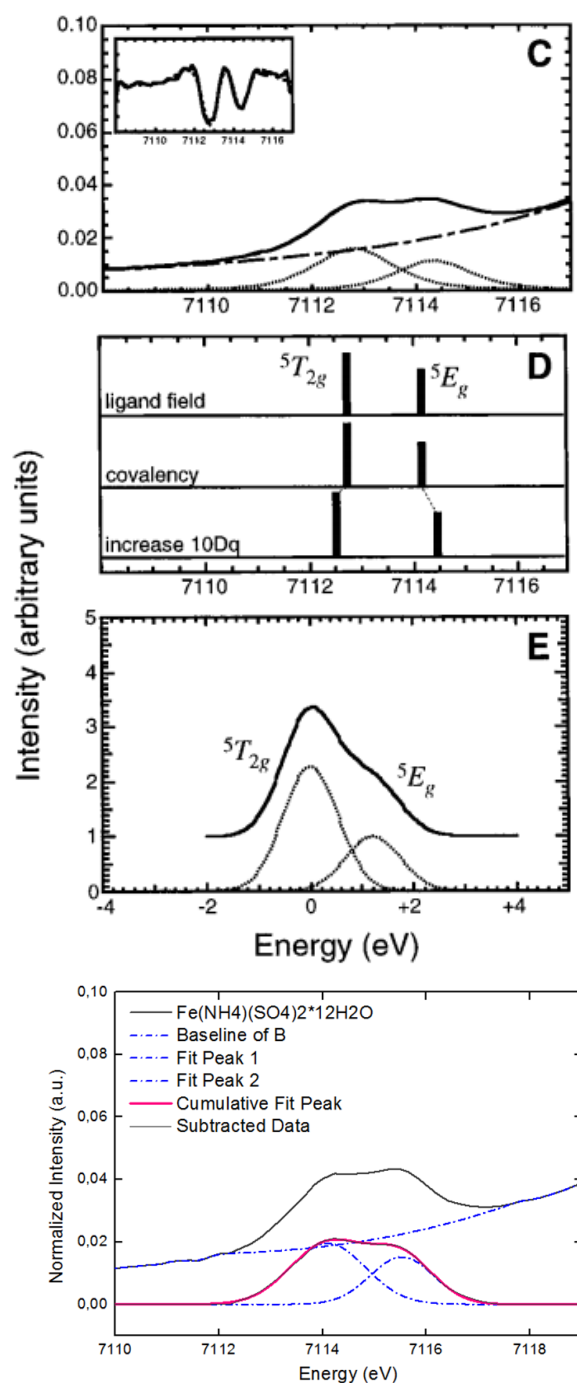
Figure 43 (top) (C) Fit to the Fe K-edge pre-edge region of Fe(acac)$_3$ including the experimental data (s), a fit to the data (- - -), the background function (- -), and the individual pre-edge peaks from the fit (°°°). The inset displays the second derivative of the data (- - -). (D) Systematic analysis of the octahedral pre-edge features. (E) Theoretical simulation of the pre-edge region for [FeCl$_6$]$^{3-}$](adapted from Westre et al.)[3] (bottom) The pre-edge fit for Fe(NH$_4$)(SO$_4$)$_2$*12H$_2$O done in Origin.

The fits of VADO 28 and VADO 118 filters show one component at 7114.43 eV and 7114.45 eV, respectively. The shape of pre-edge fits and the centroid positions allow to conclude that iron in these two filters is in a similar form. The pre-edge fit of QUI filter shows two components and a centroid at 7114.38 eV, revealing its difference from VADO filters.

The comparison of the fits performed in Origin with centroid values from Wilke et al. and Westre et al. show that our results are credible (Table 3). The difference between the authors' values and ours are justified when considering different E_0 values used for data treatment.

compound	oxid. state	symm.	ligation	component position	area	centroid	Wilke et al.[4]	Westre et al.[7]
$FeSO_4*7H_2O$	ferrous	Oh	6O	7112.61	0.0385	7113.41	7112.16	
				7114.45	0.0296			
Fe_2O_3	ferric	?	6O	7115.10	0.0311	7114.51	7113.47	
				7113.87	0.0285			
				7117.85	0.0074			
				7116.23	0.0226			
$[Fe(H_2O)_6](NH_4)$ $(SO_4)_2*6H_2O$	ferric	Oh	6O	7114.10	0.0354	7114.67		7113.14
				7115.53	0.0231			7114.57
$Fe(NO_3)_3*9H_2O$	ferric	Oh	6O	7114.05	0.0268	7114.80		
				7115.49	0.0291			
$Fe_2(SO_4)_3*5H_2O$	ferric	Oh	6O	7113.97	0.0173	7114.84	7113.61	
				7115.41	0.0269			
QUI 156				7113.89	0.0355	7114.38		
				7115.16	0.0189			
VADO118				7114.45		7114.45		
VADO 28				7114.43		7114.43		

Table 3 Pre-edge characteristics of reference iron compounds and filters and their comparison with literature values

Petit et al. and Wilke et al. made their own calibration curves using the data from a number of iron compounds[4, 31]. Wilke et al. had plotted the centroid positions of binary mixtures between $^{IV}Fe^{2+}$, $^{VI}Fe^{2+}$, $^{IV}Fe^{3+}$ and $^{VI}Fe^{3+}$ against their integrated pre-edge intensity as shown on Figure 44. As it is shown the octahedral complexes are lower in intensity than less symmetrical tetrahedral ones. Also, a clear separation between the centroid positions of Fe^{2+} and Fe^{3+} compounds is evident. Generally, the difference of 1.4 eV is reported between Fe^{2+} (~7112.1 eV) and Fe^{3+} (7113.5 eV) [4, 31]. At the end of the paper Wilke et al.
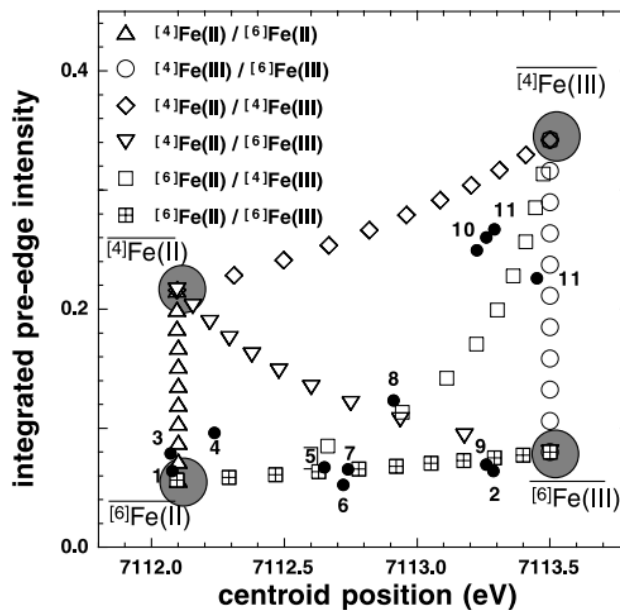
Figure 44 Summary of the pre-edge characteristics for the binary mixtures between $^{IV}Fe^{2+}$, $^{VI}Fe^{2+}$, $^{IV}Fe^{3+}$ (taken from Wilke et al.)[4]

describe a procedure for assigning the oxidation state and the geometry of unknown mixtures of iron compounds. However, they warn of the challenges of such way and the need of high S/N data.
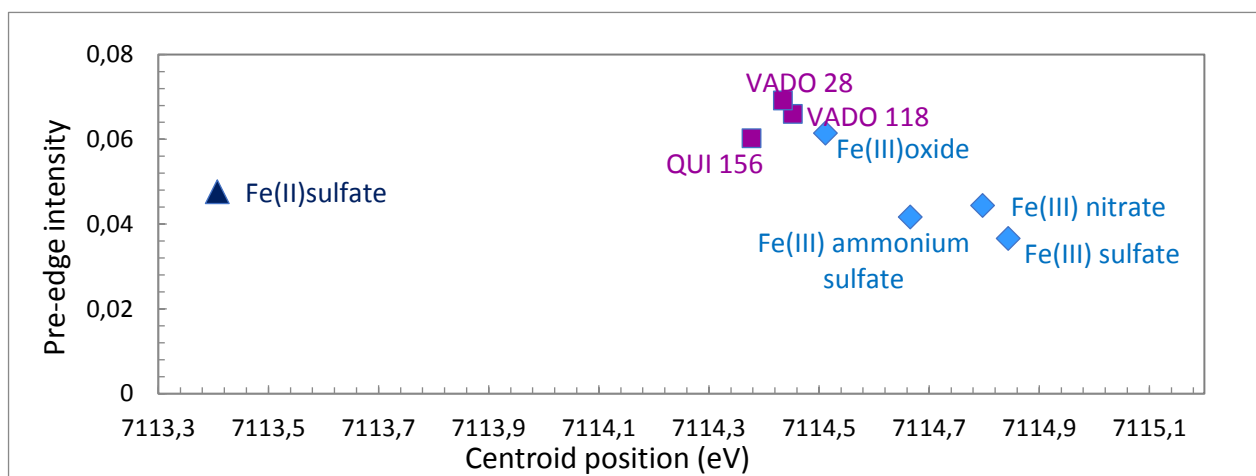
Figure 45 Summary of pre-edge region fittings showing the centroid positions vs pre-edge intensity

A summary of the pre-edge fits of our five reference samples are shown on Figure 45 below. Obviously, the number of reference compounds was not sufficient to build a full calibration curve in order to assign the oxidation state and the local geometry of our unknown iron samples. Nevertheless, we can see a clear separation between the centroid positions for our Fe^{2+} and Fe^{3+} compounds similar to literature values. The pre-edge intensity of our filters' and Fe_2O_3 are slightly higher than that of octahedral reference compounds, therefore most probably the symmetry is not

purely octahedral. Another thing to note is the centroid positions of our filters, which fall in between 2+ and 3+ oxidation states.

Iron chemical state XPS

Iron was the element of interest from the beginning of the XPS experiment, as the speciation of iron by means of only XAS technique was challenging. Therefore, the detailed spectra in the Fe 2p energy range were collected for all samples. As it is shown on Figure 53 (right) of the evolution of at.% in VADO 118 with sputtering time, the amount of iron on the surface before sputtering was close to zero. Nonetheless, after 30 min of sputtering of VADO 118 filter, Fe 2p signal became slightly more prominent. The data obtained was fit as demonstrated on Figure 32b The Fe 2p XPS spectra in general are known as difficult to analyse, especially because of a steeply rising background and broadened line width [32]. The detailed spectrum of VADO 28 new after 10 min of sputtering with 50 eV pass energy also exhibited similar line shapes. The fit was performed using two Fe 2p peaks centred at ~711 eV and at ~724 eV. McIntyre et al. who carried out a rigorous study of iron oxides compounds using an XPS experiment. According to the authors, these two peaks signify Fe $2p_{3/2}$ and Fe $2p_{1/2}$ of α-Fe_2O_3 and/or γ-Fe_2O_3. This conclusion is supported by the results of XANES linear combination fitting and GNXAS calculations of EXAFS region.

In the investigation of iron oxides they went further and studied the effect of sputtering on oxidation states of iron (III) oxides. It was revealed that after only few minutes of bombardment with argon ions, the Fe_2O_3 would reduce to FeO. The chemical shifts they assign for Fe 2p in FeO are centred at ~709.5 eV, which we did not see for VADO samples [33]. It could be explained by the fact that Fe in VADO samples was covered with a layer of carbon species, and sputtering duration was enough only to scratch it away.

Local structural environment of Fe: EXAFS analysis

XAS and XPS experiments provided some valuable information about iron speciation. However, the results were not sufficient to draw final conclusions. Therefore, EXAFS region analyses using GNXAS package was performed. As customary in any EXAFS analysis, the experimental signal is compared to a theoretical one, which is calculated from an initial structural model. In light of the experimental evidences mentioned above for the Fe case (pre-edge, XANES and XPS) the most suitable structural model could be an oxygen ligation for the first shell of Fe. Therefore, we have used the one by Maslen et al. of hematite[34]. In the model each Fe atom is surrounded by six O atoms. There are three at the corners of an equilateral triangle above the central Fe atom participating in an Fe-O bong length of about 2.11 Å. The remaining three form another equilateral triangle below the central Fe atom with a Fe-O interaction of 1.94 Å. As we will see this asymmetry

of the first shell coordination is not the case for the VADO filters, whereas more flexible first shell bond length distribution was obtained for the QUI case. There are several Fe -- Fe interactions, where the shortest one is visible on Figure 46 (right) along the face, shared between FeO6 coordination octahedra. Overall the unit cell of hematite is depicted on the Figure 46 (left) below. The structure is hexagonal, the space group R3c, with 6 units of formula per unit cell.
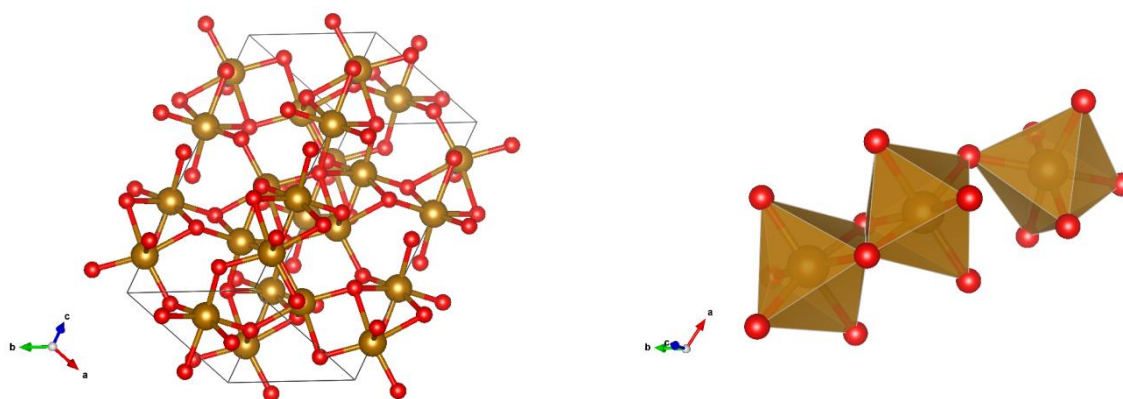
Figure 46. A unit cell of hematite (left). Fe atoms are diplayed in gold, O in red. A local fragment of the unit cell with local coordination (right). The picture displays both Fe-O and Fe -- Fe interactions.

The EXAFS analysis was performed using the GNXAS package which is based on Multiple Scattering (MS) theory. The method is based on the decomposition of the EXAFS signals into a sum of several contributions, the n-body terms. It allows the direct comparison of the raw experimental data with a model theoretical signal. The procedure avoids any filtering of the data and allows a statistical analysis of the results. The theoretical signal is calculated *ab-initio* and contains the relevant two-body $\Upsilon^{(2)}$, the three-body $\Upsilon^{(3)}$ and the four-body $\Upsilon^{(4)}$ multiple scattering (MS) terms. The two-body terms are associated with pairs of atoms, probing their distances and variances. The three-body terms are associated with triplets of atoms and probe angles, bond-bond, and bond-angle correlations. The four-body terms are associated with chains of 4 atoms, and probe distances and angles in between, and bond-bond, and bond-angle correlations. In this application, only the pair contribution $\Upsilon^{(2)}$ have been used in the fitting procedure, due to the light scattering of the first shell atoms, i.e. the oxygen, and the angles they form within their surrounding. As we will see this approach allows to simulate almost all the oscillatory portion of the EXAFS spectrum. Specifically, the two body signals included in the fitting procedures are: the two-atom contributions $\Upsilon^{(2)}$ Fe-O with degeneracy of 6 (first shell); the two-atom contributions $\Upsilon^{(2)}$ Fe--Fe with degeneracy of 3 (second shell); the two-atom contributions $\Upsilon^{(2)}$ Fe--Fe with degeneracy of 3 (third shell). Also, in VADO 28 case, an additional fourth shell due to the Fe- - Fe interaction with degeneracy of 3 has been included. In the case of QUI sample, several test have been done by considering an asymmetric distribution of the first shell[35-39].

Data analysis is performed by minimizing a χ^2-like residual function that compares the theoretical signal, $\mu(E)$, to the experimental one, $\mu_{exp}(E)$. The phase shifts for the photoabsorber and backscatterer atoms were calculated starting from the structural model of hematite taken from Maslen et al. [34]. They were calculated according to the muffin-tin approximation and allowing 10% overlap between the muffin-tin spheres (which was justified previously in MT approximation theory). The Hedin-Lundqvist complex potential was used for the exchange-correlation potential of the excited state. The core hole lifetime, Γ_c, was fixed to the tabulated value and was included in the phase shift calculation. The experimental resolution used in the fitting analysis was about 2-3 eV, in agreement with the stated value for the beam line used. The amplitude correction factor S_0^2 were identified to be 0.70(5) for the Fe K-edge for all samples.

By looking at the experimental signals diplayed in Figure 47, the relative FT's show most likely two main peaks, plus several less intense peaks. They are indicated as Fe-O and Fe—Fe on Figure 47. This holds true for all investigated filter samples but with different extent. The FT of the VADO118 samples shows the highest intense second peaks with respect to the other VADO sample (even though the K2 vs. K has an effect in the FT magnitude). The FT relative to the QUI sample is somewhat different to the other two.

Several tests were made in order to check the possible ligation of the Fe site. Indeed, the following results were obtained: i) the asymmetry of the FeO$_6$ octahedron, by considering 2+4 vs. 6 number of equivalent Fe-O distances; ii) the possible inclusion of a Fe—S interaction. This test failed for all three measurements; iii) the Fe-Fe interaction of the outer shell, which only in some cases were observed. The best fit have been obtained by using only two-body terms. This leads to a simplification of the possibile multiple scattering path which is normally mandatory for a straigthforward interpretation of an EXAFS signal. In our case, though, we decide to make the intertretation easier. This is corroborated by the magnitude of the observed FT peaks and by the obtained data. Figure 47 displays the best fits EXAFS for the three samples whereas the Table 4 reports the structural and non structural parameters as obtained by the fitting procedures.

Figures A18 and A19 in Appendix shows the details of the EXAFS analysis, for all filters. This kind of plot permits to identify the most contributing individual signals to the theoretical one. All the signals in both figures indicated that all signals are rather important in the determining the total theoretical one. Also, the Fe—Fe interactions modulates all the EXAFS by giving a peculiar high frequency contribution which is not negligible.

Figure A20 from Appendix displays some examples of the two-dimensional section of the parameter space (contour plots) for some studied samples, which have been used to calculate the

error in the parameter determination. These plots were selected among the parameters having strong correlation to reflect the highest error. The inner elliptical contour corresponds to the 95% confidence level. It is important to emphasize that this evaluation provides only statistical errors on EXAFS refined parameters and it does not account for systematic errors in the theory or peculiar to the experimental technique.

	VADO028 (v0c)	VADO118 (v1c)	QUI156 (qsc)
Fe-O / Å CN = 6	1.995(6)	1.992(7)	
σ^2 Fe-O / Å^2	0.012(2)	0.010(2)	
Fe-O / Å CN = 2			1.767(5)
σ^2 Fe-O / Å^2			0.020(4)
Fe-O / Å CN = 4			2.002(4)
σ^2 Fe-O / Å^2			0.005(1)
Fe- Fe / Å CN = 3	3.02(1)	3.05(1)	
σ^2 Fe--Fe / Å^2	0.012(2)	0.011(2)	
Fe--Fe / Å CN = 3	3.39(3)	3.38(2)	
σ^2 Fe-Fe / Å^2	0.024(5)	0.008(4)	
Fe--Fe / Å CN = 4	3.93(6)		3.78(4)
σ^2 Fe-Fe / Å^2	0.03(1)		0.003(2)
E_0 Fe	7124.7(4)	7124.7(5)	7120.7(2)
S_0^2 Fe	0.70(5)	0.70(5)	0.70(5)
χ^2-like residual / (10^{-6})	10.4	5.84	6.78

Table 4 Structural parameters from EXAFS fitting results of filter samples. The estimated parameter errors are indicated in parentheses

Generally, we can see that the theoretical signal matches well with the experimental ones in all panels, indicating that the strategy was the suitable one. Certainly, some peaks were not fitted at all, but they belong to outer shell, i.e. above 4Å, and this is out of the aim of the present application. Table 4 shows that the local atomic structures of the two VADO samples match well with the hypothetical model that has been used in the calculation, even though the asymmetry of the model is no longer present here. Indeed, Fe is surrounded by six oxygens, at about 1.99 Å composing a FeO_6 figure in the first shell. This is not the case for the QUI sample where an asymmetric first shell (two shorter Fe-O distances at 1.77 Å and 4 longest distances at 2.00 Å) produce the best fit. The second shell of the VADO samples is confirmed to be Fe at around 3.05 Å and 3.39 Å. Eventually those results not only confirm the ligation suggested by the pre-edge data analysis, i.e.:

the FeO_6 figure, but also allowed to determine of the Fe-O bond length. Also, the obtained values for the EXAFS Debye-Waller factor in the first shells suggests the occurrence of a significant structural disorder around the Fe atomic site. This is also seen from the higher values of the pre-edge intensity depicted on Figure 45.

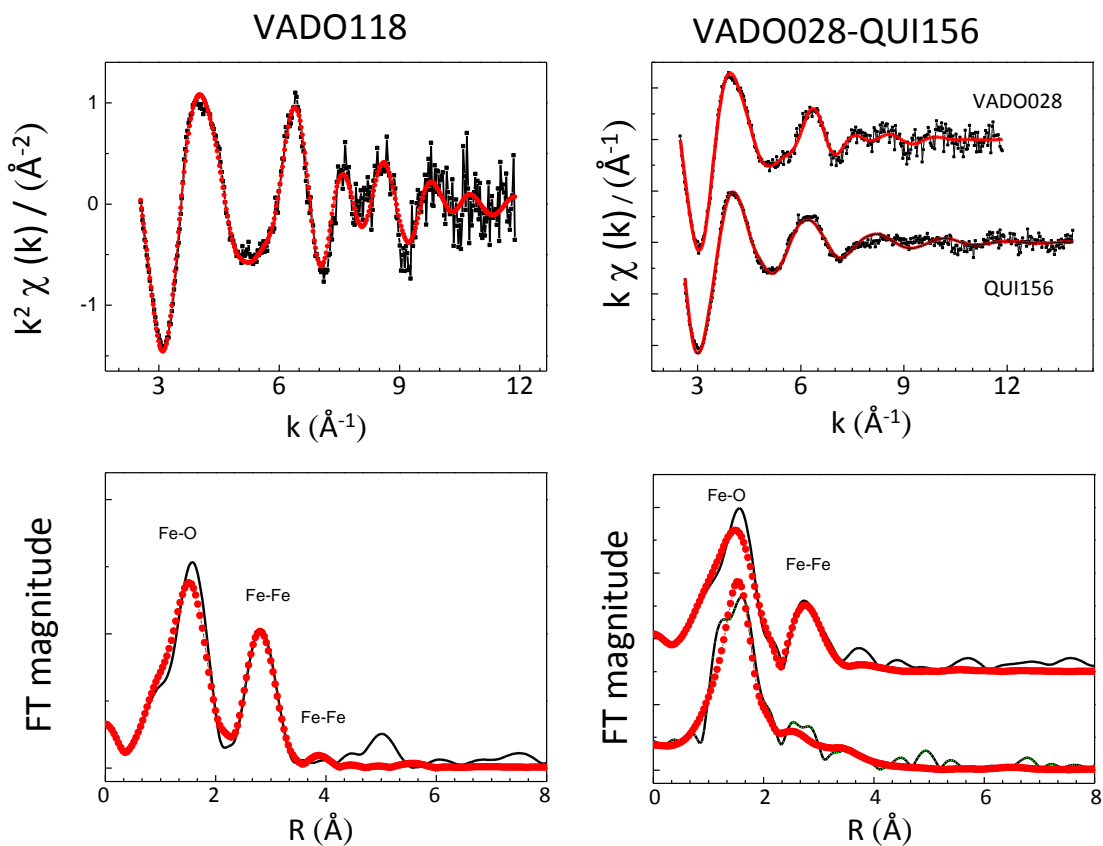Figure 47. Comparison of the experimental (-) and theoretical (…) k_n-weighted EXAFS signals (upper panels) and the corresponding Fourier Transform (FT) of the k_n-weighted EXAFS for filter samples at the Fe K-edge. The different level of S/N reflect the relative abundance of the Fe in the filters. Because of the higher concentration, the EXAFS analysis of the VADO118 sample has been computed in K2.

IV-1-3 Calcium XANES

Ca K-edge spectrum for all filters had good S/N ratio. Two reference compounds' spectra were collected at Elettra synchrotron: $CaSO_4*2H_2O$ and $CaCO_3$. The linear combination fitting was performed in ATHENA and as shown on Figure 15 in VADO 118 filter calcium is predominantly in $CaSO_4*2H_2O$ form with minor amount of $CaCO_3$. For QUI 156 and VADO 28 the fits are not perfect, but both of the filters contain different ratios of calcium sulphate and calcium carbonate as demonstrated on Figures in Appendix A7 and A8, respectively.

Calcium chemical state XPS

As mentioned earlier in the XPS experimental section, the Ca 2p signal in VADO 118 became apparent only after 30 min of sputtering and S/N was still low as shown on Figure 33a. The Ca 2p signal for both filters was fit with one doublet centred at ~347.5 eV, which was assigned to calcium sulphate signal [40]. Moreover, the O 1s spectra for VADO 118 show presence of sulphur oxides and linear combination fitting of XANES data showed calcium sulphate as the main component as mentioned in the paragraph above. The $CaSO_4$ is generally formed in the atmosphere when $CaCO_3$ reacts with H_2SO_4 produced by the photo-oxidation of the SO_2 emitted during the burning of fossil fuels [41].

The absence of sulphur signals can be explained by small XPS cross-section values for sulphur and the fact that non-organic sulphur is generally found in the bulk of the filter.

For VADO 28 "new" (Figure 33b) the Ca 2p signal was fitted for two compounds, calcium carbonate at ~347 eV and one for calcium sulphate at ~347.8 eV[41]. The carbonate signal is present in C 1s and O 1s spectra of VADO 28 "new" [40, 42]. Furthermore, the linear combination fitting of XANES spectra of VADO 28 reveals that both calcium sulphate and calcium carbonate are present as mentioned earlier.

Titanium K absorption edge spectrum represents the limitation of XAFS, as it was shown before on Figure 23, its EXAFS region overlaps with Ba L$_{III}$ edge. In order to identify the chemical state of Ti in QUI 156 and VADO 28 filters, the pre-edge analyses were performed. Ti compounds were studied extensively through the analysis of their pre-edge features[43-45]. The pre-edge of QUI 156 spectra showed clearly three peaks A1, A2 and A3. Fitting of QUI 156 with the Lorentzian functions gave three components at: 4968.5, 4971.1, 4974.1 eV as can be seen on Figure 48 (top). VADO 28 was fit with pseudo-Voigt function, as the fit with Lorentzian functions was not satisfactory (Figure 48, bottom). The positions of these peaks and their relative intensities allowed to conclude that in our filters Ti exists as TiO_2 rutile, with Ti(IV) having a six-fold octahedral coordination number. The

Figure 48 Selected normalized pre-edge region (Ti K-edge) and the best fit obtained(Origin) of QUI 156 (top) and VADO 28 (bottom)

origins of these pre-edge peaks were assigned as coming from transitions to the mixed Ti p-d orbital. The first and second components were interpreted as coming from dipolar transitions from Ti 1s to t_{2g} and e_g levels, and the third to 4p levels[43, 44].
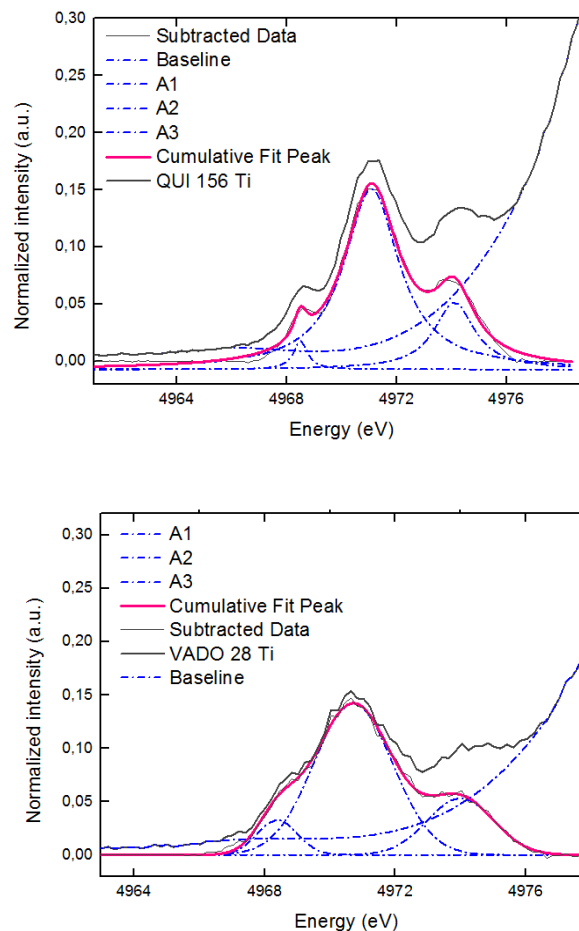
Farges et al. have studied rigorously FEFF calculations of Ti compounds varying different parameters such as cluster radius. They have demonstrated that 59 atoms, i.e. 5.5 Å cluster radius is sufficient to reproduce well XANES and EXAFS regions accurately with all features B-E3 (Figure 24). The pre-edge features were not reproduced, and as authors explain, full MS calculations are needed with radius cluster of 15Å[43].

In this work an attempt was made to reproduce the calculations using the *ab initio* approach of FDMNES code. Green's function formalism method was used with a cluster radius of 5, 5.5 and 6Å and crystallographic structure information of Howard et al. [46]. As it is shown on Figure 24 the three pre-edge peaks were not reproduced correctly by FDMNES calculations. The C2-C3 and E1-E3 features are well reproduced even for 5Å calculations. They are not clear on QUI 156

spectra as the S/N is very low, but all the spectra were compared with Farges et al. The D feature appears only at 6Å cluster radius calculations. The B shoulder which was reproduced well by Farges et al. in our case is shifted to lower energy in all cases. In general, FDMNES calculations with MT potential reproduced well the rutile TiO2 features except the pre-edge region where it requires full MS calculations.

IV-1-5 Vanadium

First thing to note on the vanadium K-edge spectra of VADO filters, besides overlapping Ba L_{III}-edge, are the distinct pre-edge peaks. The XANES spectrum of V K-edge is very sensitive to the local symmetry of the around the vanadium. The pre-edge peak is present in all vanadium spectra which originates from formally

Figure 49 Derivative plots of the K-edge spectra of vanadium

forbidden 1s-3d electronic transition. This transition is allowed when there is a distortion of local symmetry, which in turn leads to p-d orbitals mixing[47, 48]. The intensity and energy position of the pre-edge peaks allows to obtain structural and chemical information of vanadium compounds. An extensive study of various vanadium compounds with a wide range of oxidation states (-1..+5) and coordination geometries (octahedral, tetrahedral, square pyramid, trigonal bipyramidal,
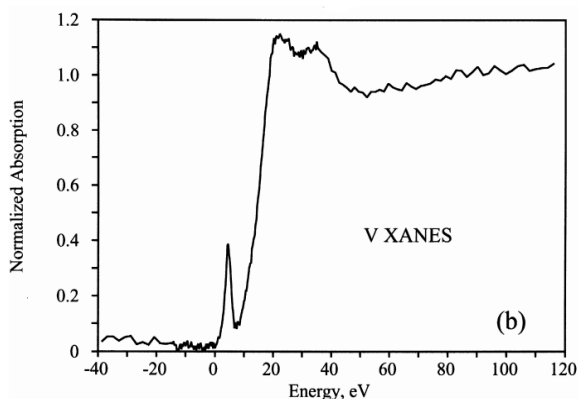

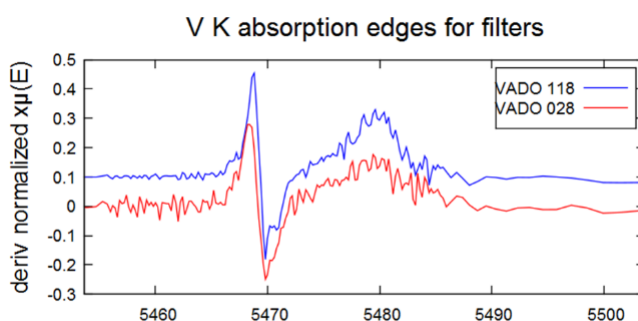Figure 50 Vanadium XANES spectrum of the NIST urban PM SRM.[6]

dodecahedral) was done by Wong et al. [49] However, in order to use that study as a reference high-resolution spectra with high S/N are necessary. In all our filters the amount of vanadium was rather low, so the some spectral features are indistinguishable from the noise. Nonetheless, the normalized intenisty of the pre-edge peak and the derivative plots of the K-edge spectra(Figure 49) of vanadium allow us to say that it is V_2O_5 or V_2O_4 present in our filters. The pre-edge peak fitting of VADO filters' spectra

was attempted as in the study by Chaurand et al. [50] According to the authors for V^{4+} standard compounds, two components are required to model pre-edge peaks, with centroid positions depending on local symmetry of V. For V^{5+}standard compounds, all spectra must be fitted with three components. The pre-edge fit of VADO filters performed in Origin was not satisfactory. The

NIST paper by Huggings et al. demonstrates a very similar spectrum for urban PM SRM to our VADO filters (Figure 50). According to the authors the vanadium in their PM exists as V_2O_4 deduced by comparison with Wong et al. Their arguments say that a pre-edge feature at 4.4 eV is reasonably sharp and symmetric, therefore it suggests a single oxidation state for vanadium. The peak position and intensity allowed them to identify a tetravalent vanadium coordinated by oxygen anions [6].

IV-1-6 Chromium

Chromium, which is found in natural environments in two oxidation states 3+ and 6+, is an unusual element. In Cr(VI) form it is highly soluble and toxic to living organisms, and in Cr(III) form it is relatively insoluble and an essential micronutrient[51]. Therefore, assigning correctly the oxidation state of Cr in a particulate matter is essential. Chromium K-edge spectrum of QUI 156 has low S/N ratio therefore the speciation is rather approximate. The starting point in the assignment was visual inspection of the spectra in order to calculate XANES spectra of reference compounds. Various calculations with the cluster radius of 6Å and Green formalism method were performed and a linear combination fitting with three relevant compounds of QUI 156 filter is shown on Figure 20. To calculate XANES spectra of eskolaite (Cr_2O_3) crystallographic data by Belokoneva et al. from Mincryst database, card №8455, was chosen. For spinel Fe_2CrO_4 paper by Smyth et al., Mincryst database, card №890 was used [24]. The last component, basic chromium sulfate $Cr(OH)SO_4*H_2O$ was calculated based on the paper by Riou et al. [52]. As it can be noted the spectrum of QUI 156 is too noisy to obtain a reliable fit. Nonetheless, the rough proportions vary as 45% for $Cr(OH)SO_4*H_2O$, 20% for Cr_2O_3 and 35% for Fe_2CrO_4. We can deduce that most chromium is in oxidation state 3+ in QUI 156 filter, which is the case in the NIST paper by Huggings et al. [6]. Another confirmation of a correct assignment of Cr oxidation state is the pre-edge region: it is dramatically different for Cr(III) and Cr(VI) species. When there is Cr(VI) present, it gives a very intense pre-edge peak due to a 3d-4p mixing in the four-coordinate transition metal ions, such as Ti^{4+} and V^{5+} also mentioned in this work [51]. Our findings suggest most likely the presence of of Cr(III).

IV-1-7 Manganese

Mn K-edge spectrum for QUI 156 and VADO 118 have an acceptable S/N ratio, but not for VADO 118. Due to the absence of reference spectra, calculations with FDMNES software were performed using the cluster radius of 6Å and Green formalism method. Comparison of spectral features of our filters and the paper by Ressler et al. lead to the idea of $MnSO_4$ and $Mn_5(PO_4)_2[PO_3(OH)]_2*4H_2O$ as possible components [53]. The XANES spectrum of ilesite ($MnSO_4*4H_2O$) was calculated using crystallographic data by Baur et al. from Mincryst database,

card №2123. For hureaulite $Mn_5(PO_4)_2[PO_3(OH)]_2*(PO_4)_2$ paper by Moore et al., Mincryst database, card №2051 was used [24]. The fits are not perfect, nonetheless a conclusion can be made that Mn is predominantly in oxidation state 2+ in all filters as shown on Figure 19 for VADO 28, and Figures A11 and A12 in Appendix for QUI 156 and VADO 118.

IV-1-8 Copper

Copper K-edge spectrum of QUI 156 has a low S/N, therefore the speciation of Cu is approximate. The visual comparison of XANES K-edge spectra of various copper compounds allowed to conclude that copper species in QUI 156 filter are similar to copper sulphate. The FDMNES calculations for chalcanthite ($CuSO_4*5H_2O$) were performed using Green formalism on muffin-tin potential with cluster radius of 6Å and are based on the paper by Bacon et al. from Mincryst database, card №827[24]. As it is shown on Figure 21 the overall shape of XANES and EXAFS regions were well reproduced, except for the pre-edge region. Comparison with NIST paper by Huggings et al. confirms the assignment of six-fold coordinated Cu^{2+} surrounded by oxygen anions. [6]

IV-1-9 Zinc

Zn K-edge spectrum for QUI 156 and VADO 118 have similar spectral features and an acceptable S/N ratio. Three reference compounds' spectra were collected at Elettra synchrotron: $ZnSO_4*7H_2O$, $ZnCO_3$ and $Zn(NO_3)_2*6H_2O$. The linear combination fitting was performed in Athena and for QUI 156 the best fit was obtained with approximately 82% of $ZnSO_4*7H_2O$ and 18% of $ZnCO_3$ as shown on Figure 13. For VADO 118 a good fit was not obtained, it is clear though that the main component is $ZnSO_4*7H_2O$ as shown in Appendix Figure A6. Results from NIST paper by Huggings et al. also include zinc in six-fold coordination by oxygen anions as the main form of Zn species in both urban and diesel PM [6].

IV-1-10 Nickel

In order to identify the speciation of nickel in VADO 118 filter various calculations using FDMNES code were performed. The visual comparison with the Ni K-edge spectra allowed to choose two Ni species as possible components[54]. First, trevorite ($NiFe_2O_4$) calculations were performed using Green formalism on muffin-tin potential with cluster radius of 6Å and based on the paper by Hill et al. from Mincryst database, card №4840. Another nickel compound, retgersite ($NiSO_4*6H_2O$) was calculated also with cluster radius of 6Å using Green formalism method, Mincryst database, card №7055[24]. According to LCF in Athena our nickel spectra consists from ~40% of $NiSO_4*6H_2O$ and ~60% of $NiFe_2O_4$ (Figure 25). The LCF fit does not match fully the experimental spectrum, however we can say that Ni in our sample is most probably in oxidation state 2+.

IV-1-11 Carbon

Most samples that have been exposed to the atmosphere generally have so-called "adventitious carbon" contamination. C 1s spectrum for contamination typically has C-C, C-O-C and O-C=O components. These chemical states of carbon are present in all filters: signal at ~285 eV stands for C-C signal of an aliphatic carbon, which was used for calibration of binding energy scale. The signal at ~286 eV is an indication of the C-O functional group, implying the presence of alcohols, ethers, and carboxylic acids and the one at ~288.5 eV is associated with O-C=O of carboxylic carbon [55-57]. In general, the adventitious carbon can be removed by argon sputtering, which is demonstrated on VADO 118 spectra after 2, 10 and 30 min of sputtering on Figures A13 a, b and c in the Appendix.

An additional peak that is present in all filters at ~282 eV signifies metal carbides[41, 42]. The most intense peak at ~293 eV in QUI 156 filter, shown on Figure 27a, comes from the C-F bonds of the PTFE filter together with F 1s signal at ~690 eV mentioned earlier [57]. The signal at ~290 eV in VADO 28 new filter on Figure 27c was assigned to a metal carbonate, presumably calcium carbonate. The region between 288-290 eV generally stands for metal carbonates, however it overlaps with carboxylic carbon signals at ~288.5 eV. The detailed assignment of carbon peaks presented here is only a scientific guess, which however it is comparable to the literature.

IV-1-12 Oxygen
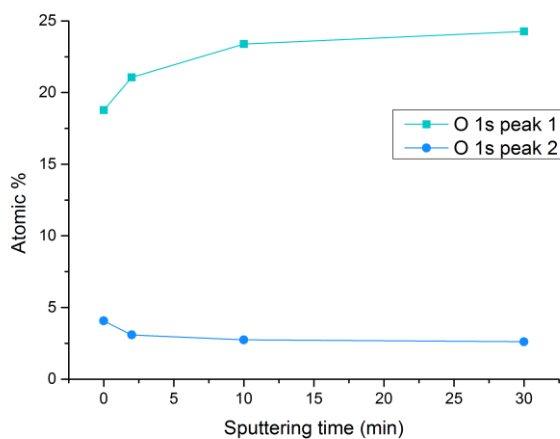

Figure 51 O 1s evolution of components 1 (top) and 2 (bottom) in VADO 118

The VADO 28 new spectrum of O 1s on Figure 51 shows broad signals ranging from ~538 to 528 eV. This indicates the coexistence of different oxygen chemical environments on the surface which overlap with each other[57]. The O 1s spectra from all filters reveal two components as shown in Figure 28 for VADO 28 "new" and Appendix Figures A14a-e. The peak at ~530 eV was assigned to the oxygen from metal oxides and metal carbonates. The large peak at ~533 eV was identified as an overlap of O 1s signals coming from silicon, sulphur, nitrogen oxides [56]. Additionally, the organic C-O signals cover the region from 531.5-532 eV, and organic C=O can be found at ~533 eV[58].

As sputtering of VADO 118 proceeded the two components of O 1s peak were changing in opposite way as shown on Figure 51. The at.% of the large peak 1 (at the top) centred at ~533 eV belonging to Si, N, S oxides rises, while the peak 2 (bottom) at ~530 eV decreases slightly. The rise of at.% of peak 1 is consistent with the "uncovering" of filter surface with sputtering as was shown on Figure 53.

IV-1-13 Nitrogen

The detailed N 1s spectra of all filters show two overlapping asymmetric peaks at ~399 eV and ~402 eV as shown on Figures 30 a, b and c. The peak 1 at ~399 eV has higher intensity then peak 2 at ~402 eV for all VADO 118 spectra. It was assigned to pyrrolic and amide nitrogen forms (Appendix Figures A15a-c). The component 2 at ~402 eV was attributed to a quaternary nitrogen[42, 55, 59]. In QUI 156 N 1s spectrum quaternary nitrogen is the dominating peak, with a small

Figure 52 The evolution of N 1s components 1 and 2 with sputtering time of VADO 118 filter

pyrrolic/amide signal (Figures 30c). In VADO 28 new spectrum an additional peak can be seen at ~407 eV which signifies the nitrate chemical shift [55, 59]. This peak is consistent with O 1s spectra assignment done previously.

The at.% of pyrrolic and amide component of the fit grow as the sputtering time increases in VADO 118 filter as shown on Figure 52. After 10 min and 30 min of sputtering of VADO 118 filter the at.% does not change significantly. The similar trend is observed for the 2nd component of the fit, just with decrease of quaternary nitrogen. After 10 min of sputtering, further bombardment with argon ions does not affect the at.% of both peaks. This can be interpreted as ammonia, which was on the surface, is getting removed by argon ions, allowing to unleash the pyrrolic and amide nitrogen forms.

IV-1-14 Sodium

All Na 1s filters spectra (Figure 31 example of VADO 118) were fitted with a single peak centred at ~1072 eV which identifies as sodium cation, most probably coming from sodium chloride, i.e. sea salt [42].

The Si 2p spectra in all VADO filters revealed the peak at ~103 eV, shown on Figure 29 from the fit of VADO 28 "new" which indicates silicon dioxide coming from the filter material quartz [57, 60]. The QUI 156 survey spectrum did not show any presence of Si, which allows to say that the only source of Si is quartz.

IV-2 In depth profile: XPS sputtering experiment in the case of VADO 118 filter

XPS analysis allows to quantify the elements present in the first few nm of analysed particles surface. However, sputtering with Ar^+ ions can give a depth profile information on samples. The atomic percentage (at.%) was obtained for VADO 118 filter to observe the change of relative amounts of elements with sputtering time as demonstrated on Figure 53 for O, Si, C, Fe, N and Na. Ca peak became noticeable only after 30 min of sputtering, therefore it was not included in overall quantification.
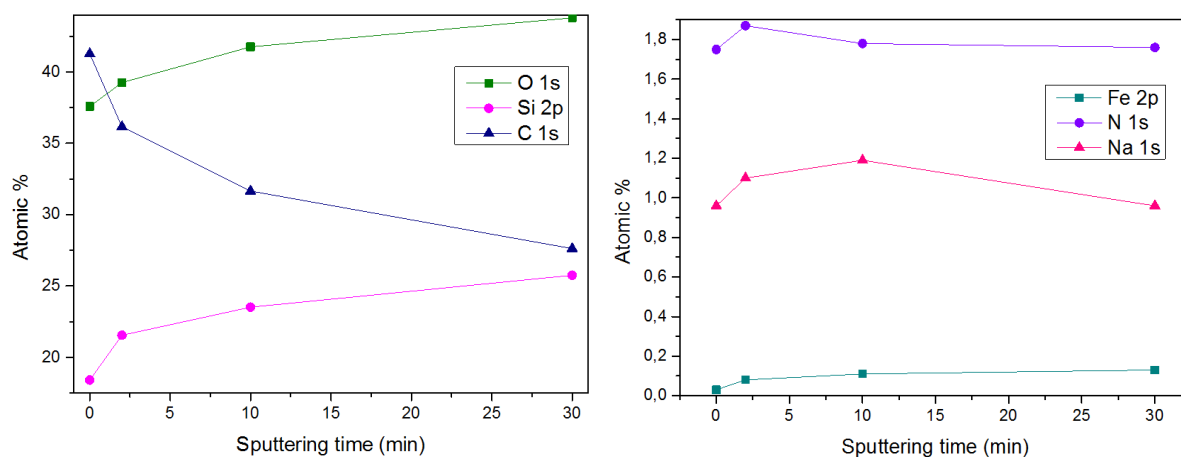
Figure 53 The evolution of O, Si, C (left) and of Fe, N, Na (right) at.% with sputtering time in VADO 118

As it can be seen there is a similar trend in at.% increase of Si 2p and O 1s with sputtering time and quite a dramatic decrease of C 1s signal from 41 to 27%. Fe 2p signal was not present at the detailed scan of iron compounds' energy range before sputtering. After 10 min of sputtering the hint of the signal appeared, however it did not increase throughout sputtering experiments. For Na we see slight rise in at.%, but after 30 min of sputtering the amount comes back to the original. This could indicate that sodium scattered all over the filter in different layers. The N 1s signal stays steady except the small increase after the first sputtering. This might be due to ammonia, which was uncovered after 2 min of sputtering and was ejected by argon ions. These trends allow to say that probably carbon was at the surface, covering other elements. As sputtering proceeded, it had removed some surface carbon, allowing Fe, N, Na and the filter material quartz (Si and O) to be closer to the surface. In general, we can only make assumptions about the nature of processes that happened during sputtering.
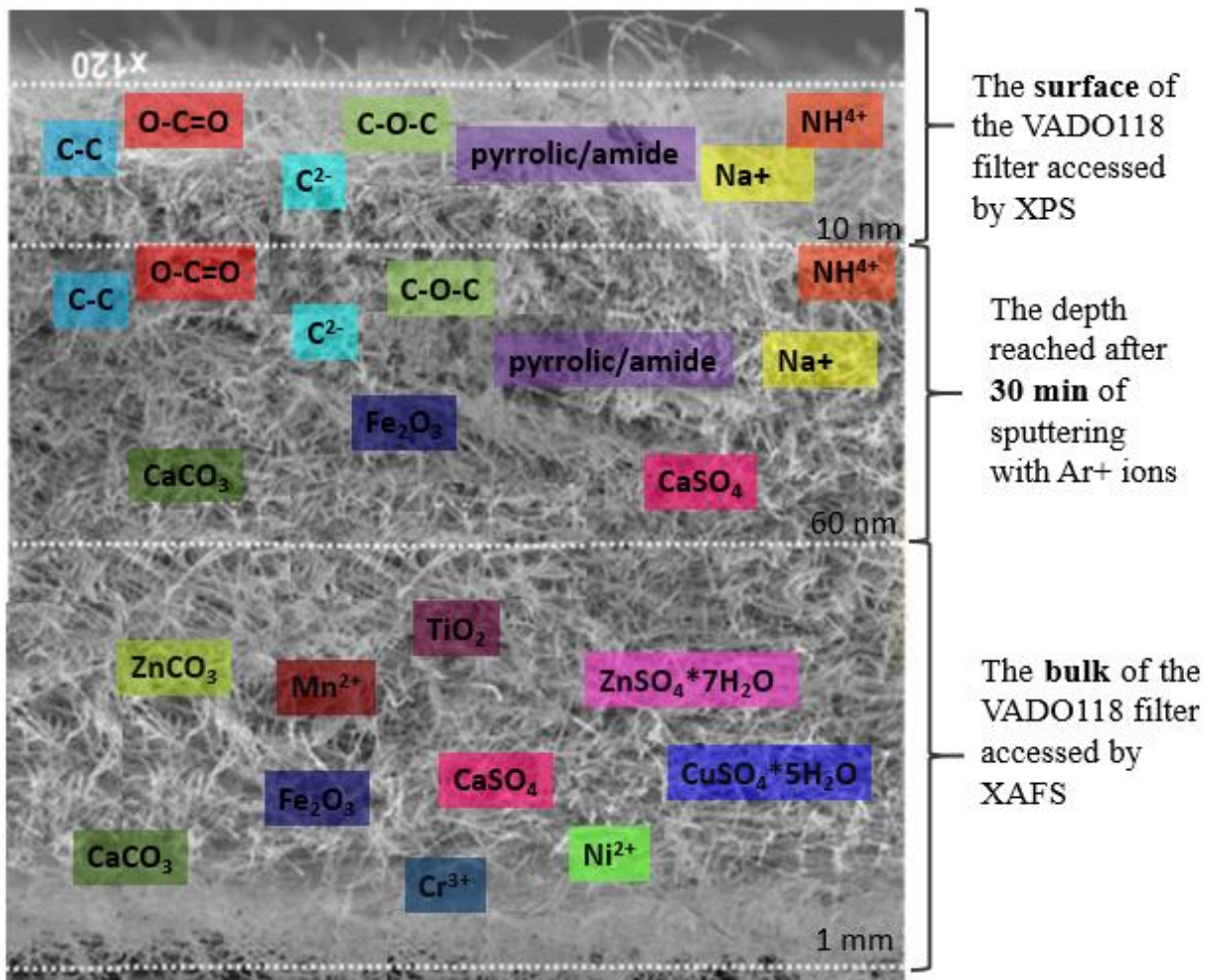
Figure 54 An approximate sketch showing the layers in VADO118 filter.

To sum up the information about from XPS sputtering and XAS experiments, a sketch of VADO 118 filter was produced. The background of the picture is the SEM image of a quartz filter magnified 120 times[61]. The top surface layer (up to 10 nm) before sputtering shows the presence of mostly adventitious carbon, carbide, some nitrogen forms, trace amount of Na+. The middle layer represents the composition of the filter that was probed after 30 min of sputtering with Ar ions. Adventitious carbon, carbide, pyrrolic/amide, ammonia, Na+(more) are still present. Also, at this depth (roughly 60 nm) we start seeing a signal for an iron oxide and calcium sulphate/carbonate. The last layer represents the bulk of the filter, where the results were taken from XAFS data analysis. We can see the presence of zinc sulphate/carbonate, copper sulphate, titanium dioxide, Cr(III), Mn(II), Ni (II). SiO_2 is not represented on the picture, as it is the filter material itself in the form of fibers.

CONCLUSIONS

In this master thesis the peculiar characteristics of core level spectroscopic techniques have been utilized to have a clearer picture on the chemical description of particulate matter samples. Not only chemical state of the various elements present in the filters have been probed, but also the local geometric structure and chemical bonding centred around single atomic sites. Two techniques that are based on the creation of a core-hole, namely, the X-ray Absorption Spectroscopy (XAS) and X-ray Photoelectron Spectroscopy (XPS), have been used in combination to theoretical calculation of XAS K-edges for various elements. Indeed, owing to the capabilities of FDMNES software to perform calculations for metal edges fast and due to a simple input procedure, the chemical speciation of all recorded XAS data was performed, even though we planned to do the speciation of a few selected elements only.

Data analysis included both the pre-edge portion of the XAS spectrum and the Linear Combination Fitting (LCF) of the XANES spectra, which provided valuable information about the oxidation states and local geometry of transition metal compounds. Metal speciation in some relevant cases were done by analysing the photo-electron kinetic energy emitted by the samples.

In the case of an iron metal, all previously listed approaches were not sufficient to make final conclusions about the coordination number and oxidation state. Therefore, its local structure has been unravelled by using the data from an EXAFS region.

At the end, we can have an information about the chemical speciation of elements in the bulk of the filter, as well as on the surface. In the case of VADO 118 filter we could even demonstrate the chemical composition of successive layers.

To conclude, this master thesis brought to a further level conventional analysis of a particulate matter by employing the potentials of core-level spectroscopies and theoretical calculations.

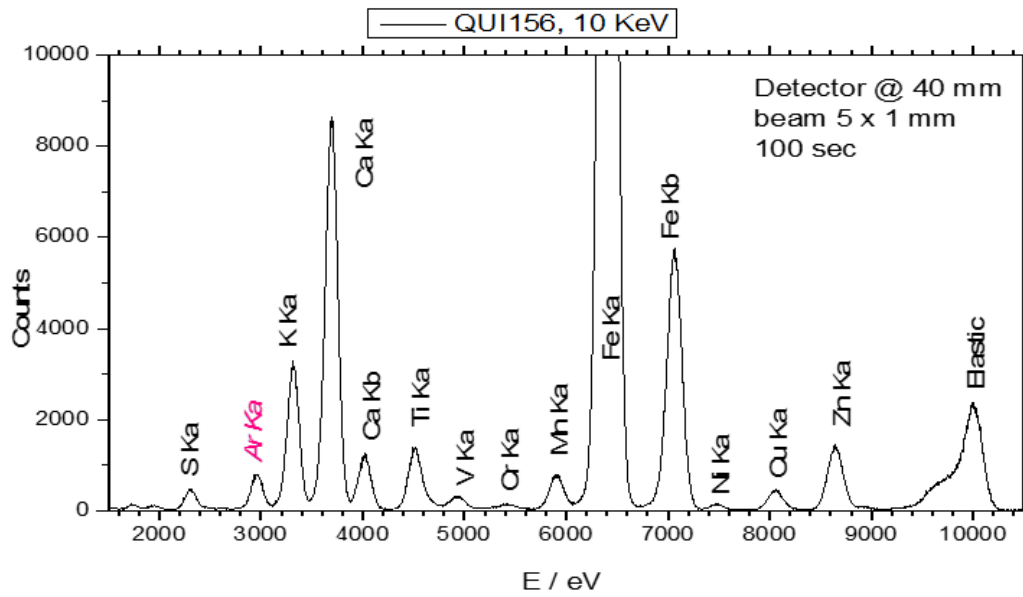Figure A1 Fluorescence response of QUI 156 filter

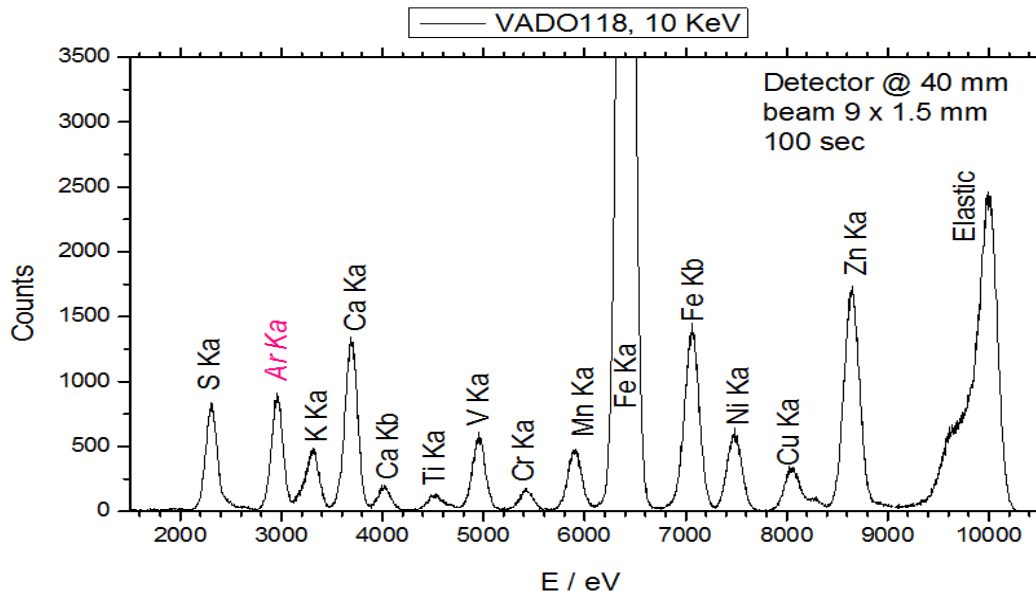Figure A2 Fluorescence response of VADO 118 filter

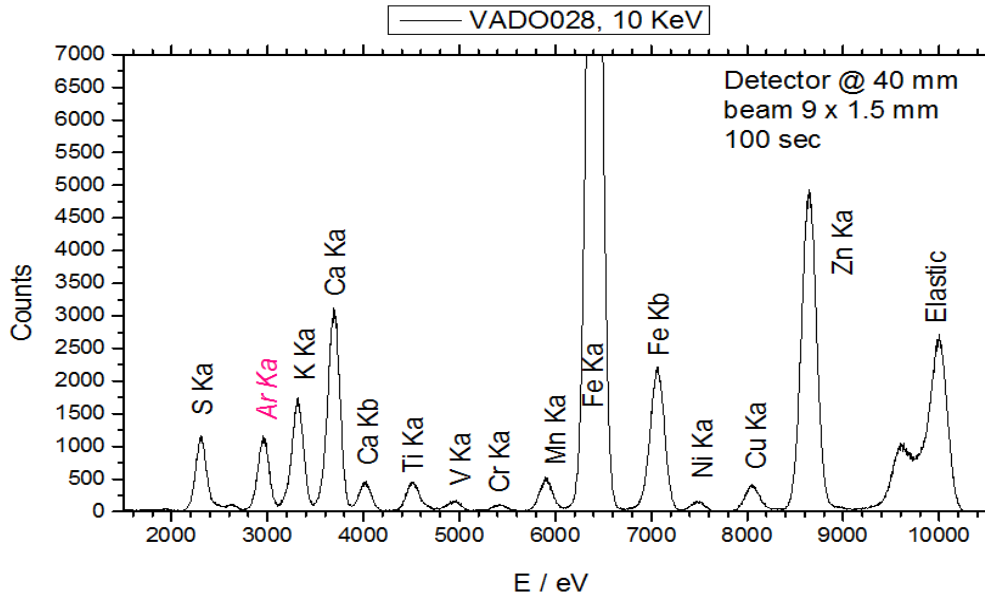Figure A3 Fluorescence response of VADO 28 filter

Figure A4 Results of linear combination fitting in ATHENA of QUI 156 S K-edge XANES spectrum
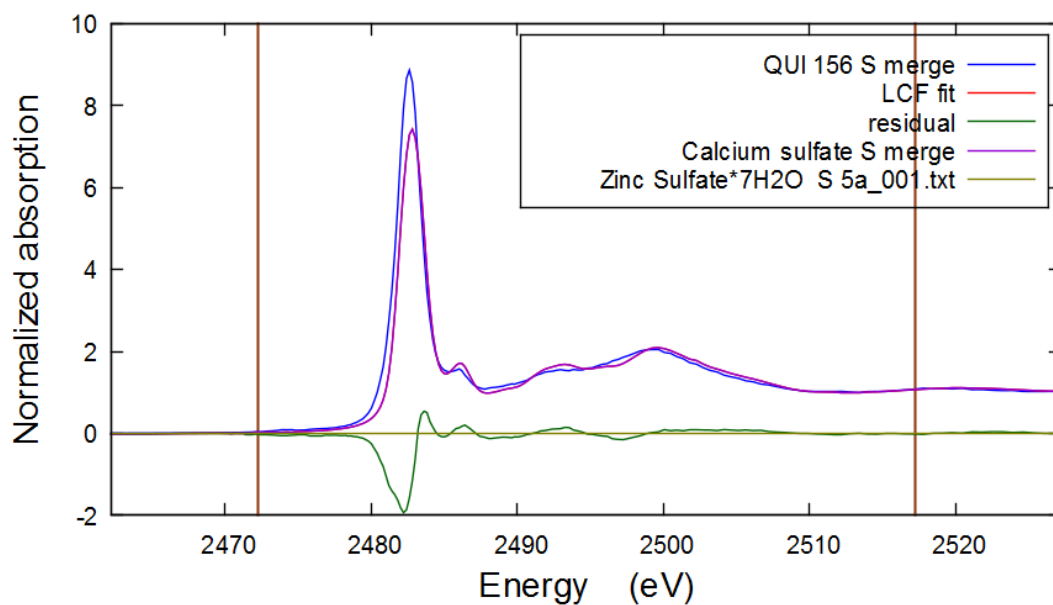

Figure A5 Results of linear combination fitting in ATHENA of VADO 118 S K-edge XANES spectrum
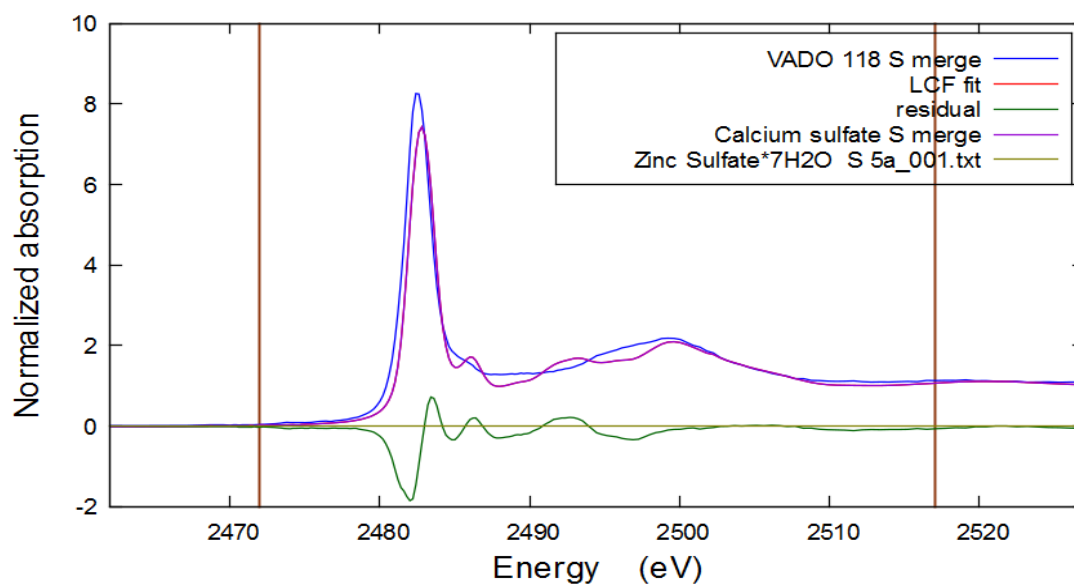
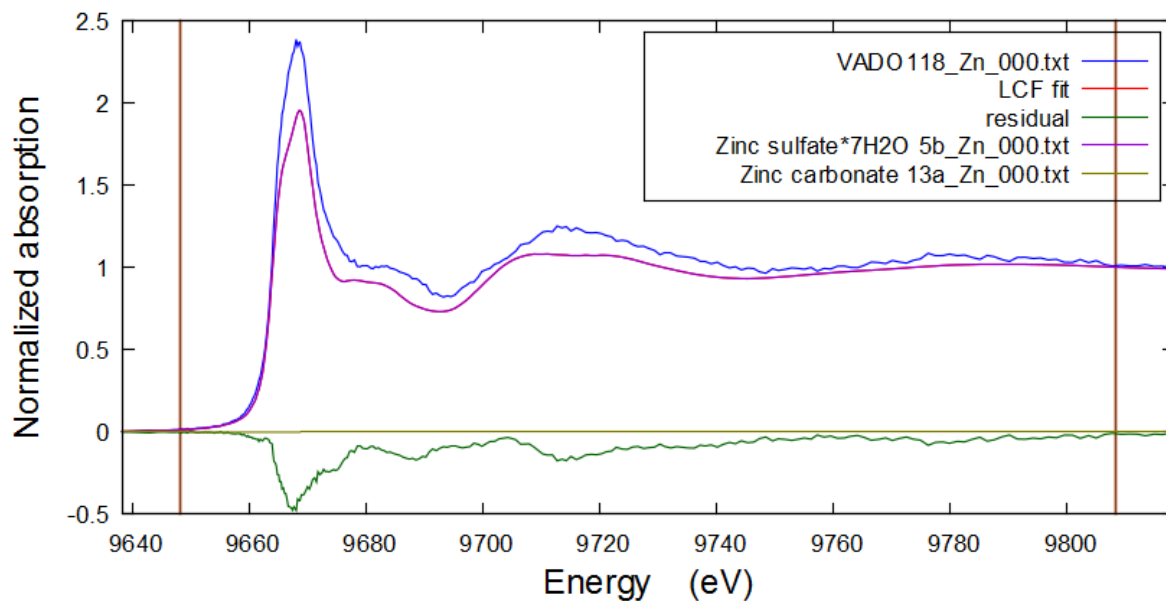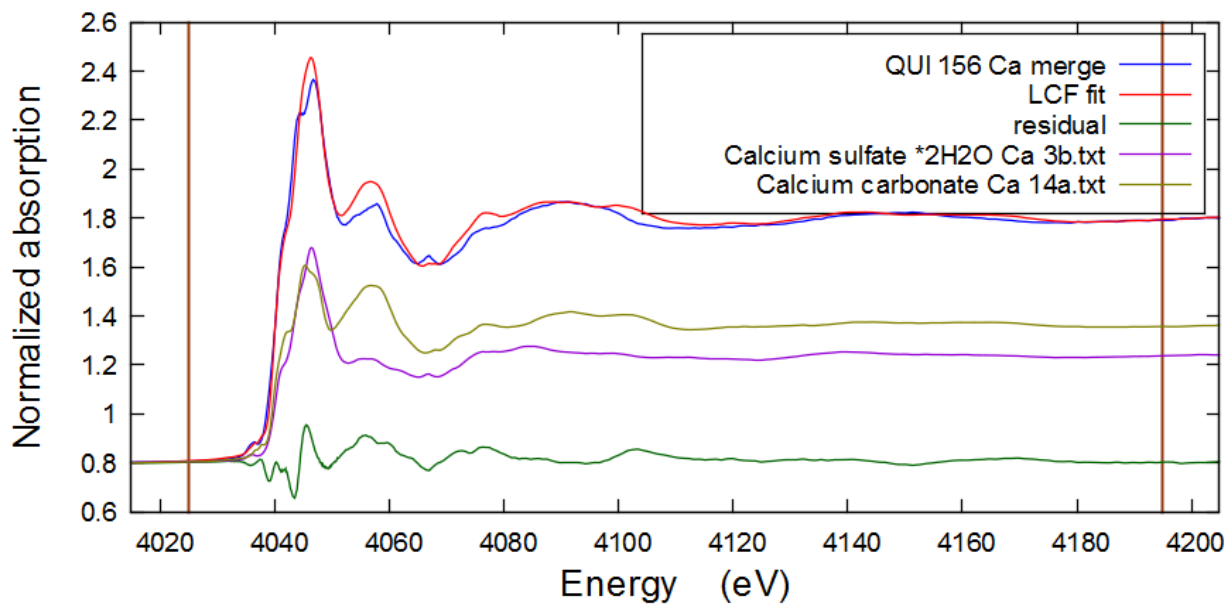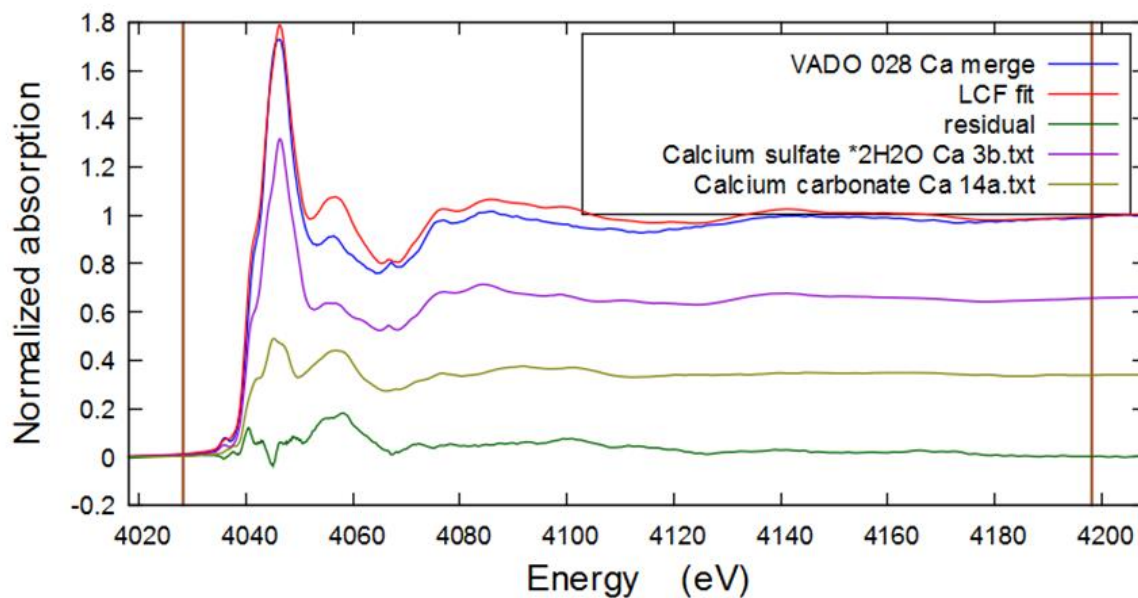Figure A6 Results of linear combination fitting in ATHENA of VADO 118 Zn K-edge XANES spectrum
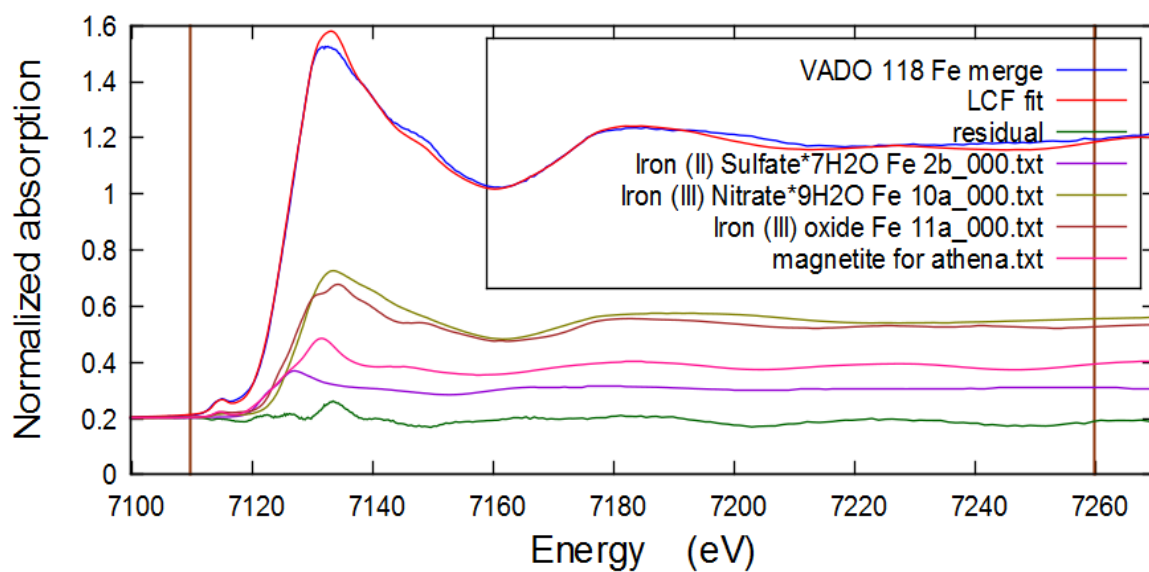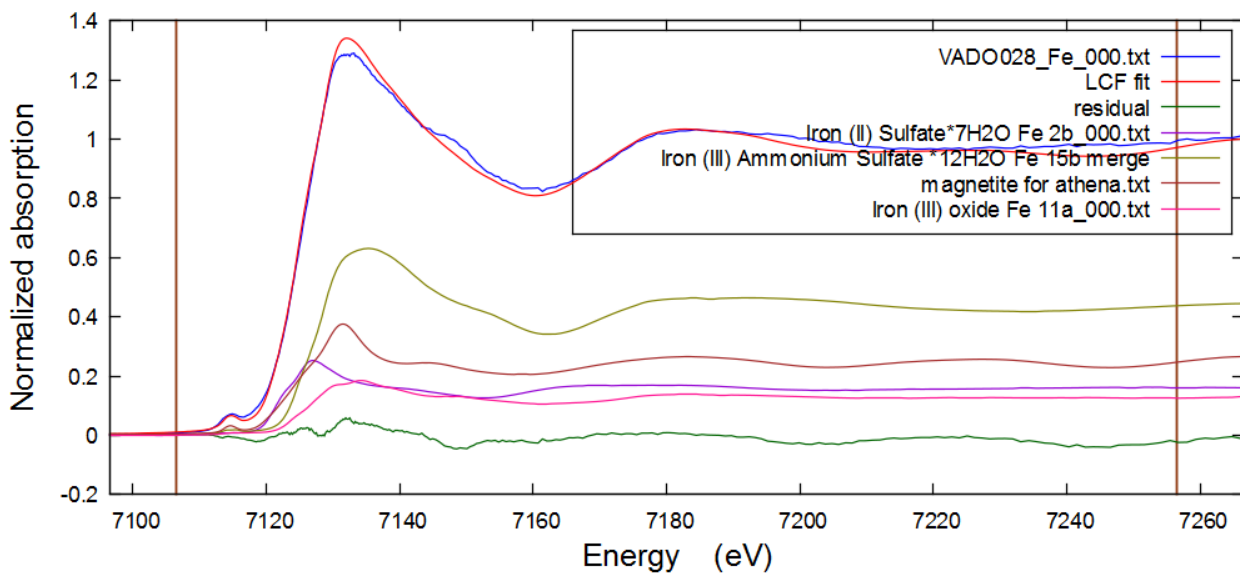

Figure A7 Results of linear combination fitting in ATHENA of QUI 156 Ca K-edge XANES spectrum

Figure A8 Results of linear combination fitting in ATHENA of VADO 28 Ca K-edge XANES spectrum

Figure A9 Results of linear combination fitting in ATHENA of VADO 118 Fe K-edge XANES spectrum

Figure A10 Results of linear combination fitting in ATHENA of VADO 28 Fe K-edge XANES spectrum

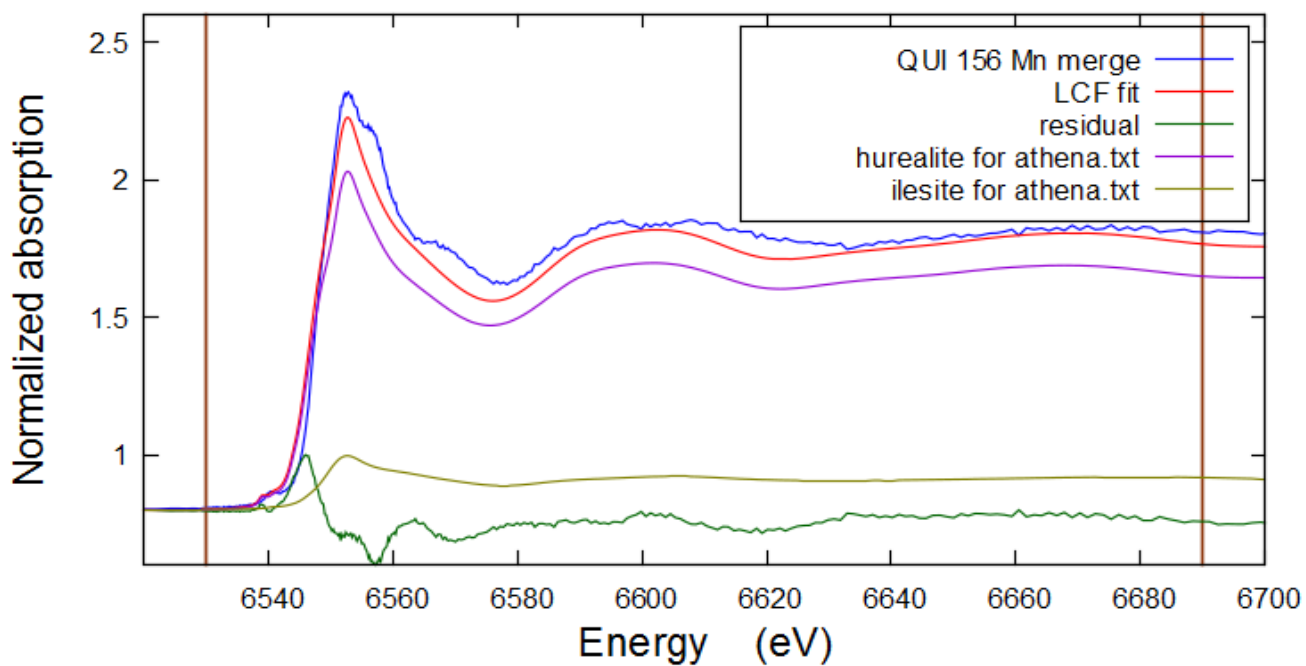Figure A11 Results of linear combination fitting in ATHENA of QUI 156 Mn K-edge XANES spectrum
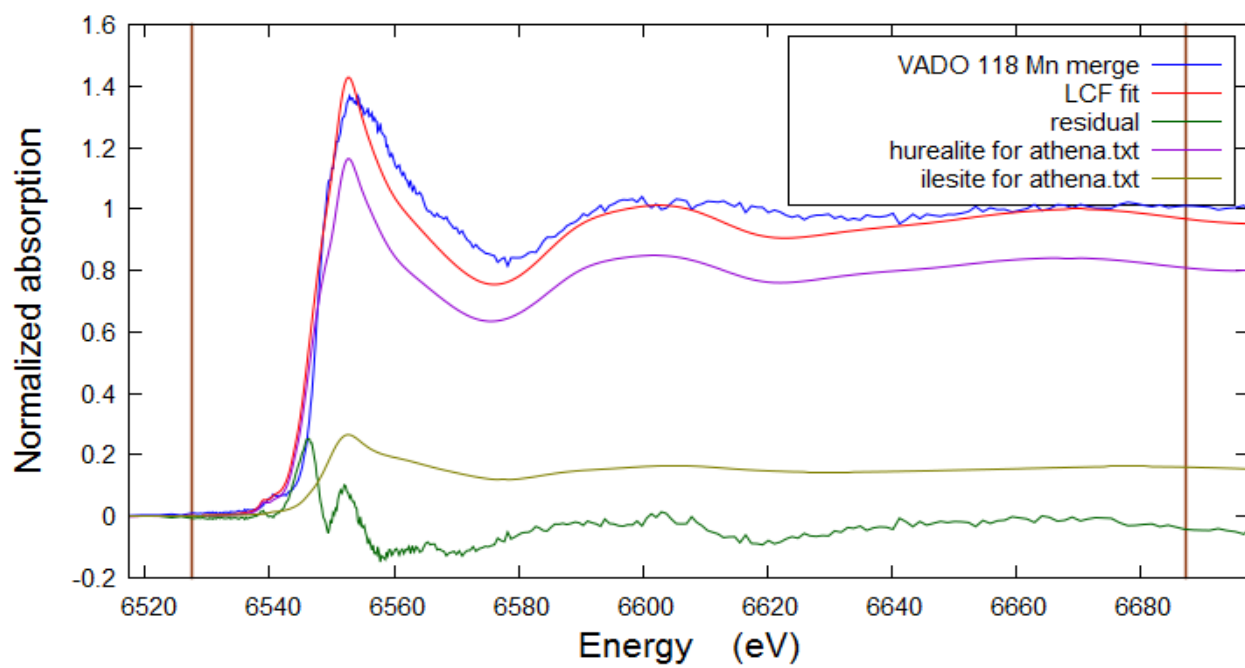
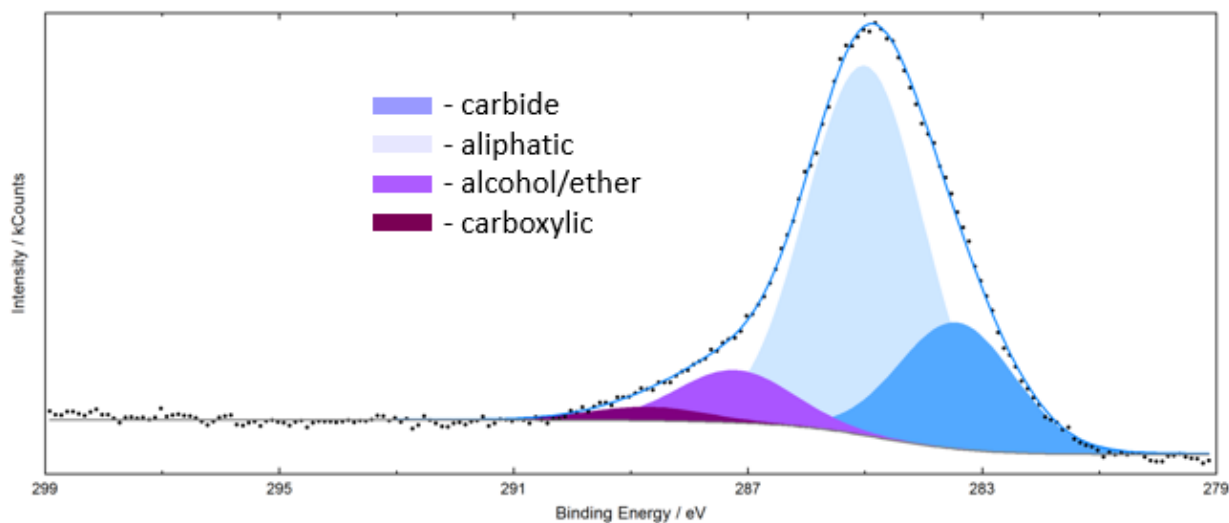Figure A13a A detailed C 1s XPS spectrum of VADO 118 after 2 min of sputtering

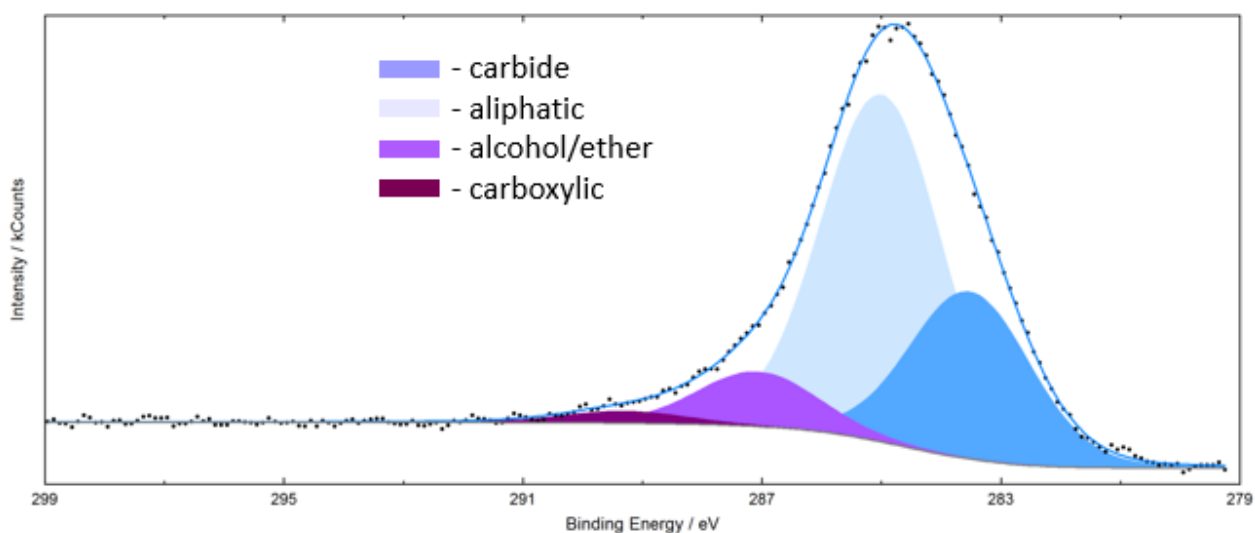Figure A13b A detailed C 1s XPS spectrum of VADO 118 after 10 min of sputtering

Figure A13c A detailed C 1s XPS spectrum of VADO 118 after 30 min of sputtering
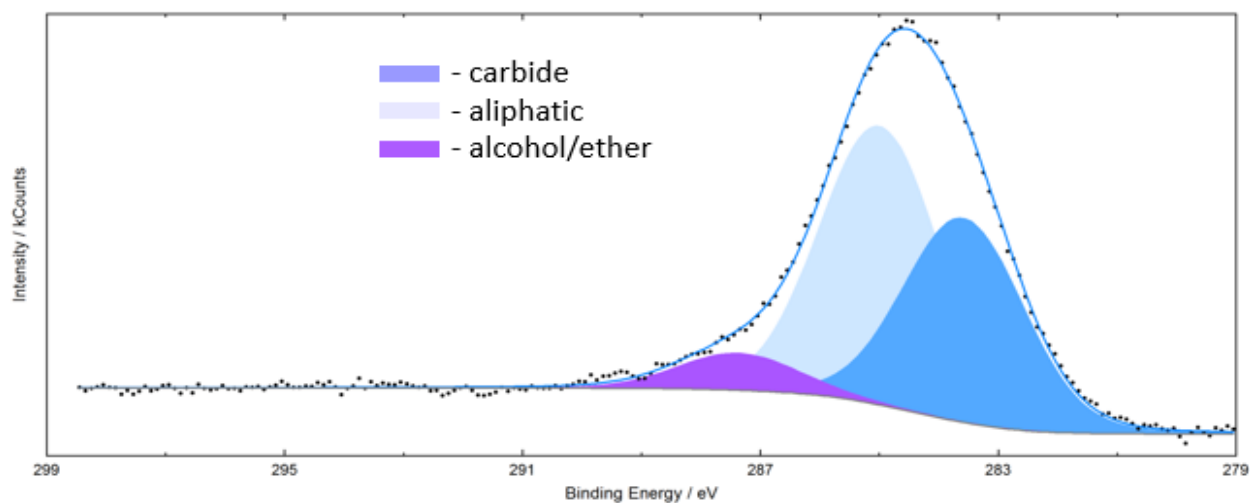
Figure A14a A detailed O 1s XPS spectrum of VADO 118 before sputtering
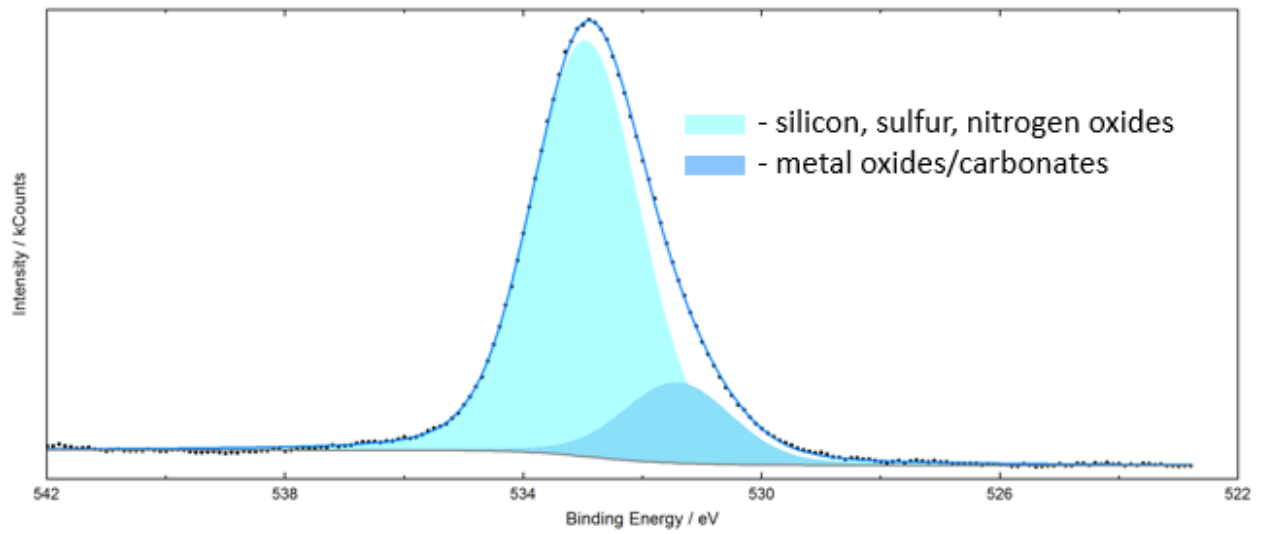

Figure A14b A detailed O 1s XPS spectrum of VADO 118 after 2 min of sputtering
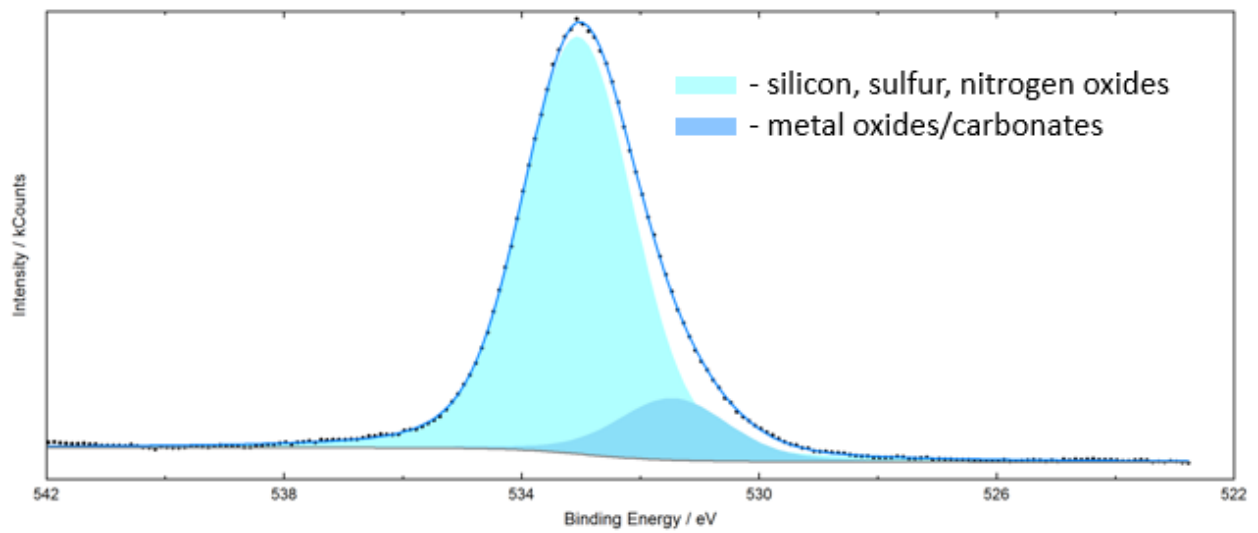
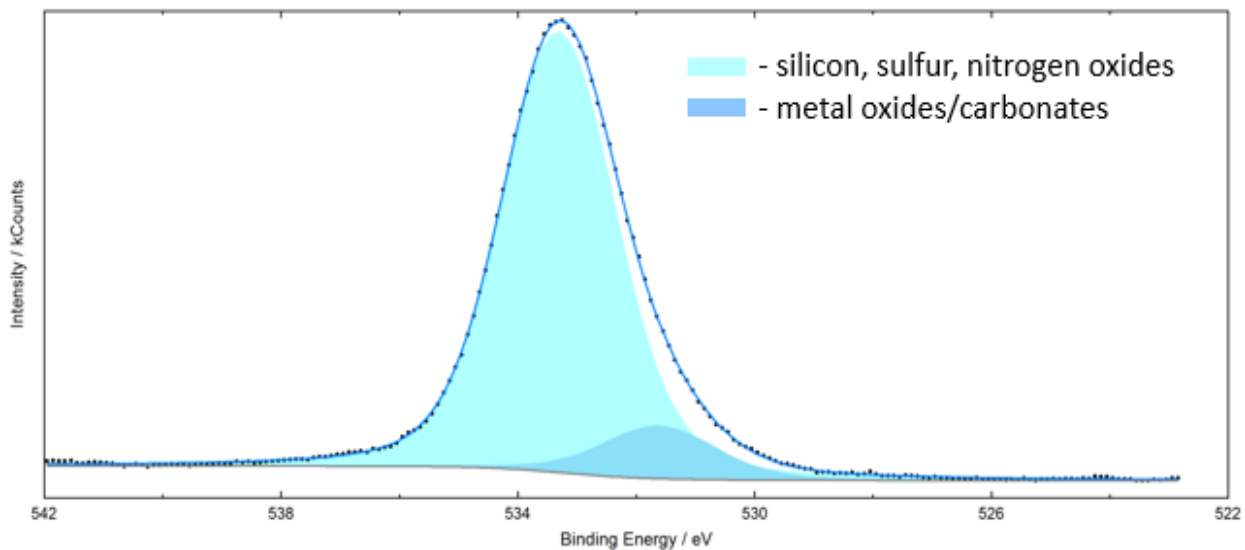Figure A14c A detailed O 1s XPS spectrum of VADO 118 after 10 min of sputtering

Figure A14c A detailed O 1s XPS spectrum of VADO 118 after 30 min of sputtering
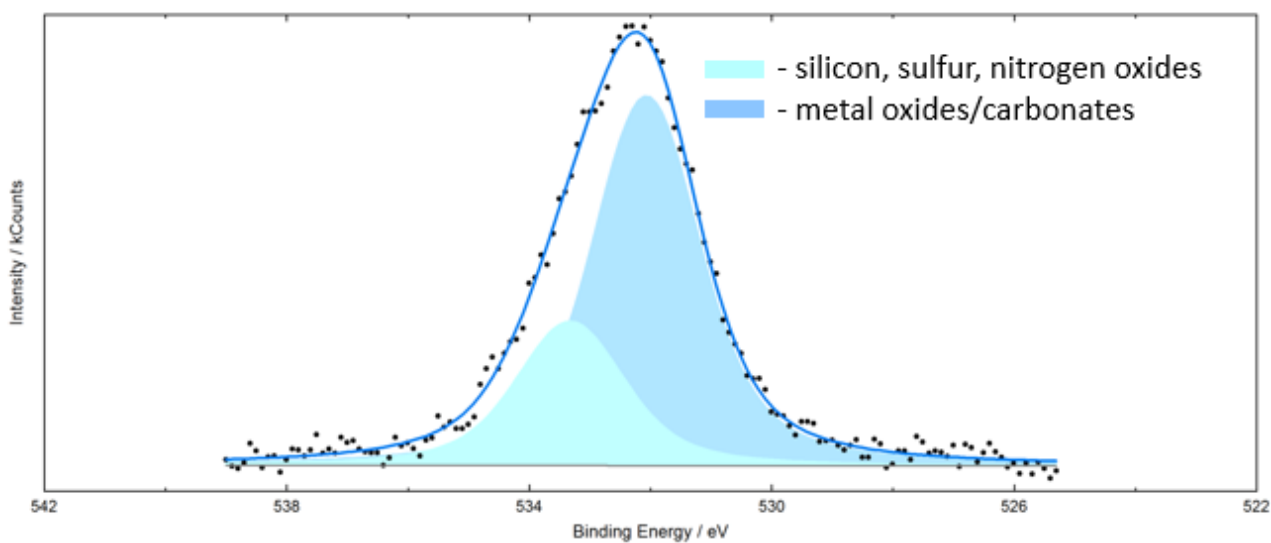
Figure A15a N1s XPS spectrum of VADO 118 before sputtering
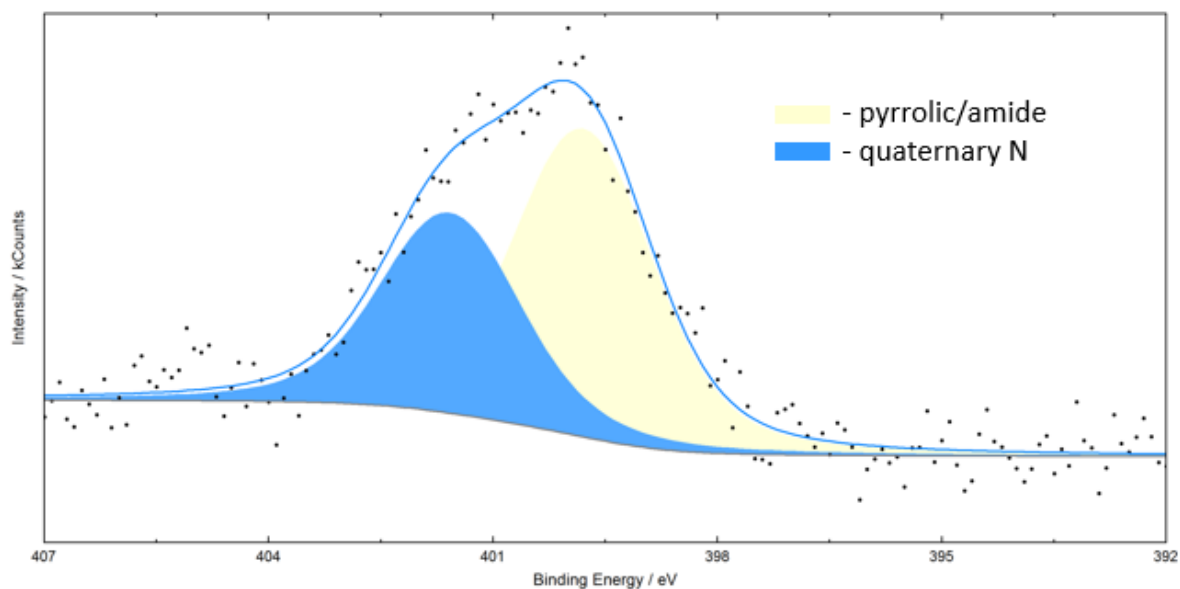
Figure A15b A detailed4 N1s XPS spectrum of VADO 118 after 2 min of sputtering
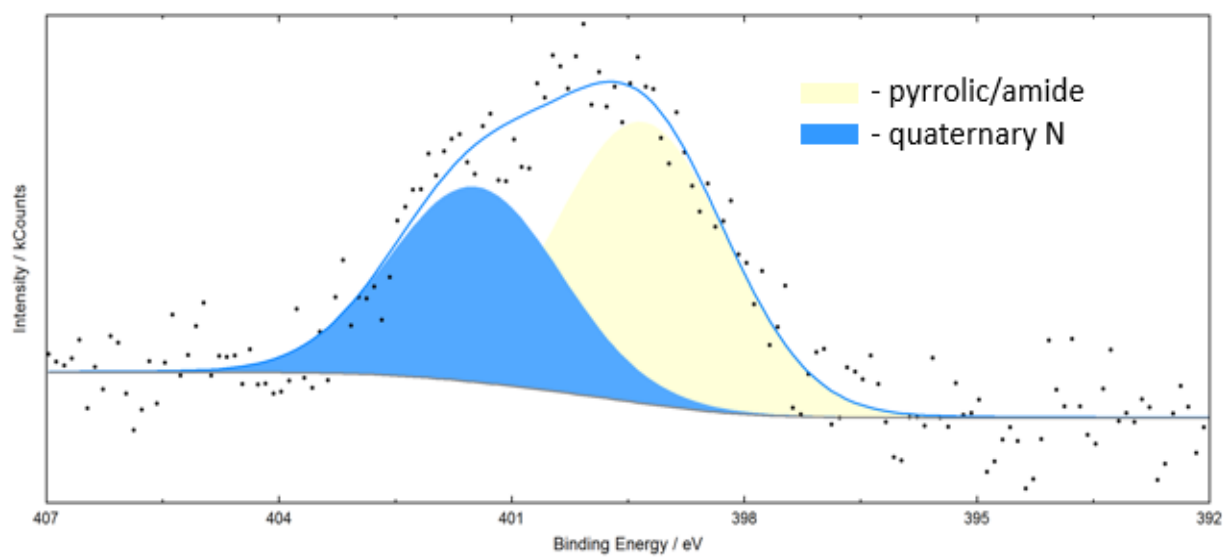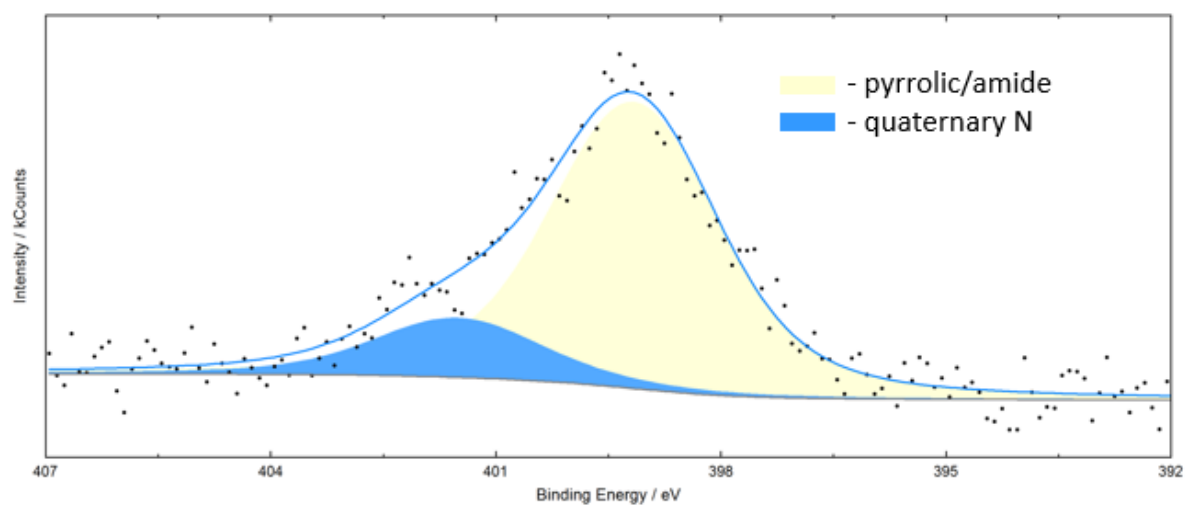
Figure A16 The pre-edge fit of Fe(NO3)3*9H2O
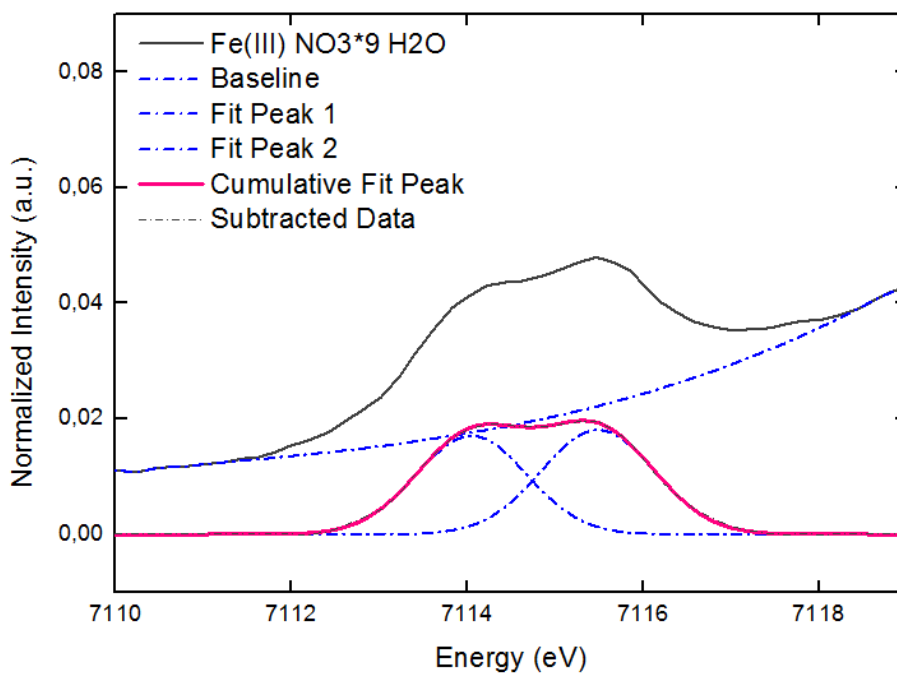
Figure A17 The pre-edge fit of FeSO4*7H2O
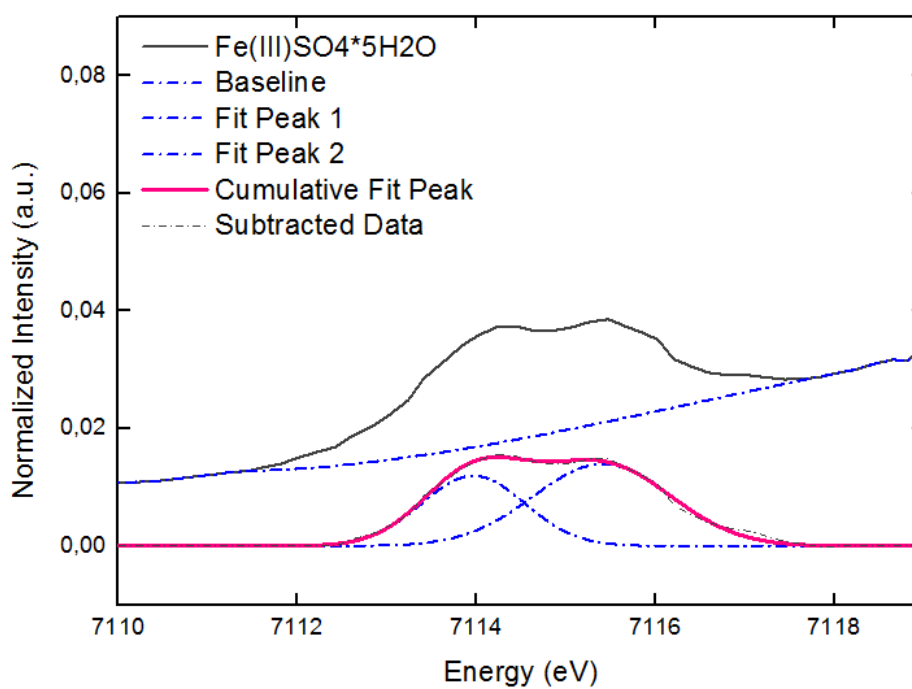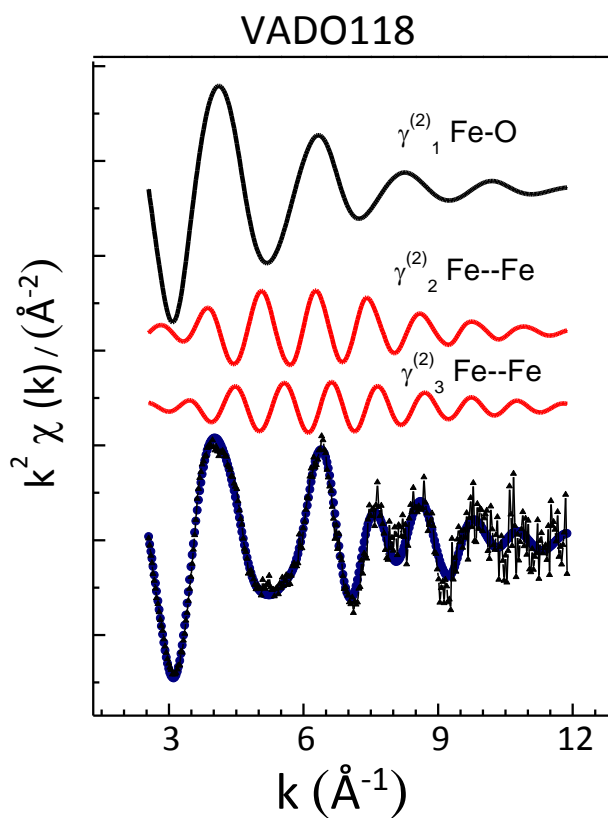
Figure A18 Best fit of VADO118 sample at Fe K-edge, in terms of individual EXAFS contributions to the total theoretical signal. The comparison of the total theoretical signal (•) with the experimental one (-▲-) is also shown at the bottom.

Figure A19 Best fit of VADO028 and QUI156 samples at Fe K-edge, in terms of individual EXAFS contributions to the total theoretical signal. The comparison of the total theoretical signal (•) with the experimental one (-▲-) is also shown at the bottom.

Error parameter determination

BIBLIOGRAPHY

1.   *Handbook of X-ray detectors*. 2012, Hamamatsu Photonics: Japan.
2.   Michael, F., *XANES spectroscopy of sulfur in Earth materials* The Canadian Mineralogist, 2005. **43**: p. 1811-1838.
3.   Giorgetti, M., *A Review on the Structural Studies of Batteries and Host Materials by X-Ray Absorption Spectroscopy.* ISRN Materials Science, 2013. **2013**: p. 22.
4.   Wilke M., F.F., Petit P.E., Brown G., Martin F., *Oxidation state and coordination of Fe in minerals: An Fe K-XANES spectroscopic study*, in *American Mineralogist*. 2001. p. 714.
5.   Joly, Y., *X-Ray Absorption Near Edge Structure Calculation Beyond the Muffin-Tin Approximation.* J. Phys. IV France, 1997. **7**(C2): p. C2-111-C2-115.
6.   Huggins, F.E., G.P. Huffman, and J.D. Robertson, *Speciation of elements in NIST particulate matter SRMs 1648 and 1650.* Journal of Hazardous Materials, 2000. **74**(1): p. 1-23.
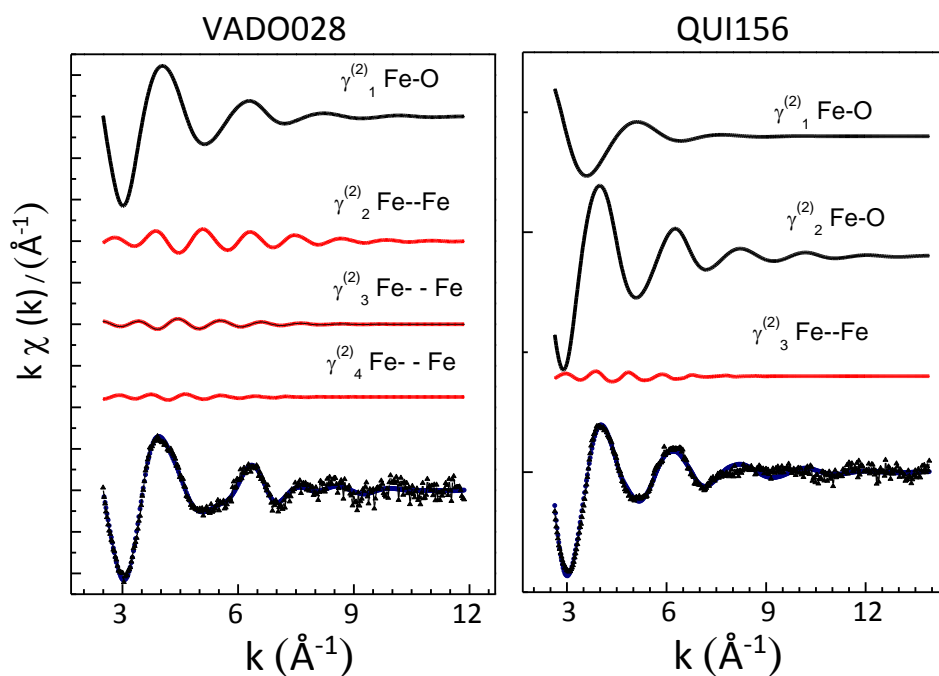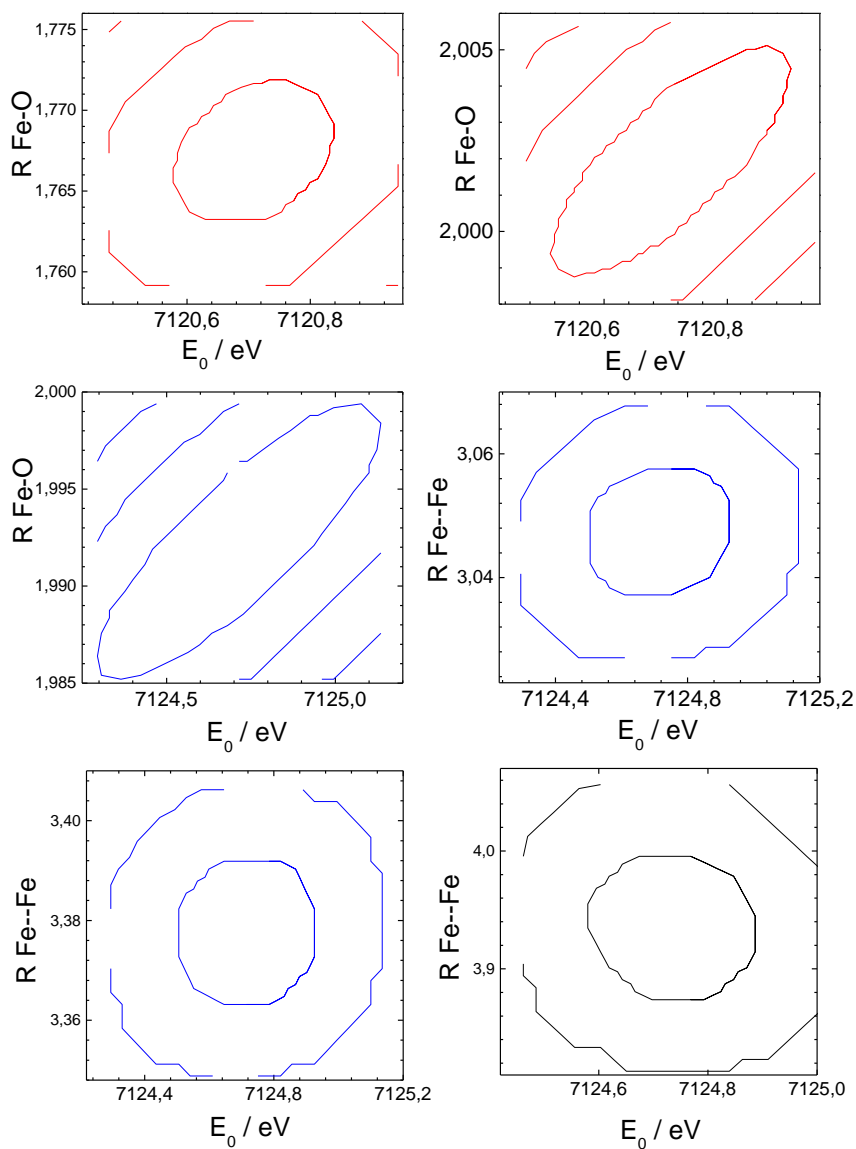7.   Westre T., K.P., DeWitt J., Hedman B., Hodgson K., Solomon E., *A Multiplet Analysis of Fe K-Edge 1s → 3d Pre-Edge Features of Iron Complexes.* Journal of the American Chemical Society, 1997. **119**(27): p. 6297-6314.
8.   Valavanidis A., F.K., Vlachogianni T., *Airborne Particulate Matter and Human Health: Toxicological Assessment and Importance of Size and Composition of Particles for Oxidative Damage and Carcinogenic Mechanisms.* Journal of Environmental Science and Health, Part C, 2008. **26**(4): p. 339-362.
9.   Holland W, B.A., Cameron I, Florey C, Leeder S, Schilling R, Swan A, Waller R, *Health effects of particulate pollution: reappraising the evidence.* Am J Epidemiol., 1979. **5**(110): p. 527-659.
10.   Kelly, F.J. and J.C. Fussell, *Size, source and chemical composition as determinants of toxicity attributable to ambient particulate matter.* Atmospheric Environment, 2012. **60**: p. 504-526.
11.   Wiseman C., Z.F., *Airborne particulate matter, platinum group elements and human health: A review of recent evidence.* Science of The Total Environment, 2009. **407**(8): p. 2493-2500.
12.   Autrup, H., *Ambient Air Pollution and Adverse Health Effects.* Procedia - Social and Behavioral Sciences, 2010. **2**(5): p. 7333-7338.
13.   Janssen, N., Brunekreef B., van Vliet P., Aarts F., Meliefste K., Harssema H., Fischer P., *The relationship between air pollution from heavy traffic and allergic sensitization, bronchial hyperresponsiveness, and respiratory symptoms in Dutch schoolchildren.* Environmental Health Perspectives, 2003. **111**(12): p. 1512-1518.
14.   G., B., *Introduction to XAFS : A Practical Guide to X-ray Absorption Fine Structure Spectroscopy*. Vol. 1. 2010, Cambridge, United Kingdom: CAMBRIDGE UNIVERSITY PRESS. 270.
15.   Joly, Y., et al., *Self-consistency, spin-orbit and other advances in the FDMNES code to simulate XANES and RXD experiments.* Journal of Physics: Conference Series, 2009. **190**: p. 012007.
16.   Nelson, R.C. and J.T. Miller, *An introduction to X-ray absorption spectroscopy and its in situ application to organometallic compounds and homogeneous catalysts.* Catalysis Science & Technology, 2012. **2**(3): p. 461-470.
17.   Briggs, D., *Handbook of X-ray Photoelectron Spectroscopy C. D. Wanger, W. M. Riggs, L. E. Davis, J. F. Moulder and G. E.Muilenberg Perkin-Elmer Corp., Physical Electronics Division, Eden Prairie, Minnesota, USA, 1979. 190 pp. $195.* Surface and Interface Analysis, 1981. **3**(4): p. v-v.
18.   V., C. *X-ray photoelectron spectroscopy*. 2010 June 30, 2017; Available from: https://en.wikipedia.org/wiki/X-ray_photoelectron_spectroscopy#/media/File:XPS_PHYSICS.png.
19.   Aquilanti G., G.M., Dominko R., Stievano L., Arčon I., Novello N., Olivi L., *Operando characterization of batteries using x-ray absorption spectroscopy: advances at the beamline XAFS at synchrotron Elettra.* Journal of Physics D: Applied Physics, 2017. **50**(7): p. 074001.
20.   Ravel B., N.M., *ATHENA, ARTEMIS, HEPHAESTUS: data analysis for X-ray absorption spectroscopy using IFEFFIT.* Journal of Synchrotron Radiation, 2005. **12**(4): p. 537-541.

21.   Hesse, R., P. Streubel, and R. Szargan, *Product or sum: comparative tests of Voigt, and product or sum of Gaussian and Lorentzian functions in the fitting of synthetic Voigt-based X-ray photoelectron spectra.* Surface and Interface Analysis, 2007. **39**(5): p. 381-391.

22.   Hesse, R., Weiß, M., Szargan, R., Streubel, P., Denecke, R., *Improved peak-fit procedure for XPS measurements of inhomogeneous samples—Development of the advanced Tougaard background method.* Journal of Electron Spectroscopy and Related Phenomena, 2015. **205**: p. 29-51.

23.   Ruben H., T.D., Rosenstein R., Olovsson I., *Crystal Structure and Entropy of Sodium Sulfate Decahydrate.* Journal of the American Chemical Society, 1961. **83**(4): p. 820-824.

24.   V., C.A. *Crystallographic and Crystallochemical Database for Minerals and their Structural Analogues*. WWW-MINCRYST 1997 June 13, 2017 [cited 2017 June 27, 2017]; Available from: http://database.iem.ac.ru/mincryst/index.php.

25.   Zachariasen W. H. , B.H.E., *The Crystal Lattice of Anhydrous Sodium Sulphite.* Physical Review, 1931. **37**(10): p. 1295-1305.

26.   Emilie, C., *ID21 SULFUR XANES SPECTRA DATABASE HOME*, E.S.R. Facility, Editor.

27.   Perraud, V., et al., *Nonequilibrium atmospheric secondary organic aerosol formation and growth.* Proceedings of the National Academy of Sciences of the United States of America, 2012. **109**(8): p. 2836-2841.

28.   Mori A., P.E., Giuli G., Eeckhout S. G., Kavčič M., Žitnik, M., Bučar K., Pettersson L. G. M., Glatzel P., *Electronic Structure of Sulfur Studied by X-ray Absorption and Emission Spectroscopy.* Analytical Chemistry, 2009. **81**(15): p. 6516-6525.

29.   Sekiyama H., N.K., Haruo K., Toshiaki O., *Sulfur K-Edge Absorption Spectra of Na2SO4, Na2SO3, Na2S2O3, and Na2S2Ox (x=5–8).* Bulletin of the Chemical Society of Japan, 1986. **59**(2): p. 575-579.

30.   Dräger, G., et al., *On the Multipole Character of the X-Ray Transitions in the Pre-Edge Structure of Fe K Absorption Spectra. An Experimental Study.* physica status solidi (b), 1988. **146**(1): p. 287-294.

31.   Petit, P.-E., et al., *Determination of the iron oxidation state in Earth materials using XANES pre-edge information.* Journal of Synchrotron Radiation, 2001. **8**(2): p. 952-954.

32.   Allen, G.C., et al., *X-Ray photoelectron spectroscopy of iron-oxygen systems.* Journal of the Chemical Society, Dalton Transactions, 1974(14): p. 1525-1530.

33.   McIntyre, N.S. and D.G. Zetaruk, *X-ray photoelectron spectroscopic studies of iron oxides.* Analytical Chemistry, 1977. **49**(11): p. 1521-1529.

34.   Maslen, E.N., et al., *Synchrotron X-ray study of the electron density in [alpha]-Fe2O3.* Acta Crystallographica Section B, 1994. **50**(4): p. 435-441.

35.   Krause M.O. , O.J.H., *Natural widths of atomic K and L levels, Kα X-ray lines and several KLL Auger lines.* Journal of Physical and Chemical Reference Data, 1979. **8**(2): p. 329-338.

36.   Filipponi, A., Di Cicco A. , *X-ray-absorption spectroscopy and n-body distribution functions in condensed matter. II. Data analysis and applications.* Physical Review B, 1995. **52**(21): p. 15135-15149.

37.   Filipponi, A., A. Di Cicco, and C.R. Natoli, *X-ray-absorption spectroscopy and n-body distribution functions in condensed matter. I. Theory.* Physical Review B, 1995. **52**(21): p. 15122-15134.

38.   Giorgetti, M., et al., *Evidence of four-body contributions in the EXAFS spectrum of Na2Co[Fe(CN)6].* Chemical Physics Letters, 1997. **275**(1): p. 108-112.

39.   Hedin L., L.B., *Explicit local exchange-correlation potentials.* Journal of Physics C: Solid State Physics, 1971. **4**(14): p. 2064.

40.   Demri, B. and D. Muster, *XPS study of some calcium compounds.* Journal of Materials Processing Technology, 1995. **55**(3): p. 311-314.

41.   González, L.T., et al., *Determination of trace metals in TSP and PM2.5 materials collected in the Metropolitan Area of Monterrey, Mexico: A characterization study by XPS, ICP-AES and SEM-EDS.* Atmospheric Research, 2017. **196**: p. 8-22.

42.   Guascito, M.R., et al., *XPS surface chemical characterization of atmospheric particles of different sizes.* Atmospheric Environment, 2015. **116**: p. 146-154.

43.   Farges F., B.G., E., Rehr J., J., *Ti K-Edge XANES Studies of Oxides: Theory vs. Experiment.* J. Phys. IV France, 1997. **7**(C2): p. C2-191-C2-193.

44.   Chen, L.X., et al., *XAFS Studies of Surface Structures of TiO2 Nanoparticles and Photocatalytic Reduction of Metal Ions.* The Journal of Physical Chemistry B, 1997. **101**(50): p. 10688-10697.

45.   Tong T., H.A., Alsina M., Wu J., Shang K., Kelly J., Gray K., Gaillard J.F., *Spectroscopic Characterization of TiO2 Polymorphs in Wastewater Treatment and Sediment Samples.* Environmental Science & Technology Letters, 2015. **2**(1): p. 12-18.

46.   Howard, C.J., T.M. Sabine, and F. Dickson, *Structural and thermal parameters for rutile and anatase.* Acta Crystallographica Section B, 1991. **47**(4): p. 462-468.

47.   Giorgetti, M., M. Berrettoni, and W.H. Smyrl, *Doped V2O5-Based Cathode Materials: Where Does the Doping Metal Go? An X-ray Absorption Spectroscopy Study.* Chemistry of Materials, 2007. **19**(24): p. 5991-6000.

48.   Giorgetti, M.P., Stefano; Smyrl, William H.; Mukerjee, Sanjeev; Yang, X. Q.; McBreen, James., *In situ X-ray absorption spectroscopy characterization of V2O5 xerogel cathodes upon lithium intercalation.* Journal of the Electrochemical Society, 1999. **146**(7): p. 2387-2392.

49.   Wong J., L.F., Messmer R., Maylotte D., *K-edge absorption spectra of selected vanadium compounds.* Physical Review B, 1984. **30**(10): p. 5596.

50.   Chaurand, P., et al., *New Methodological Approach for the Vanadium K-Edge X-ray Absorption Near-Edge Structure Interpretation: Application to the Speciation of Vanadium in Oxide Phases from Steel Slag.* The Journal of Physical Chemistry B, 2007. **111**(19): p. 5101-5110.

51.   Szulczewski M., H.P., Bleam W., *Comparison of XANES Analyses and Extractions To Determine Chromium Speciation in Contaminated Soils.* Environmental Science & Technology, 1997. **31**(10): p. 2954-2959.

52.   Riou, A. and A. Bonnin, *Structure de l'hydroxysulfate de chrome monohydrate.* Acta Crystallographica Section B, 1981. **37**(5): p. 1031-1035.

53.   Ressler T., W.J., Roos J.,, *Manganese speciation in exhaust particulates of automobiles using MMT-containing gasoline.* Journal of Synchrotron Radiation, 1999. **6**(3): p. 656-658.

54.   Bridinette Thiodjio, S., et al., *Fe, Ni and Zn speciation, in airborne particulate matter.* Journal of Physics: Conference Series, 2016. **712**(1): p. 012087.

55.   Cheng, W., et al., *Surface Chemical Composition of Size-Fractionated Urban Walkway Aerosols Determined by X-Ray Photoelectron Spectroscopy.* Aerosol Science and Technology, 2013. **47**(10): p. 1118-1124.

56.   Zhu Y., O.N., Beebe T., *Surface Chemical Characterization of 2.5-μm Particulates (PM2.5) from Air Pollution in Salt Lake City Using TOF-SIMS, XPS, and FTIR.* Environmental Science & Technology, 2001. **35**(15): p. 3113-3121.

57.   Hutton, B.M. and D.E. Williams, *Assessment of X-ray photoelectron spectroscopy for analysis of particulate pollutants in urban air.* Analyst, 2000. **125**(10): p. 1703-1706.

58.   Scientific, T.F. *XPSsimplified*. [cited 2017 23.06.17]; Available from: http://xpssimplified.com/elements/sodium.php#appnotes.

59.   Song, J. and P.a. Peng, *Surface Characterization of Aerosol Particles in Guangzhou, China: A Study by XPS.* Aerosol Science and Technology, 2009. **43**(12): p. 1230-1242.

60.   He, J.W., et al., *X-ray photoelectron spectroscopic characterization of ultra-thin silicon oxide films on a Mo(100) surface.* Surface Science, 1992. **279**(1): p. 119-126.

61.   Suárez-Peña B., N.L., Castrillón L., Megido L., Marañón E., Fernández-Nava Y., *Imaging Techniques and Scanning Electron Microscopy as Tools for Characterizing a Si-Based Material Used in Air Monitoring Applications.* Materials, 2016. **9**(2): p. 109.